Department of Physics and Astronomy

University of Heidelberg

Master thesis

in Physics

submitted by

Ludwig Franz Rauch

born in Dachau

2014

Detector characterization, electronic-recoil energy scale and astrophysical independent results in XENON100

This Master thesis has been carried out by Ludwig Franz Rauch

at the

Max-Planck-Institut für Kernphysik

under the supervision of

Herrn Prof. Dr. Manfred Lindner

Detektor Charakterisierung, Energieskala für elektromagnetische Wechselwirkungen und astrophysikalisch unabhängige Ergebnisse in XENON100:

Für über drei Jahre war XENON100 das Experiment mit der höchsten Sensitivität, bei der Suche nach einem schwach wechselwirkenden und schweren (WIMP) Dunkle Materie Teilchen bei einer Masse von 55 GeV und einem Wirkungsquerschnitt von $2.0 \times 10^{-45}\,\mathrm{cm}^2$. In dieser Arbeit werden verschiedene Analysen vorgestellt, die eine Suche nach Dunkler Materie mit dem XENON100 Experiment erweitern. Dabei werden zunächst für die Dunkle Materie Daten von 2013/2014, sowohl die Licht- und Ladungsausbeute quantifiziert, als auch eine verbesserte Korrekturkarte für das Ladungssignal vorgestellt, mit der die Energieauflösung des Detektors erhöht werden kann. Außerdem wird eine Methode eingeführt und erste Ergebnisse vorgestellt, mit der die Ladungsausbeute von elektromagnetischen Wechselwirkungen in flüssigen Xenon mit dem XENON100 Detektor bestimmt werden kann. Zum Schluss wird ein Verfahren bentutzt um Ausschlusskurven für WIMP - Kern wechselwirkungen zu berechnen, die unabhäning von astrophysikalischen Unsicherheiten sind.

Detector characterization, electronic recoil energy scale and astrophysical independent results in XENON100:

For over three years, the XENON100 experiment set the benchmark sensitivity for the weakly interacting massive particle (WIMP) dark matter candidate, with a cross-section of $2.0 \times 10^{-45}\,\mathrm{cm}^2$ at 55 GeV for spin independent interactions. In this thesis various analysis are introduced to extend the dark matter search with the XENON100 detector. For the science data taken in 2013/2014, studies on the light and charge yield as well as an optimized correction for the secondary scintillation signal is introduced, resulting in an increased energy resolution of the detector. Secondly, a method to determine the charge yield for electromagnetic interactions in liquid xenon with the XENON100 detector is developed and results are presented. Finally, a method is used to derive bounds on the WIMP - nucleus interactions, free of astrophysical uncertainties.

Contents

List of Figures

List of Tables

Chapter 1

Introduction

The XENON100 experiment is dedicated to the quest of directly detecting dark matter. Thus, in the following introduction, a short summary of the theoretical motivations for dark matter searches is given and the most popular dark matter candidates are discussed. Finally, various models for dark matter halos and measurements of the relevant astrophysical parameters are explained.

1.1 The observation of dark matter

Historically, the first indications of missing gravitational potentials in the Universe was observed in 1933 by Zwicky [1] who observed galaxy clusters, large gravitationally bounded objects. Zwicky measured the radial velocities of galaxies in the Coma-cluster and found that the velocities exceed expectations by an order of magnitude.

In 2014 the nature of dark matter remains unknown, however, the estimations of the amount of dark matter, as well as various different observations, strengthen the conclusion of an *invisible mass* in our Universe. One of the strongest indications can be derived from the power spectrum of the measured temperature anisotropies calculated from the cosmic microwave background [2, 3]. From a fit of the oscillation pattern seen in the power spectrum, it is possible to conclude that a gravitational potential exists which is not affected by radiation pressure and it accounts for approximately 26.8 % of the total energy in our Universe [2]. In addition, a calculation of the processes during the Big Bang nucleosynthesis [4] can derive the observed abundances of light elements, which can not account the total necessary gravitational potential. At later cosmological times, a component of dark matter with low random velocities (cold dark matter or CDM) is necessary to simulate correctly the formation of structures in the Universe [5]. The presence of dark matter can be reconstructed by its gravitational potential mapped from its weak lensing signal [6], in e.g. galaxy clusters. With this method, the weak self interaction of dark matter can also be tested when cluster of galaxies collide [7, 8] as the center of mass of the total gravitational potential does not coincide with the visible mass center. At smaller scales, adding this invisible mass as a dark matter halo to galaxies can explain the large radial velocities of objects which are far away from the center [9].

1.2 Dark matter candidates

The missing mass problem in Cosmology and Astrophysics might be solved by postulating a dark matter particle. Naturally, the question arises what properties and origin this particle might have. Cosmology shows that dark matter interacts gravitationally as its mass can be reconstructed from weak gravitational lensing ([7, 8]). Baryonic oscillations before photons decouple show that dark matter is not affected by radiation pressure and interactions via the electromagnetic force can be ruled out [3, 2]. Furthermore, a coupling via the strong force can be ruled out since the cross-section to couple to ordinary matter would be large and therefore would have been observed already. Finally, Cosmology constrains strongly the stability of dark matter particles, since the abundance has not changed during the evolution of the Universe. These properties rule out most of the known particles of the standard model. Neutrinos are in general good dark matter candidates, but due to their highly relativistic velocities, fermionic nature and small masses, they can only contribute partly to the missing gravitational potential. Since they are fermions and follow the Pauli exclusion principle, their finite phase space density can not account for the total mass observed in dark matter halos [10]. Hence, it seems that dark matter can not be explained within the framework of the standard model of particle physics.

In addition, constraints of the dark matter velocities can be derived from simulations of the formation of structure [5]. The authors show that only small random velocities of dark matter particles give rise to enough structure, in order to create stars and galaxies. Therefore, dark matter needs to be cold or warm but can not show relativistic velocities (hot). In the scope of this work only weakly interacting massive particles as well as axion and axion-like particles are introduced as possible dark matter candidates, as they are relevant for the following chapters. However, it is to mention that generally a large number of different dark matter particle models exist and more information can be found in [11].

Weakly interacting massive particles Weakly interacting massive particles (WIMPs) are one of the best motivated candidates. It stems from the fact that they can be thermally produced in thermal equilibrium in the early Universe and naturally have the right abundance to be cold dark matter. A coupling via the weak force to standard model particles would have the right coupling strength to be a WIMP and would allow a similar production mechanism as included in the standard model (eg. $\chi\bar{\chi} \leftrightarrow f\bar{f}, W^+W^-, HH...$) [12]. The weak interactions enable a test of the model through a direct detection of the scattering processes with nuclei in ground based detectors. Figure 1.1 shows the current constraints on the WIMP model for spin independent interactions, tested by a number of different experiments. So far the DAMA collaboration measured a signal with a statistical significance of 8.9 sigma [13] and other experiments e.g. CoGeNT and CRESST-II measured a small excess of events above their expectations, which is indicated by the contours in figure 1.1. However, the stated best fit values of these signals can not be explained by a single WIMP mass and cross-section. Furthermore, various other experiments exclude these signal claims (e.g. [14, 15, 16]) which can be seen e.g. by the blue and purple line, indicating the absence of cross-sections above the lines. So far no clear evidence for the WIMP hypothesis is present.

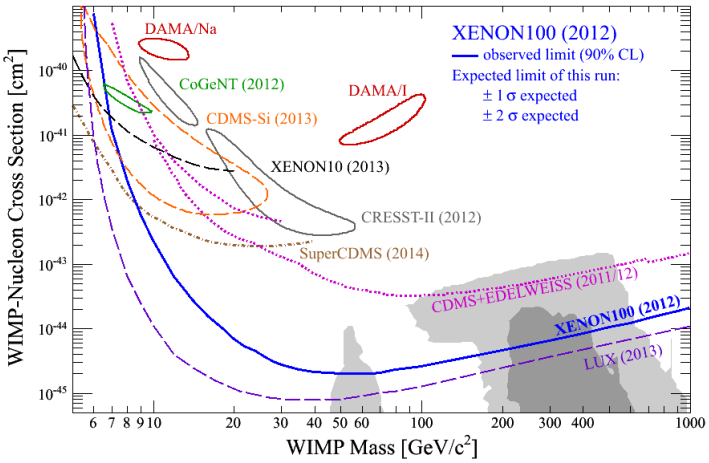

Figure 1.1: Exclusion limits and signal contours for isospin conserving and spin independent interactions. It can be seen that the LUX experiment [14] as well as the XENON100 results exclude most of the shown parameter space [15]. Even at low WIMP masses the super CDMS experiment [16] excludes a parameter space where various other experiments indicate the presence of a WIMP. The grey region indicates prefered regions from CMSSM models. Further information and references can be found in [15]. Figure adapted from [15].

Axions and axion like particles Axions or axion like particles (ALPs) are particles which, in case of a discovery, could not only account for the dark matter in the Universe but might explain the small neutron electric dipole moment [17], known as the 'strong CP problem' of the standard model of particle physics. The axion mass would be a quasi-Nambu-Goldstone boson, generated by the spontaneous breaking of the postulated U(1) Peccei-Quinn (PQ) symmetry [18]. In models where the axion or ALP account for the CDM in the Universe and couple to electron with a strength g_{Ae}, some experimental constrains exist and are shown in figure 1.2. Note that Axion and ALP couple to the electrons and not to the nucleus as it is the case of the WIMP model.

1.3 Detection principles of dark matter particles

To illustrate the existing methods to observe dark matter particles, figure 1.3 shows a sketch of an effective Feynman diagram. It describes a possible coupling of a dark matter particle (χ) to fermions (f) of the standard model. If read from bottom to top, it indicates the possibility to search for dark matter with colliders which could produce these new particles (e.g. [20]). This, however, is challenging since the dark matter particles can not be observed directly but only through a missing energy signal. Another promising possibility is an indirection detection, if the dark matter particles annihilate to particles of the standard model and shown in figure 1.3, if read from top to bottom. Signal indications by an observation of photons is reported with Fermi data [21] with an energy of 130 GeV and at an energy of 3.5 keV by [22, 23]. However, so far no clear evidence is present. In addition, the diagram can be read from left to right, which illustrates a scattering process and would enable a direct detection. This work focuses on this method, since the

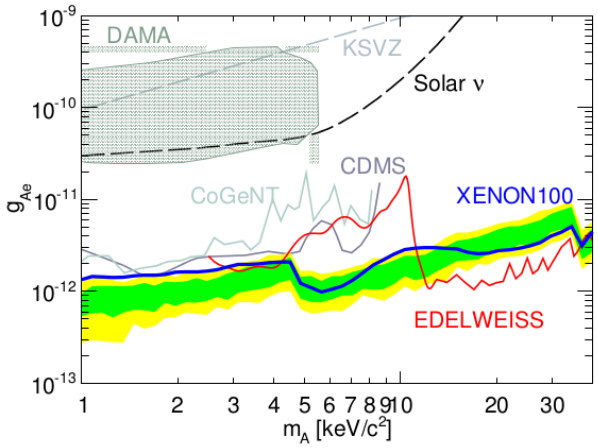

Figure 1.2: Experimental limits on ALP coupling (g_{Ae}) to electrons as a function of the particle mass m_A, under the assumption that ALPs account for all the dark matter in our galaxy. The limit and expected sensitivity for the XENON100 experiment on these interaction is shown by the blue line and green/yellow bands (one and two sigma), respectively. The contour area corresponds to a possible interpretation of the DAMA annual modulation signal due to ALP interactions. The other curves are constraints derived by CoGeNT (brown dashed line), CDMS (grey continuous line), and EDELWEISS-II (red line). Indirect astrophysical bounds from solar neutrinos is represented as a dashed line. The dashed grey line illustrates a theoretical prediction (KSVZ). Figure, more information and references in [19].

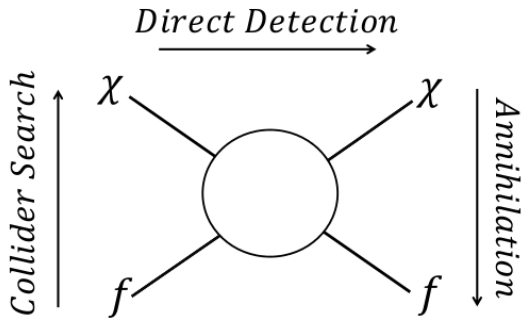

Figure 1.3: This sketch indicates different effective Feynman diagrams to illustrate possible observable through WIMP (χ) interactions with fermions (f).

XENON100 detector is built to measure these direct interactions.

1.4 Expected recoil rates in direct detection experiments

If the missing gravitational potential in our Universe can be explained by WIMPs and they are homogeneously distributed in a dark matter halo around the Milky Way, then this hypothesis can be tested by Earth based detectors. Generally, a hypothetical dark matter candidate can be detected if the signal shows a time, direction or energy dependence. The time dependence is introduced due to the revolution of the Earth around the Sun with a period of one year [24]. The dependence of the direction is explained by the motion of the target around the Galactic rest frame and the measured recoil spectrum is expected to peak in direction of the motion of the Earth [25]. And, finally, the most common signal to search for dark matter particles is motivated by its energy dependence (e.g. XENON100) which is discussed in detail below.

If m_χ is the WIMP mass, E_{nr} the nuclear recoil energy and m_A the mass of the target nucleus, the differential scattering rate $\frac{dR_A}{dE_{nr}}$ is given by [26, 27],

$$\frac{dR_A}{dE_{nr}} = \frac{\rho_\chi}{m_\chi m_A} \cdot \int_{v \geq v_{min}} d^3v \cdot \frac{d\sigma}{dE_{nr}}(v, E_{nr}) \cdot f(\mathbf{v}, t)\, v, \tag{1.1}$$

where ρ_χ is the local dark matter density and $f(\mathbf{v}, t)$ describes the dark matter velocity distribution of the halo in terms of the WIMP velocity (v) of the nucleus frame of reference and the time (t) (see section 1.5). The differential WIMP-nucleus cross section for elastic scattering is expressed by $\frac{d\sigma}{dE_{nr}}$. It encodes the involved model of particle physics such as assumptions on the microscopic WIMP-quark interactions. It is useful to decompose spin independent (SI) and spin dependent (SD) contributions of the total cross-section. Since the cross-section is energy dependent, it can be further decomposed by introducing the cross section at zero momentum transfer σ_0 and encoding the momentum transfer by the form factor $F(E_{nr})$

$$\frac{d\sigma}{dE_{nr}} = \frac{m_A}{2\mu_A^2 v^2} \left(\sigma_0^{SI} F_{SI}^2(E_{nr}) + \sigma_0^{SD} F_{SD}^2(E_{nr})\right), \tag{1.2}$$

with μ_A^2 being the reduced mass of the WIMP-nucleus system. In the scope of this work, only spin independent contributions of the cross-section will be considered.

A first assumption on the microscopic processes between WIMPs and quarks of the target nucleus which contribute to the spin independent cross-section could arise from scalar - scalar and vector - vector couplings in the Lagrangian

$$\mathcal{L} \supset \alpha_q^S \bar{\chi}\chi\bar{q}q + \alpha_q^V \bar{\chi}\gamma_\mu\chi\bar{q}\gamma^\mu q, \tag{1.3}$$

where α_q^S denotes the scalar and α_q^V the vector coupling strength, q and χ represent the quark and WIMP spinors, respectively. The Dirac matrices are indicated by γ_μ. Following [27], it can be shown that the dominant term arises from the scalar coupling due to its A^2 dependency, and the vector - vector couplings can be safely neglected. An analysis of the scalar coupling term in the Lagrangian leads to the spin independent contribution to the scattering cross-section

$$\sigma_0^{SI} = \sigma_p \frac{\mu_A^2}{\mu_p^2} \left[Zf^p + (A - Zf^n)\right]^2. \tag{1.4}$$

With σ_p being the WIMP-proton cross-section, μ_p the WIMP-proton reduced mass, A the mass number, Z the atomic number, and f^p and f^n the coupling strengths to protons and neutrons, respectively. Inserting equation 1.4 in 1.2 and considering only spin independent contributions, the differential cross-section reads,

$$\left(\frac{d\sigma}{dE_{nr}}\right)_{SI} = \sigma_p \frac{m_A}{2v^2 \cdot \mu_p^2} \left[Zf^p + (A - Zf^n)\right]^2 F(E_{nr})^2. \tag{1.5}$$

Equation 1.5 can be simplified, by assuming that the interaction between the WIMP and nucleus is independent of the isospin. This leads to an equal coupling of WIMPs to neutrons and protons ($f^p = f^n$), resulting in

$$\left(\frac{d\sigma}{dE_{nr}}\right)_{SI} = \sigma_p \frac{m_A}{2v^2 \cdot \mu_p^2} \cdot A^2 \cdot F(E_{nr})^2. \tag{1.6}$$

1.5 The dark matter halo

This section tries to give a brief summary of different halo models and the uncertainties of the involved astrophysical parameters since these assumption enter the rate equation 1.1. It is beyond the scope of this work to explain in detail the various methods of determining these parameters and therefore this section is a short summary of astrophysical uncertainties and introduces only a selection of velocity distributions. For more details see [28, 29, 30, 27] and references therein.

The distance to the Galactic center The distance R_0 from the Galactic center to the Sun is not an explicit parameter of the rate equation 1.1 but enters directly in the calculation of the local dark matter density ρ_0 and the circular velocity v_c (see below). Generally, a distance of $R_0 = (8.0 \pm 0.5)\,\mathrm{kpc}$ [31] is assumed but this calculation dates back to 1993 and more recent determinations indicate that this value is not compatible with the Galactic rotation velocity of 220 km/s. For instance in [32], two values are determined with independent approaches and yield in $(7.4 \pm 0.2|_{stat} \pm 0.2|_{sys})\,\mathrm{kpc}$ and $(7.5 \pm 0.3)\,\mathrm{kpc}$.

Density The parameter ρ_0, introduced in equation 1.1, describes the dark matter density at the position of the Sun with respect to the Milky Way center, $\rho_0 \equiv \rho(r = R_0)$. Generally, two different approaches exist to determine the local dark matter density. On the one hand, the density can be estimated from velocities of stars in the Milky Way at R_0 [33]. This requires the knowledge of the exact shape of the dark matter halo including assumptions on spherical symmetry, the global and local shape. This method bears large systematic errors due to its assumptions on the halo model. For spherical models, the authors in [34] derive a value of $\rho_0 = (0.2 - 0.4)\,\mathrm{GeV\,cm^{-3}}$ and even lower value $\rho_0 = 0.11^{+0.34}_{-0.27}\,\mathrm{GeV\,cm^{-3}}$ is stated in [35].

On the other hand, it is possible to determine the local dark matter density by the kinematics of stars in the Solar neighborhood [36]. This approach relies on fewer assumptions but the resulting values show usually larger errors. In [35], a maximal value of $\rho_0 = 1.25^{+0.3}_{-0.34}\,\mathrm{GeV\,cm^{-3}}$ is determined if a non-isothermal halo profile is assumed. More information can be found in [37].

Circular speed The Earth's velocity relative to the Galactic center is described by the motion of the local standard of rest (LSR), the Sun's peculiar motion with respect to the LSR and the Earth's orbit around the Sun [27]. If the Milky Way has radial symmetry, then the motion of the LSR can written in terms of the circular velocity $(0, \mathrm{v_c}, 0)$. The circular speed is in direction of the galactic rotation and usually estimated to $\mathrm{v_c} = 220\,\mathrm{km\,s^{-1}}$. This standard value dates back to 1986 and was derived by simple averaging over the various estimated values at that time [38]. Recent calculations, however, can differ significantly. The velocity can be measured by observing the motions of Galactic masers, but depends strongly on the underlying model of the Milky Way. Stating the minimal and maximal values in [35], the velocities range from $\mathrm{v_c} = (200 \pm 20)\,\mathrm{km\,s^{-1}}$ to $\mathrm{v_c} = (279 \pm 33)\,\mathrm{km\,s^{-1}}$ [39]. The deviations of these parameters arise due to differing models for the rotation curve of the Milky Way which indicates large systematic errors.

Escape velocity Dark matter particles are only bound to the Milky Way if their velocities do not exceed the escape velocity ($\mathrm{v_{esc}}$) of the gravitational potential. This velocity can be determined by the speed of high velocity stars. An analysis reveals that the escape velocity ranges from $498\,\mathrm{km\,s^{-1}} < \mathrm{v_{esc}} < 608\,\mathrm{km\,s^{-1}}$ at 90% confidence [40]. Usually, the median $\mathrm{v_{esc}} = 544\,\mathrm{km\,s^{-1}}$ of this velocity interval is used.

Velocity distribution of halo models In general, the velocity distribution of dark matter particles within a halo is derived from the matter density distribution, which can be estimated either from measurements or derived by N-body simulations. It depends not only on the velocity but also shows a time dependency due to the revolution of the Earth around the Sun. The former method assumes a spherical symmetric and isotropic distribution, where no preferred direction of the velocity vector $\mathbf{v}$ is present at the position of the Earth. This, so called, standard halo model (SHM) is derived from the collisionless Boltzmann equation and is expressed by the Maxwell-Boltzmann velocity distribution which is truncated at the escape velocity $\mathrm{v_{esc}}$. Thus its 0 for all values $|\mathbf{v}| \geq \mathrm{v_{esc}}$ and, for $|\mathbf{v}| < \mathrm{v_{esc}}$, it can be written as

$$f(\mathbf{v}) = \mathrm{N} \cdot \left(\mathrm{e}^{-\frac{\mathrm{v}^2}{\mathrm{v}_0^2}} - \mathrm{e}^{-\frac{\mathrm{v}_{\mathrm{esc}}^2}{\mathrm{v}_0^2}} \right), \tag{1.7}$$

where N is the normalization constant and the parameters $\mathrm{v_{esc}}$ and $\mathrm{v_0}$ need to be determined from direct measurements. However, this sharp truncation of the velocity distribution is unphysical. This give rise to other models, e.g. King models [41], which are based on the SHM distribution but try to avoid a sharp cut off at large velocities. Note that this model is used to derive results for direct detection experiments as shown in figure 1.1.

A further extension, the so-called "non-standard halo models", allow different velocities in each dimension of the velocity vector. The simplest triaxial model, a generalization of the isothermal sphere, uses a multivariate Gaussian to model the velocity distribution [42]. Again this model is truncated at $|\mathbf{v}| \geq \mathrm{v_{esc}}$ and for $|\mathbf{v}| < \mathrm{v_{esc}}$ is expressed as

$$f(\mathbf{v}) = \mathrm{N} \cdot \left[\exp\left(-\frac{\mathrm{v_r}^2}{\sigma_\mathrm{r}^2} - \frac{\mathrm{v}_\phi^2}{\sigma_\phi^2} - \frac{\mathrm{v_z}^2}{\sigma_\mathrm{z}^2} \right) \right]. \tag{1.8}$$

Following [30], this logarithmic ellipsoidal model can be parameterized by,

$$\sigma_{\mathrm{r}}^2 = \frac{\mathrm{v}_0^2}{(2+\gamma)(p^{-2}+q^{-2}-1)}, \tag{1.9}$$

$$\sigma_{\phi}^2 = \frac{\mathrm{v}_0^2 \cdot (2\mathrm{q}^{-2}-1)}{2(p^{-2}+q^{-2}-1)}, \tag{1.10}$$

$$\sigma_{\mathrm{z}}^2 = \frac{\mathrm{v}_0^2 \cdot (2\mathrm{p}^{-2}-1)}{2(p^{-2}+q^{-2}-1)}, \tag{1.11}$$

with the parameters describing the ellipse $q = 0.8$, $p = 0.9$ and the isotropy parameter $\gamma = -1.33$.

Another approach is to directly parameterize the mass distribution from N-body simulations of collisionless, self-gravitating particles. Projects such as Via Laceta [43], GHALO [44] and Aquarius [45], indicate that dark matter halo are not spherical and isotropic. A simple model has been proposed by [46] which can fit the simulated data for radial (r) and tangential (t) velocities with,

$$f(\mathrm{v_r}) = \frac{1}{\mathrm{N_r}} \exp\left[-\left(\frac{\mathrm{v_r}}{\bar{\mathrm{v}}_{\mathrm{r}}}\right)^{\alpha_{\mathrm{r}}}\right] \tag{1.12}$$

$$f(\mathrm{v_t}) = \frac{\mathrm{v_t}}{\mathrm{N_t}} \exp\left[-\left(\frac{\mathrm{v_t}}{\bar{\mathrm{v}}_{\mathrm{t}}}\right)^{\alpha_{\mathrm{t}}}\right] \tag{1.13}$$

with $\mathrm{v_t} = \sqrt{\mathrm{v}_\theta^2 + \mathrm{v}_\phi^2}$, N being the normalization of the distribution, $\alpha_r = 0.934$ and $\alpha_t = 0.642$ derived from the best fit [46]. As mentioned previously, various other models exist but in the scope of this work only this selection will be discussed.

1.6 Outline of this thesis

In this work, three different analysis related to the XENON100 experiment are presented. After an overview of the XENON100 detector and an explanation of the analysis procedure in chapter 2, various studies on the performance of the detector during the science run in 2013 and 2014 (science run 3) are presented (chapter 3). The main focus lies on the derivation of the size corrections for the charge signal explained in section 3.2. Following this, it is shown that by selecting double scattered photons from a mono-energetic calibration source, the electronic recoil energy scale for the secondary scintillation light can be derived (chapter 4). Finally a method is presented in chapter 5 to set limits of dark matter interactions to the target nucleus independently of astrophysical assumptions. The concluding statements can be found in chapter 6.

Chapter 2

The XENON100 experiment

At the time of writing, liquid xenon dual phase time projection chambers (TPC), e.g. the XENON100 and LUX experiments, set the benchmark sensitivity for spin independent and isospin conserving WIMP interactions. In this chapter the working principle of a TPC as well as the signal generation is explained in light of the XENON100 detector. Models to describe the microscopic processes leading to the observed signals are summarized. Finally, the basic event selection for WIMP searches as well as the analysis procedure for the XENON100 detector is summarized.

2.1 Enlighten the dark with XENON100

The XENON100 detector is optimized to search for seldom events by following a twofold strategy. Firstly, operating the target in an ultra-low background environment and, secondly, using a detector technology which is able to discriminate between electronic and nuclear recoils. In this section the setup of a liquid xenon dual-phase TPC is explained, using the XENON100 detector as an example.

2.1.1 Detection principle of a dual phase time projection chamber

A sketch of a liquid xenon (LXe) dual-phase TPC can be seen in the figure 2.2 (left) [47]. The detector consists of LXe, indicated by the white area, which is used as the target and of gaseous xenon at the top illustrated in light blue. A particle interaction in the liquid xenon produces direct scintillation photons as well as ionization electrons. The direct scintillation light (S1) is measured by the top and bottom photomultiplier (PMT) arrays. The walls of the TPC are made out of reflective PTFE panels in order to increase the probability that photons reach the PMT arrays. An applied potential between the cathode (15 kV) and grounded gate grid located at the bottom and top of the TPC, respectively, drifts the ionization electrons towards the gaseous phase. Electrons which reach the liquid-gas interface are extracted from the liquid phase by a strong extraction field between gate grid and the anode (4.4 kV), where the electrons are amplified through the effect of proportional scintillation [48], leading to the charge signal (S2). A field stronger than 10 kV/cm yields to a complete extraction of the drifted electrons. The time projection is given by the delay between the S1 and S2 signals due to the time that

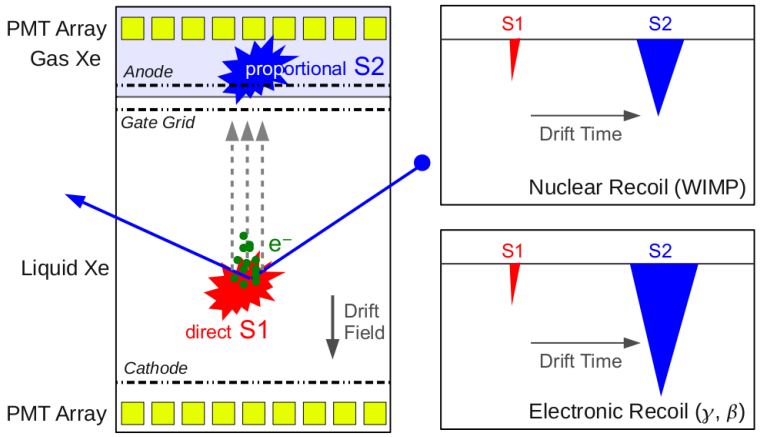

Figure 2.1: The left figure illustrates the working principle of the XENON dual-phase liquid-gas time projection chamber (TPC). See text for details. The waveforms at the right indicate the discrimination power between nuclear and electronic recoils due to the different ratio of light (S1) and charge (S2) signal [47].

it takes to drift the electrons to the gaseous phase. A measurement of the time difference defines the vertical position (Z) of the interaction vertex. The horizontal position (XY-coordinate) can be reconstructed from the S2 hit pattern on the PMTs at the top array. This enables a full three dimensional vertex resolution of 0.3 mm in Z and 3 mm in XY. The schematic waveforms at the right of figure 2.2 illustrate the discrimination power of a dual phase TPC. Due to the different S2 signal size with respect to S1 for nuclear or electronic recoils a discrimination parameter such as $\log\frac{S2}{S1}$ can discriminate different interactions inside the LXe (see section 2.4.2).

2.1.2 The XENON100 detector

The XENON100 detector is optimized to measure the S2 and S1 signals generated in a dual phase TPC filled with LXe. A more detailed sketch of the detector can be seen in figure 2.2 and a full description of all relevant detector components can be found in [47]. The cylindrical TPC is located inside a low-radioactivity stainless steal vessel which is not only shielded by various layers of copper, polyethylene and led, but is located at the underground laboratory at Gran Sasso (LNGS) in Italy to further reduce the surface muon flux by a factor of 10^6 [49]. The vessel is covered from the inside with highly reflective PTFE panels and is filled with a total of 161 kg of LXe, consisting of 62 kg in the active target and 99 kg for an active veto. Due to the active veto external background radiation can be further reduced in an offline analysis. To operate the TPC in two phases, the liquid level has to remain constant above the gate grid. This can be achieved by a diving bell located at the top which minimizes the impact of liquid density variations due to temperature changes as well as fluctuations in the gas recirculation rate. The constant gas recirculation enables a continuous purification of the gaseous xenon. Note that, the liquid-gas interface has to be parallel to the anode in order to maintain a homogeneous S2 amplification in the XY-plane.

The extraction field of $\sim$ 12 kV/cm is generated between the anode and gate grid

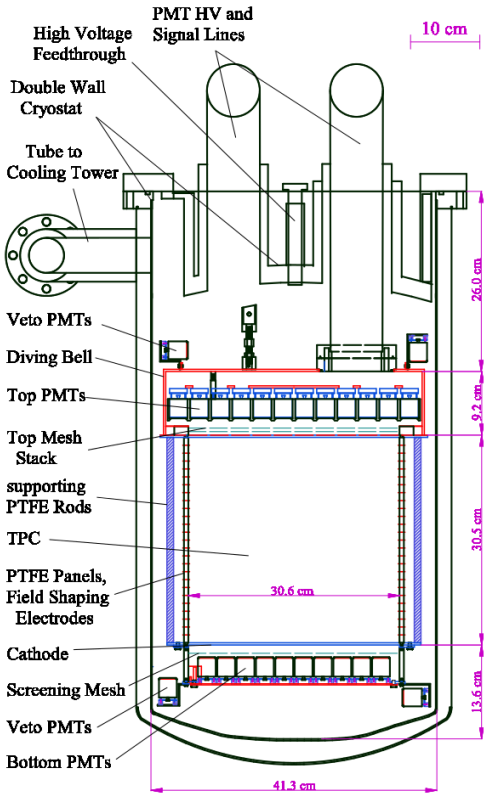

Figure 2.2: Drawing of the XENON100 detector and its components. For details see text and [47].

which are placed at a distance of 5 mm from each other. A drift field between the cathode and gate grid of 0.53 kV/cm drifts the electrons from the interaction vertex to the liquid-gas interface. To generate a homogeneous electric field across the 30 cm long TPC, 40 equidistant field shaping electrodes are placed around the TPC.

2.1.3 Data acquisition

The XENON100 data acquisition (DAQ) system digitizes the waveforms of the 242 PMTs and stores the data after each triggered pulse. At the typical background rate of approximately 1 Hz, the system runs with a negligible dead time due to an analog to digital converter (ADC) with a circular buffer of 512 kB memory per channel. An on-board field-programmable gate array (FPGA) allows to operate the ADCs in a mode where only the relevant part of the waveform is stored (zero-length-encoding) by still saving the relative position of all the peaks. The threshold for a signal in a single PMT is 4 mV corresponding to about 0.3 photoelectrons (PE).

The trigger is generated by using the signals of the 68 inner PMTs of the top arrays as well as 16 PMTs from the bottom center which are summed by a Fan-In/Fan-Out module. The DAQ system achieves at a S2 threshold of 150 PE a trigger efficiency of

more than 99 %. As mostly the S2 signal will trigger an event the corresponding S1 peak will be chronologically ahead. Therefore, the trigger is placed in the middle of the event window of 400 μs, more than twice of the maximal drift time of 176 μs at a drift field of 0.53 kV/cm. A more detailed description can be found in [47].

2.2 Signal generation in a two-phase xenon TPC

In general any interactions of a particle with liquefied noble gases result in an emission of luminescence, an ionization of the medium, and in heat. The emission of luminescence (scintillation) from liquid noble gases is attributed to the decay of excited dimers (excimers) to the ground state. For LXe, the wavelength of the scintillation of photons is centered at 177.6 nm [50]. LXe is at this wavelength transparent and the signal can be directly measured by PMTs. Excimers are produced by an initial interaction of a particle in LXe, generating excitions Xe^* which immediately form an excited dimer (excimer) Xe_2^* (equation 2.1) with the surrounding Xe atoms [50].

$$Xe^* + Xe \rightarrow Xe_2^* \tag{2.1}$$

$$Xe_2^* \rightarrow 2Xe + \gamma \tag{2.2}$$

The de-excitation of the excimer on timescales of few to tens of ns [50] results in the scintillation light (equation 2.2). These reactions produce directly the scintillation signal as illustrated by the blue box in figure 2.3. The charge particle moving in LXe produces

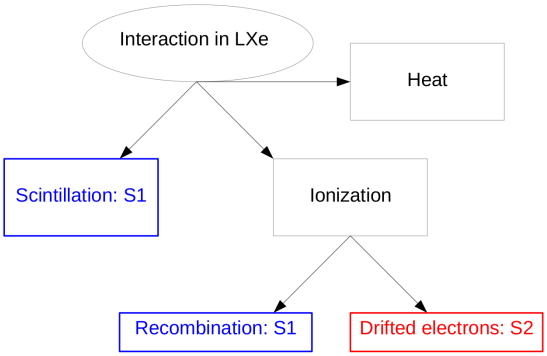

Figure 2.3: An energy deposition in LXe yields in a component of direct scintillation light, an local ionization of the medium and in an transformation into heat. Two competing processes within the ionized medium generate either further scintillation light due to recombinations or free electrons which can be amplified to the charge signal.

also an ionization of the medium, creating free electrons and Xe^+ ions (see equation 2.3). A part of the electrons are extracted from the locally ionized medium due to the applied drift field and, if they reach the gaseous phase at the top, are measured as the charge signal (red box in figure 2.3). However, some electrons might recombine (equation 2.4) at the interaction site and form again excitons and thus, enhancing the production of scintillation light (blue box in figure 2.3).

$$Xe^+ + Xe \rightarrow Xe_2^+ \tag{2.3}$$

$$Xe_2^+ + e^- \rightarrow Xe^{**} + Xe \tag{2.4}$$

$$Xe^{**} \rightarrow Xe^* + \text{heat}. \tag{2.5}$$

The remaining part of the initially deposited energy is converted into heat which can not be measured by the XENON100 detector (equation 2.5). An important process of these reactions is the distribution of recombining electrons, contributing partly to the total S1 signal, and escaped electrons (S2) since it depends not only on the initial energy deposition but differs for electronic and nuclear recoils (see section 2.2.1). If the number of directly produced excimers is small, the S1 and S2 signals are mainly generated according to the ionization processes in the medium. Note that a larger number of escaped electrons results directly in reduction of recombinations, and, hence, in an anti-correlation of the S1 and S2 signals.

2.2.1 Modelling of microscopic processes

Following the notation of [51], the generation of the S1 and S2 signal can be mathematically described by the number of produced photons N_{ph} (S1) and electrons N_e (S2). As seen in figure 2.3, the S1 signal is given by the number of direct excimers N_{ex} and ions N_i which can recombine with a probability r. Ignoring heat and assuming a 100 % efficiency for excited or recombined electrons to produce photons, the number of scintillation photons N_{ph} are given by

$$N_{ph} = N_{ex} + r \cdot N_i. \tag{2.6}$$

The number of ionization electrons N_e (S2) is then expressed with

$$N_e = N_i(1 - r). \tag{2.7}$$

Note that the ratio of excitions to ions, defined by $\alpha = \frac{N_{ex}}{N_i}$ differs for nuclear or electronic recoil but is assumed to be independent of the initial energy deposition [52]. For electronic recoil a value of $\alpha = 0.06$ indicates that the number of directly produced excimers generating the S1 signal is small [53]. For nuclear recoil, however, the value for $\alpha = 1.09$ is larger due to more directly produced excitons N_{ex} and an pronounced anti-correlation between S1 and S2 is not expected [54, 55].

The physical input enters in the calculation of the recombination probability r. The authors in [51] combine the models derived from Doke/Birks' Law [56, 57] and Thomas-Imel [58, 59] for high and low energy depositions, respectively.

Doke/Birks' Law The recombination probability r for long particle tracks and thus for high energy depositions (>15 keV at zero drift field) can be derived form Doke/Birks's law by considering two different processes of recombination,

$$r = \frac{A\frac{dE}{dx}}{1 + B\frac{dE}{dx}} + C. \tag{2.8}$$

The first term in equation 2.8 accounts for recombinations of electrons with ions other than its initial parent ion. The recombination probability depends on the density of charged ions which is given by energy loss per unit length $\frac{dE}{dx}$. The parameters A and B have to be determined experimentally. The second term C describes the probability for a immediate recombination of the produced electron-ion pair, also known as Onsager recombination [56].

Thomas-Imel model The Thomas-Imel model [58] describes short particle tracks and thus smaller energy depositions where the recombination probability r is given by,

$$\mathrm{r} = 1 - \frac{\ln(1+\xi)}{\xi}, \tag{2.9}$$

with $\xi = \frac{\mathrm{N_i}\beta}{4a^2v}$. Here N_i is total number of ions, β a constant dependent on ionization electron and hole mobilities and the dielectric constant, a is a length scale defining an ionization density volume and v is the mean electron velocity in the medium [58]. Note that in the Thomas-Imel regime the recombination probability is dependent on the absolute number of ions and not on the ionization density. Hence, in this model smaller energy depositions create less electron - ion pairs and result in a lower recombination probability. A lower light yield can not be explained by Doke/Birks' law since the dE/dx increases in general for low electron energies. At these energies, the signal consists of many different interaction sites at the scale of a few μm, triggered by X-rays and Auger electrons. The scintillation yield will remain constant for a given energy, because every possible way will always produce on average the same number of ions.

The NEST model The NEST model [51, 60] combines Doke/Birks's law and the Thomas-Imel model to fit measured data of the scintillation yield in LXe. The transition between the two models depends on the track length of initial particle and is defined by the mean ionization electron-ion thermalization distance of 4.6 μm in liquid xenon. Since the track length depends on the initial energy of the incoming particle, the two models describe the scintillation yield at high and low energy depositions, respectively. Measured data at zero drift field of the scintillation yield can be used to determine the free parameters of the two models. Figure 2.4 illustrates the absolute scintillation yield with respect to the incident gamma energy [51]. The Thomas-Imel model is shown by the dashed blue line and the Doke/Birks' Law as a dashed red line. In addition various experimental results are displayed. The reduced light yield at around $(30-35)$ keV can be explained by the production of low-energy Auger electrons which show typically an energy below < 10 keV [61]. At these energies the Thomas-Imel model dominates, explaining the reduced light yield. In addition at 29.8 keV, a K-shell X-ray is emitted which can travel far enough to create an own interaction site, resulting in a reduction of the recombination probability due to the independent interaction site [61].

2.3 Measuring process and data corrections

The detection of WIMP interactions in liquid xenon requires a detailed knowledge of the detector response for both the scintillation and charge signals. Once the different processes between the initial energy deposition and the observation of photoelectrons on the cathode in the PMTs is understood, corrections due to spatial inhomogeneities can be calculated and applied to the recorded signals. The details of the measuring process as well as the dominant data corrections will be explained in the following section. More details can be found in [62].

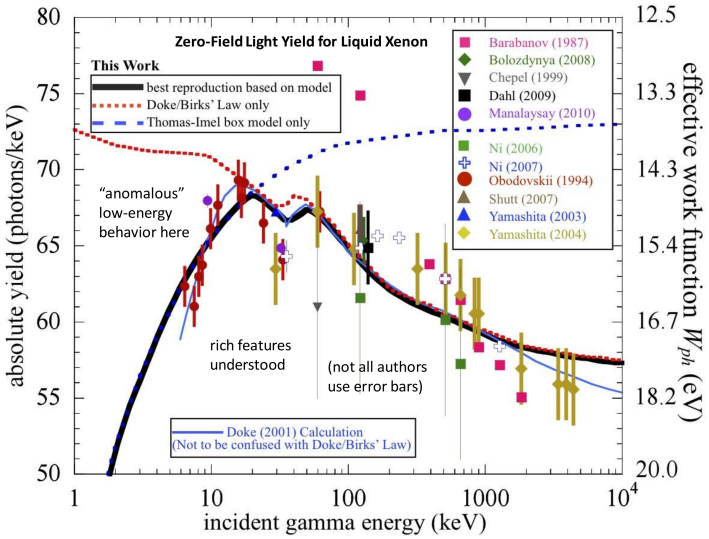

Figure 2.4: Various different measurements of the light yield for electronic recoils at zero drift field are indicated with the colored markers. In addition the Thomas-Imel model and the Doke/Birks' Law is shown by the dashed blue line and dashed red line, respectively. The black line displays a combined model where the transition takes place at around 15 keV. The dip at around 30 keV can be explained by the K-shell and Auger electrons of xenon. For more details see text. Figure from [51].

2.3.1 Scintillation signal

The scintillation signal can be used to estimate the deposited energy after an interaction in the active target. However, after the emission of the scintillation photons various effects of the detector and target medium reduce the signal as not all photons are detected. The expected S1 signal of a single PMT i ($\mathrm{s1_i}$) is a product of the expectation value for the number of photons $\mathrm{n_\gamma(E_u, \mathcal{E})}$, which depends on the drift field strength $\mathcal{E}$ as well as the deposited energy $\mathrm{E_u}$, and a parameter $\mu_\mathrm{i}(r)$, quantifying the detector response

$$\mathrm{s1_i(r) = n_\gamma(E_u, \mathcal{E})\mu_i(r)}. \tag{2.10}$$

The index u indicates either an interaction via a nuclear (nr) or electronic recoil (ee). The S1 signal is dependent on the vertex position r due to the finite attenuation length of LXe as impurities in the LXe remain. The limited reflectivity of the PTFE foil at the walls and finite transmissivity of the liquid-gas interface cause further photon losses. All these reductions of the observed light are quantified in the light collection efficiency (LCE). In addition the small probability of $(20-35)\,\%$ that a PMT converts a photon into a photoelectrons (quantum efficiency or QE) results in a PMT dependent reduction of observed photons. Also a PMT collects only $(70-90)\,\%$ of the created photoelectrons, which is defined by the collection efficiency CE. Thus the parameter μ_i is given for each PMT and event position by the product of QE, CE and LCE,

$$\mu_\mathrm{i}(\mathrm{r}) = \mathrm{LCE(r)} \cdot \mathrm{QE_i} \cdot \mathrm{CE_i}. \tag{2.11}$$

By summing over all PMTs in equation 2.10, the total expected scintillation signal can be written explicitly in terms of the deposited energy E_{nr} for nuclear recoils.

$$S1(r) = E_{nr} \times \mathcal{L}_y(E_{ee} = E_{ref}, \mathcal{E}, r) \times \mathcal{L}_{eff}(E_{nr}, \mathcal{E} = 0) \times \frac{S_{nr}(\mathcal{E})}{S_{ee}(\mathcal{E})}. \tag{2.12}$$

In this notation $\mathcal{L}_y(E_{ee} = E_{ref}, \mathcal{E}, r)$ is a parameter describing the light yield for a reference γ-line for a given electric drift field and event position. The function $\mathcal{L}_{eff}(E_{nr}, \mathcal{E} = 0)$ is the relative scintillation yield of nuclear recoils with respect to the reference γ-ray line at 122 keV and zero field. This energy scale will be explained in more detail in the section 2.5. The scintillation quenching due to the electric drift field $\mathcal{E}$ are accounted for by the factors S_{nr} and S_{ee} for nuclear and electronic recoil, respectively. The light yield in XENON100 is $\mathcal{L}_y = (2.28 \pm 0.04)\,\mathrm{PE/keV_{ee}}$ [15]. To derive a S1 value independently of the vertex position due to inhomogeneities in LC and CE, it is necessary to apply a correction to the integrated S1 signal (S1 size). This can be done by measuring the S1 size in small sub-volumes of the TPC from a mono-energetic calibration source at the relevant drift field. By applying this correction to each event, the light yield is averaged over the hole TPC and the S1 size is independent of the position. The corrected scintillation signal cS1 can be written as

$$cS1 = E_{nr} \times \langle \mathcal{L}_y(E_{ee} = E_{ref}, \mathcal{E}) \rangle \times \mathcal{L}_{eff}(E_{nr}, \mathcal{E} = 0) \times \frac{S_{nr}(\mathcal{E})}{S_{ee}(\mathcal{E})}. \tag{2.13}$$

However, in the process of generating the scintillation light and observing a signal in the PMTs, unavoidable statistical variations occur and the measured S1 value will follow a continuous distribution. The probability density function (pdf) for the S1 signal (p_{cS1}) consists of a Poisson-distributed number of generated photons n_γ [1]. This can be explained by the combined effect of the LCE and QE, which results in the detection of only a few percent of the initial emitted photons, especially at energy depositions of only a few keV. The low number of observed photons justifies the important assumption of a Poisson-distributed process. In addition, the response of a PMT i to an observed S1 signal can be approximated by a Gaussian function with the mean $N_{pe,i}$ and width $\sigma_{PMT}\sqrt{N_{pe,i}}$ where N_{pe} is the number of photoelectrons recorded by the PMTs.

$$p_{cS1}(cS1|n_\gamma(E, \mathcal{E}_u))dcS1 = \sum_{N_{pe}} p_{pmt}(cS1|N_{pe}) \times Poiss(N_{pe}|\langle\mu\rangle n_\gamma)dcS1 \tag{2.14}$$

2.3.2 Ionization signal

The charge signal seen by a PMT i ($s2_i$) is initially generated by the extracted electrons from the ionized medium caused by an energy deposition. Due to the drift, field they travel through the LXe towards the liquid-gas interface in a time t_d. Not all electrons reach the top as they can attach to electronegative impurities. This is quantified by a characteristic lifetime τ_e. Electrons reaching the surface are lifted from the LXe into the gaseous phase by an extraction field $\mathcal{E}_{gas}$ with a yield κ. The extracted electrons are accelerated by the $\mathcal{E}_{gas}$ field and scatter with the surrounding gas atoms, resulting in the

[1] To be consistent with equation 2.6: $N_{ph} \equiv n_\gamma$

proportional scintillation light signal (S2) [48]. The amplification of the charge signal is expressed by a factor Y (secondary scintillation gain) which depends on the gas density ρ and the space between the liquid level and anode, defining the gas gap $\mathrm{h_g}$. A further dependency of the xy-position of Y can be induced by an inclined liquid level or a warping of the gate grid or anode. $\beta_i(x, y)$ accounts for the probability for a photon created at the position (x,y) in the gas phase to be observed by the PMT i. The vertical position z can be neglected as the S2 signal is generated within the narrow gas gap $\mathrm{h_g} = 2.5\,\mathrm{mm}$. The QE for a single PMT is described by η_i

$$\mathrm{s2_i(r)} = \mathrm{n_e(E_u, \mathcal{E})} \times \mathrm{e^{-t_d/\tau_e}} \times \kappa(\mathcal{E}_\mathrm{gas}) \times \mathrm{Y}\left(\frac{\mathcal{E}\mathrm{gas}}{\rho}, \mathrm{h_g}\right) \times \beta_\mathrm{i}(\mathrm{x, y}) \times \eta_\mathrm{i}. \tag{2.15}$$

Similar to the scintillation light, the position dependence of the S2 signal can be removed by applying correction to the measured signal. A correction map $\delta(\mathrm{x, y})$ can be calculated from a gamma calibration source (see chapter 3). With this method $\delta(\mathrm{x, y})$ is given by

$$\delta(\mathrm{x, y}) = \kappa(\mathcal{E}_\mathrm{gas}) \times \mathrm{Y}\left(\frac{\mathcal{E}_\mathrm{gas}}{\rho}, \mathrm{h_g}\right) \times \beta_\mathrm{i}(\mathrm{x, y}) \times \eta_\mathrm{i}. \tag{2.16}$$

Summing over all PMTs in equation 2.15 and writing the S2 signal explicitly in terms of the deposited energy for nuclear recoils, S2 is given by

$$\mathrm{s2_i(r)} = \mathrm{E_{nr}} \times \mathcal{Q}_\mathrm{y}(\mathrm{E_{nr}}) \times \mathrm{e^{-t_d/\tau_e}} \times \delta(\mathrm{x, y}), \tag{2.17}$$

where $\mathcal{Q}_y(\mathrm{E_{nr}})$ is the measured charge yield of nuclear recoils at the given electric field. The correction for the electron lifetime $e^{-\mathrm{t_d}/\tau_\mathrm{e}}$ varies with time as the purity level increases due to a constant purification procedure to remove the electronegative impurities. The pdf for the S2 signal can be constructed as in equation 2.14.

$$p_\mathrm{cS2}(\mathrm{cS2|n_e(E, \mathcal{E}_u)})\mathrm{dcS2} = \sum_{\mathrm{N_{pe}}} \mathrm{p_{pmt}(cS2|N_{pe})} \times \mathrm{Poiss(N_{pe}|\delta n_e)dcS2} \tag{2.18}$$

2.4 Event selection and recoil discrimination

The trigger system records events in the absence of a calibration source at a rate of around 1 Hz. This rate is clearly not caused by WIMP interactions but by events triggered from remaining background. Thus, it is crucial to find selection criteria which can be extracted from the waveform to select WIMP-like events in an offline analysis. With LXe as a target it is possible to discriminate between electronic and nuclear recoils, enabling a much higher sensitivity for WIMP searches. This section gives an overview of the event selection in XENON100 and an explanation of the recoil discrimination.

2.4.1 Event selection

In general, the dark matter event selection criteria try to identify events which are caused by a physical interaction of a particle inside the sensitive area of the TPC and deposits its energy in a single vertex. Various different conditions have been investigated and the most important ones are summarized below.

Basic data quality Electronic noise measured by the PMTs consists of random fluctuation of the baseline and is sometimes recognized as a event by the data processing system. This can happen within the waveform of a good event or can accidently mimic an valid interaction pattern. The former waveform can be avoided by a condition based on the signal-to-noise ratio which requires that the main contribution to the size of the S1 an S2 peaks is caused by the largest S1 and S2 peak in the waveform. The latter waveform can be tagged by a condition on the width of the S1 peaks as well as by too large fluctuations in a waveform. In addition, any energy deposition in the LXe causing a S1 signal must be observed by at least 2 individual PMTs within a time window of 20 ns and a threshold of 0.35 PE.

Single scatter events The selection of single scatter events gives rise to a condition for both S1 and S2 signals. If more than one S1 peak is present in a waveform it is a clear evidence that more than one physical process happened in the 400 μs time window. However, this requirement is not sufficient since a double scattered photon would produce two S1 signals but would be reconstructed by a single S1 peak due to the too long decay time of the excited xenon states. To require only one S2 peak would be too restrictive, since a non negligible amount of single electron events [63] are present after an energy deposition in the LXe. These events show a rather small and well understood S2 peak size and a threshold condition on the size of the second largest S2 peak as a function of the largest S2 peak is sufficient to select single scatter events.

Active veto An active veto is installed around the inner TPC with a 4π coverage. The veto-PMTs record events and waveforms similar to the inner PMTs, but with a higher energy threshold due to a reduced PMT coverage and lower light collection efficiency. Since it is very unlikely that WIMP scatter once in the veto and inside the active target, measured S1 signals in the veto and the inner TPC within $\pm$ 20 ns are most probable caused by background.

Detector threshold condition As described in section 2.1.3 the trigger efficiency decreases for low energy depositions resulting in small S2 peaks. In order to maintain a close to 100 % efficiency a threshold condition on the S2 size is necessary. It is important to realize that this threshold defines directly the energy threshold of the XENON100 detector and thus the sensitivity to low mass WIMP interactions. This threshold was set to $>$ 300 PE and $>$ 150 PE for the analysis in [64] and [65], respectively. In addition, a threshold energy for the S1 signal is set to 4 PE in science run I and was reduced to 3 PE in run II.

Fiducial volume Due to the high vertex resolution of a dual-phase TPC, the position of an interaction can be used to discriminate between background and possible WIMP events. The active target of the XENON100 detector consists of 62 kg of LXe. Most of the radioactive elements causing the background can be found close to the TPC walls. Thus it is possible to decrease background events by selecting the purest inner part of the TPC avoiding events in vicinity of the walls and, thus, exploiting the self shielding capability of LXe. The inner 48 kg and 34 kg have been used in the analysis of [64] and [65], respectively.

Consistency cuts To reconstruct the XY-position of an interaction from the top PMT pattern, various algorithms have been tested. Even though an algorithm based on a neural network shows the best performance large discrepancies between the algorithms are not expected. A consistency condition is fulfilled if the reconstructed positions agree within the uncertainties. Also a condition on the S2 peak width can be used to select WIMP-like events.

2.4.2 Event discrimination

A dual phase TPC enables to observe not only the scintillation signal, but also amplifies the produced electrons in an interaction to an measurable charge signal. The ratio of two measured signals differs for electronic and nuclear recoil, enabling a discrimination between different recoils (see section 2.1.1). Figure 2.5 illustrates events in the parameter space of the flattened discrimination parameter $\log_{10}(S2_b/S1)$ with respect to the S1 signal and deposited energy. The flatted variable is calculated by subtracting the distributions mean and the parameter $S2_b$ denotes the S2 light measured by the bottom PMT array only. Note that in the most recent XENON100 analysis [64, 65] only the S1 signal is used to estimate the energy. The blue points indicate events from electronic recoils

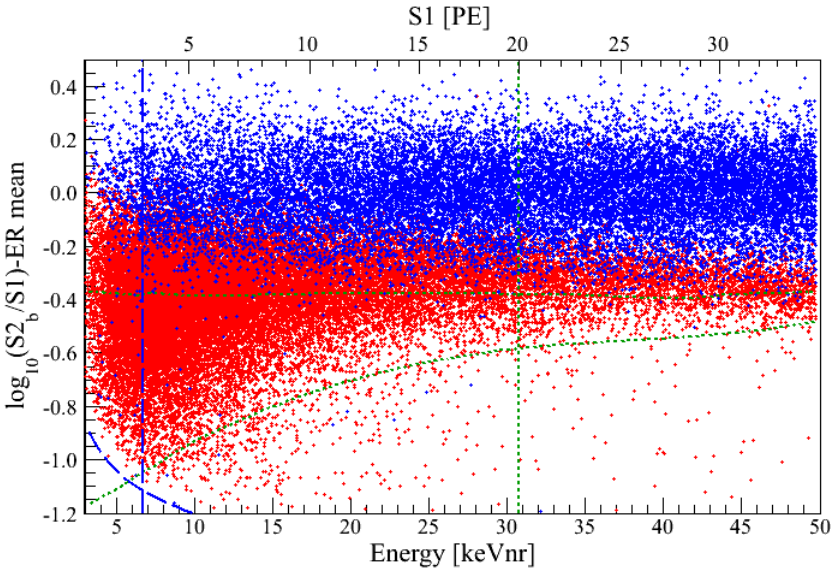

Figure 2.5: Events produced by electronic recoils (blue) and nuclear recoils (red) in the discrimination space $\log_{10}(S2_b/S1)$ with respect to the S1 size and energy. It can be seen that the mean ratio of S2/S1 for electronic recoil is larger than for nuclear recoil, which enables a discrimination between the two interaction types. For more details see. Figure taken from [65].

measured with a ^{60}Co and ^{232}Th calibration sources and in red events due to nuclear recoils produced by a AmBe neutron source. It can be seen that for electronic recoil the average ratio S2/S1 is larger than for nuclear recoil, and, by exploiting this fact, can be used to discriminate between these different interactions. The curved blue dashed line at the lower left shows the impact of the S2 threshold condition which selects only events above 150 PE. The curved lower green line displays the minimal allowed values

of the discrimination parameter calculated from the $3\,\sigma$ contour of the neutron band. As a cross check to the profile likelihood analysis [66], a method using an upper limit (horizontal green dashed line) at 99.75 ER rejection for the $\log_{10}(S2_b/S1)$ value is used to define the benchmark WIMP region from above. The green vertical dashed lines at $6.6\,\mathrm{keV_{nr}}$ (3 PE) and $30.5\,\mathrm{keV_{nr}}$ (20 PE) indicate the lower and upper energy threshold in S1 for the benchmark region, respectively.

The different S2/S1 ratios can be explained by the parameter $\alpha = \frac{N_{ex}}{N_i}$ introduced in section 2.2. For electronic recoil it was shown that $\alpha = 0.06$ and for nuclear interactions $\alpha = 1.09$, indicating a larger production of excitions in case of a nuclear recoil. A higher number of directly produced excitons leads to a larger S1 signal, explaining the lower value of $\log_{10}(S2_b/S1)$ for nuclear recoils.

2.4.3 Calibration sources

Various radioactive sources are used to calibrate the XENON100 detector. Due to the shield of the detector against external radiation, a dedicated pipe is necessary to place the radioactive sources as close as possible to the TPC. Therefore, a low radioactive copper pipe is placed through the shield and follows the circular shape of the TPC as it is displayed in figure 2.6. The point sources can be placed in the pipe through a stiff

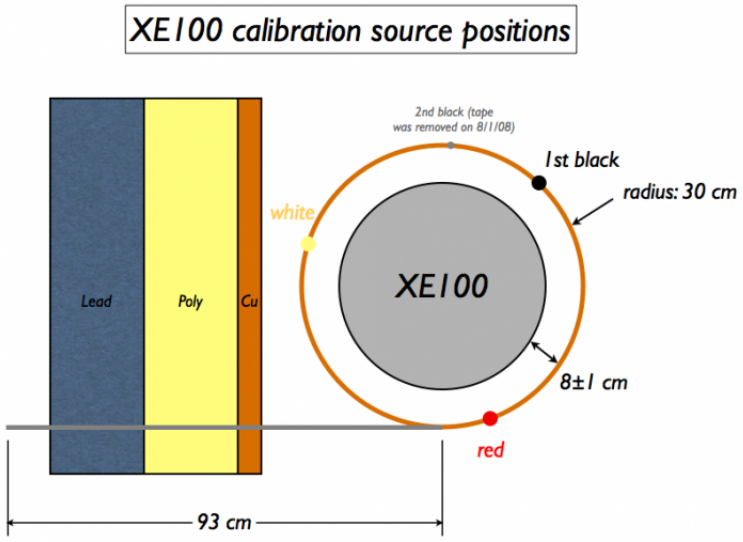

Figure 2.6: The XENON100 detector can be calibrated by placing radioactive sources through a small pipe close to the TPC.

wire at three different positions. The ^{232}Th source is not a point source but consists of a thoriated wire in order to achieve a homogeneous calibration in the XY plane. A list of the available energy lines due to electronic recoil can be found in table 2.1. Note that all the listed decay modes generate gamma rays.

The background expectation for the dark matter analysis due to electronic recoil is determined from ^{60}Co and ^{232}Th sources (see figure 2.5). To test WIMP like interactions

in the fiducial volume, an AmBe neutron source is used. It produces a spectrum of nuclear recoils which can be used to define a benchmark region for WIMP searches. Furthermore, by using neutron interactions as a model for WIMP scatters, the acceptance of the dark matter event selection can be computed with the AmBe calibration (see figure 2.5).

Isotope	Energy [keV]	Half-life	Decay mode
^{129}Xe	39.6	0.97 ns	γ
^{131}Xe	80.2	0.48 ns	γ
^{19}F	109.9	0.6 ns	γ
^{131m}Xe	163.9	11.8 d	γ
^{19}F	197.1	89 ns	γ
^{129m}Xe	236.1	8.9 d	γ
^{129}Xe	319.9	$\sim$ ps	γ
^{137}Cs	661.6	30 a	γ
^{60}Co	1173.2	5.27 a	γ
^{60}Co	1460.8	5.27 a	γ
^{232}Th	4803	$1.405 \cdot 10^{10}$ a	decay chain with γ's

Table 2.1: The table lists the available calibration lines produced by electronic recoils in XENON100 [61].

Due to inelastic scattering of neutrons with ^{129}Xe and ^{131}Xe, the xenon nuclei can be excited during an AmBe neutron calibration. Ensuing de-excitations result in the emission of a photons with various energies as shown in figure 2.7 in terms of S1 and S2. The color coded scale indicates the number of events in each bin. The half life's of these excited states are below 1 ns and an ensuing decay results in an emission of a 40 keV and 80 keV photon. It is to mention that the neutron not only excites the nucleus but transfers some momentum to the atom, which results in a small variation of the light and charge yield due to the contribution of a nuclear recoil. In addition, the neutrons interact with the Teflon of the TPC which contains fluorine. Similar to ^{129}Xe and ^{131}Xe states, the ^{19}F creates prompt photons with an energy of 109.9 keV and 197.1 keV. Note, that the 109.9 keV line can not be clearly resolved due to its vicinity to the 80 keV γ from ^{131}Xe. As events due to ^{19}F mainly interact with the LXe at the boarder of the TPC, these lines can be avoided by restricting the fiducial volume to the inner part of the TPC.

The meta stable states ^{129m}Xe and ^{131m}Xe are also generated during the AmBe calibration, however, their half life is much longer and no coincident nuclear recoil is present. The decay to the ground state emits an γ with 164 keV and 236 keV. Note that the ^{129m}Xe decays through two transitions until it reaches the ground state by emitting an 196 keV and 40 keV γ summing up to 236 keV. This results to an differing charge and yield light than a monoenergetic 236 keV line as the energy scale varies with energy. A superposition of a 318 keV and 321 keV γ from ^{129}Xe is visible at around 319.9 keV (weighted mean).

The ^{137}Cs calibration source is usually used to estimate the electron lifetime which is measured once or twice per week (see section 2.3.2).

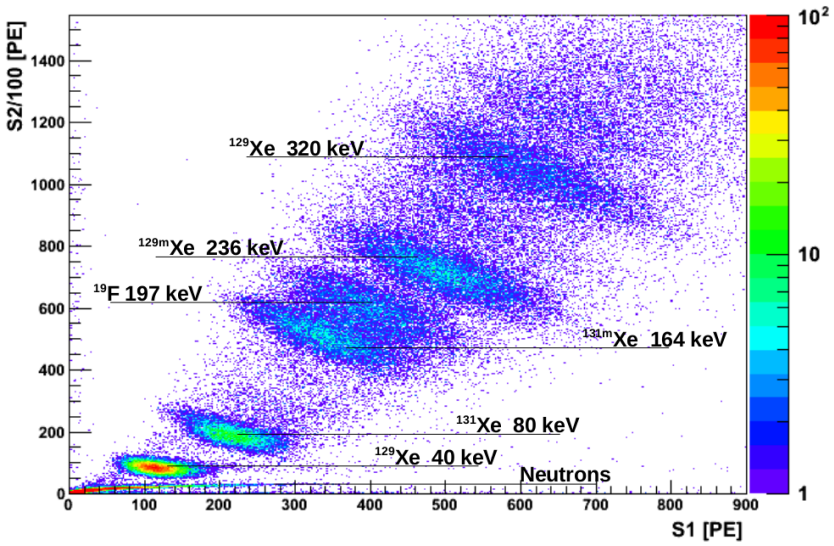

Figure 2.7: Events measured during a AmBe neutron calibration in terms of the corrected S2 and S1 signals. At very low values of S2 the neutron band is visible. The 40 keV and 80 keV lines are caused by the inelastic scattering of neutrons on ^{129}Xe, ^{131}Xe, respectively. The energy positions at 164 and 236 keV are explained by the decay of the meta stable ^{131m}Xe and ^{129m}Xe to the ground state. Due to neutron interactions with the surrounding material, a γ from ^{19}F with an energy of 197 keV can be observed. A superposition of a 318 keV and 321 keV γ from ^{129}Xe is visible at around 319.9 keV (weighted mean).

2.4.4 Acceptances

The event selection criteria described in section 2.4.1, try to identify events which are expected to be caused by nuclear recoils from WIMP interactions. Even though the conditions are optimized on nuclear recoil data, not all nuclear recoil events are selected and the loss is quantified by the so called acceptance. The acceptance of a selection criterium is estimated by applying the condition on the AmBe-neutron calibration data and an computation of the selected neutron events. The desired acceptance of 1 means, that the criterium selects all WIMP like events.

In XENON100 three different acceptances need to be computed and are shown in figure 2.8 representing the published results in [64] (left) and [65] (right). The red line displays the S2 threshold acceptance in terms of S1 and the blue line shows the combined acceptances of all event selection criteria including the neutron acceptance for the benchmark region (see figure 2.5). The right figure shows the same acceptances for science run II, but the benchmark WIMP region acceptance (green) and the acceptances of the event selection (blue) are shown individually.

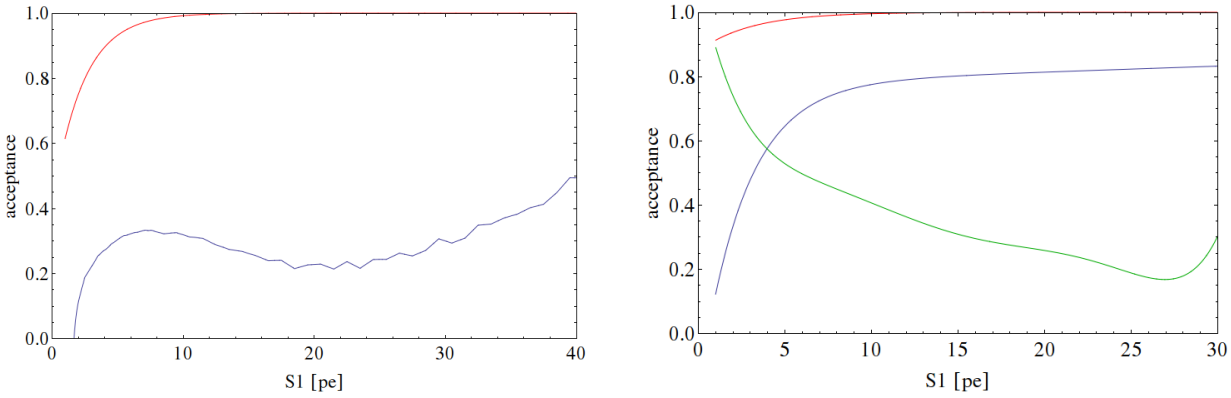

Figure 2.8: Cut acceptances as published in science run I ([64]) and science run II ([65]) in the left and right plot, respectively. The red lines show the S2 threshold acceptances. The blue line in the left plot indicates the combined cut acceptances as well as the acceptance of neutrons due to the 99.75 % discrimination level. For science run II (right), the green line shows the neutron acceptance due to the 99.75 % discrimination level as well as the combined event selection acceptances (blue).

2.5 Energy scales

For calorimeters it is essential to be able to relate the measured signal to the initial deposited energy. In general, this relation can be measured with calibration sources or a detailed Monte Carlo simulation of all relevant physical processes. However, a simulation is always based on assumptions and a verification by measured data should be performed. This section gives a short summary of the available energy scales for nuclear and electronic recoil which are relevant for XENON100.

Energy scales for nuclear recoils The most important energy scale used for the WIMP analysis in [64, 65], converts the measured S1 signal into the energy scale for nuclear recoils. This quenching function ($\mathcal{L}_{\text{eff}}$) is introduced in equation 2.12 and shown in the left plot of figure 2.9. It describes the relative scintillation yield of nuclear recoils as a function of the energy with respect to the reference γ-ray line (122 keV) at zero drift field. In addition to the various existing measurements the black line illustrates the parameterization of measured data points used for the XENON100 analysis. Below 3 keV no measured data exists and has to be extrapolated to 0. Since the XENON100 is operated at 0.53 keV/cm and by assuming that the drift field changes only the absolute values of the relative scintillation yield, $\mathcal{L}_{\text{eff}}$ is anchored to the light yield at 122 keV via $\mathcal{L}_{\text{y}}$.

The right plot in figure 2.9 displays the charge yield $\mathcal{Q}_y(\text{E}_{\text{nr}})$ for nuclear recoils as a function of the energy [68].$\mathcal{Q}_y$ was introduced in equation 2.17 to convert measured S2 signals to the deposited energy. No direct measurements at the relevant drift field exist at the time of writing, however the charge yield can be calculated by a Monte Carlo simulation of the AmBe neutron source which is used to calibrate the XENON100 detector. In the work [68] an absolute matching of the measured and simulated neutron energy spectrum is achieved, confirming the validity of the simulation. Note that this energy scale is essential to extend the presented analysis in [64, 65] to an energy estimation

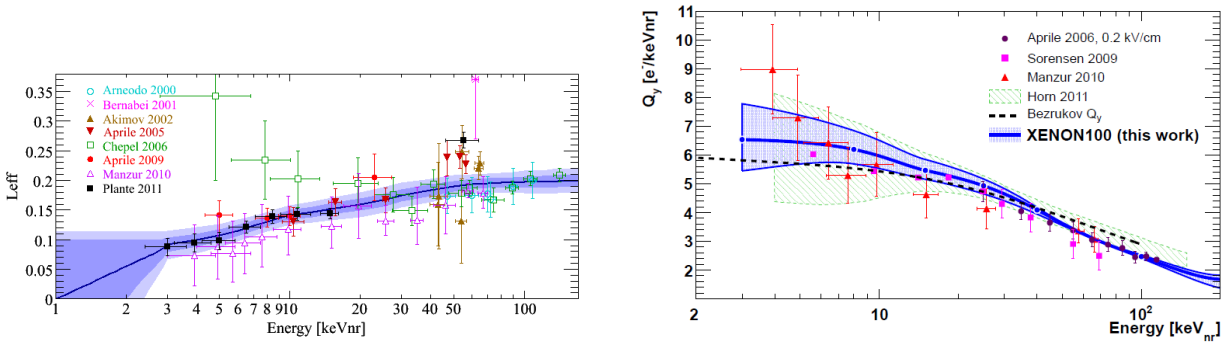

Figure 2.9: The left plot shows various measurements of the relative scintillation yield of nuclear recoils with respect to the 122 keV γ line at zero drift field ($\mathcal{L}_{\text{eff}}$). In blue the Gaussian mean at $1\,\sigma$ and $2\,\sigma$ as well as the parameterization used for the analysis is illustrated [67]. Measurements of the charge yield $\mathcal{Q}_y$ can be seen in the left figure. Only a few measurements at different drift fields are available. A determination of $\mathcal{Q}_y$ at the relevant drift field for XENON100 is possible by a Monte Carlo simulation of the AmBe neutron source and shown in blue [68].

using both the S1 and S2 signal.

Energy scales for electronic recoils The energy scale for electronic recoil is not relevant for WIMP searches, however necessary for an analysis of the annual modulation signal in the electronic recoil band or other dark matter models producing electronic recoil such as axions (see section 1.2). The quenching of the scintillation signal with an applied drift field of 0.45 kV/cm has been measured by eg. [69] which is shown in the left plot of figure 2.10. Also the semi-empirical model (NEST) introduced in section 2.2.1 is displayed by the green line. Due to the low $\alpha = 0.06$ value of electronic recoil, the S1 and S2 signals show an anti-correlation. By assuming that losses during the S1 and S2 signal generation are not dependent on the energy, it is possible to calculate the charge yield from the scintillation yield which is shown for different drift fields in the right of figure 2.10. It can be seen that a stronger drift field enhances the charge yield, as more electrons are drifted from the ionized xenon.

2.6 Dark matter analysis

In chapter 1 the expected differential scattering rate (equation 1.5) of WIMPs in direct detection experiments is derived. However this equation has to be modified according to the detector response to nuclear recoils (see section 2.3). In addition, it is necessary to account for the acceptances of the various event selection criteria. A summary of the observed primary scintillation signal caused by an interaction in the LXe, described in section 2.3, can be seen in figure 2.11. The black boxes indicate the different units and distributions during the conversion of deposited energy to the expected number observed photoelectrons in the PMTs. The red boxes label the different parameters and distributions which are necessary for the calculation. The acceptances (blue) are applied to the expected number of photons in the last step (4) of the calculation, except the one

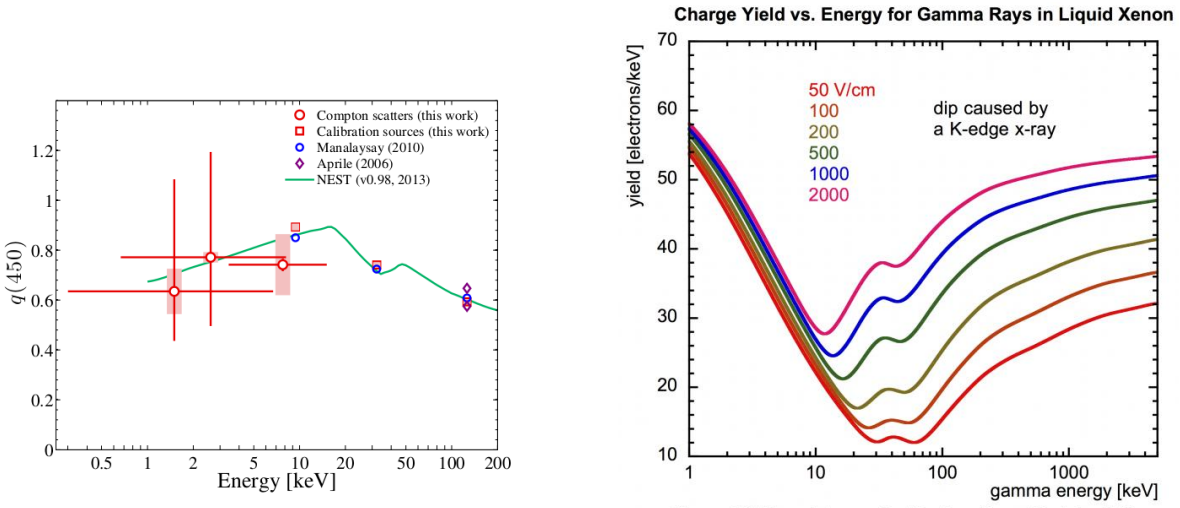

Figure 2.10: Various measurements of the quenching of the scintillation signal due to electronic recoil with an applied drift field of 0.45 keV/cm is shown in the left plot. The green line indicates the semi-empirical prediction of the NEST model [69]. In the absence of a direct measurement of the charge yield for electronic recoils the right plot shows only the NEST predictions for different drift fields [60].

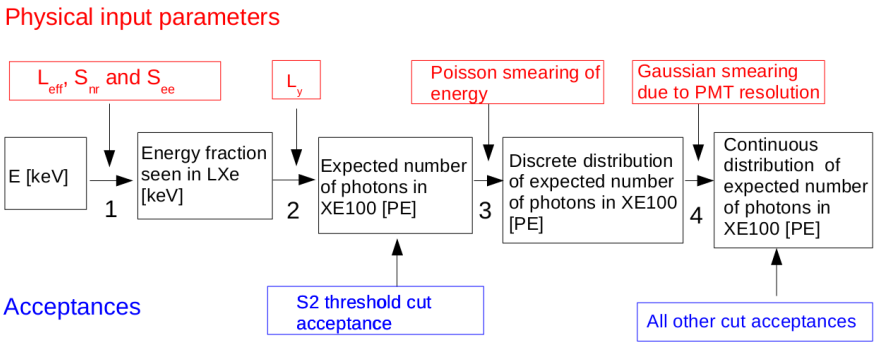

Figure 2.11: Sketch of the analysis procedure in XENON100 in terms of S1. The black boxes label the different parameters which arise by a conversion the deposited energy into an expected number of photons. The red boxes indicate the relevant physical parameters which are necessary for the calculation. The acceptances are applied to different parameters during the conversion and are shown in blue.

for the S2 threshold condition. It has to be applied before the Poisson smearing since the S2 signal fluctuates independently from S1 after the initial energy deposition. This procedure is mathematically described below and in more detail in [66].

The total number of detected signal events N_s in the interval $[S1_{min}, S1_{max}]$ can be

calculated by the integral

$$\mathrm{N_s} = \int_{\mathrm{S1_{min}}}^{\mathrm{S1_{max}}} \mathrm{dS1} \frac{\mathrm{dR}}{\mathrm{dS1}}(\mathrm{m}_\chi), \tag{2.19}$$

where $\frac{\mathrm{dR}}{\mathrm{dS1}}$ denotes the WIMP energy spectrum as a function of the dark matter mass m_χ. Since the number of detected photoelectrons (n) at the PMTs fluctuate, the expected S1 signal is smeared according to the response of the PMTs. For the XENON100 PMTs the number of photoelectrons are smeared according to a Gaussian distribution with a mean value of n and width of $\sqrt{\mathrm{n}}\sigma_{\mathrm{PMT}}$, where $\sigma_{\mathrm{PMT}} = 0.5$ is experimentally determined [66]. In addition, the event selection acceptance in terms of S1 is denoted by $\epsilon(S1)$, and leads to

$$\frac{\mathrm{dR}}{\mathrm{dS1}} = \mathrm{Gauss}(\mathrm{S1}|\mathrm{n}, \sqrt{\mathrm{n}}\sigma_{\mathrm{Pmt}}) \cdot \frac{\mathrm{dR}}{\mathrm{dn}} \cdot \epsilon(\mathrm{S1}). \tag{2.20}$$

Combining 2.19 and 2.20 yields,

$$\mathrm{N_s} = \int_{\mathrm{S1_{min}}}^{\mathrm{S1_{max}}} \mathrm{dS1} \cdot \mathrm{Gauss}(\mathrm{S1}|\mathrm{n}, \sqrt{\mathrm{n}}\sigma_{\mathrm{Pmt}}) \cdot \frac{\mathrm{dR}}{\mathrm{dn}} \cdot \epsilon(\mathrm{S1}). \tag{2.21}$$

In order to express $\frac{\mathrm{dR}}{\mathrm{dn}}$ in terms of the deposited energy E, one needs to consider a Poissonian distribution due to the small number of observed photons (see section 2.3)

$$\frac{\mathrm{dR}}{\mathrm{dn}} = \int_0^\infty \mathrm{dE} \cdot \frac{\mathrm{dR}}{\mathrm{dE}} \cdot \mathrm{Poiss}(\mathrm{n}|\nu(\mathrm{E_{nr}})), \tag{2.22}$$

with the energy expectation value

$$\nu(\mathrm{E_{nr}}) = \mathrm{E_{nr}} \cdot \mathcal{L}_{\mathrm{eff}} \cdot \frac{\mathrm{S_{nr}}}{\mathrm{S_{ee}}} \cdot \mathrm{L_y}. \tag{2.23}$$

The values for the scintillation quenching factors are $S_{nr} = 0.95$ and $S_{ee} = 0.58$, for nuclear and electronic recoil, respectively [70]. The relative scintillation efficiency is expressed by $\mathcal{L}_{eff}$ and the normalization light yield at 122 $\mathrm{keV_{ee}}$ is measured to $\mathrm{L_y}(122\,\mathrm{keV_{ee}}) = (2.28 \pm 0.04)\,\mathrm{PE/keV}$ [65].

Combining all results from above we can derive an equation for the total number of observed events N as function of the deposited energy E.

$$\mathrm{N_s} = \int_{\mathrm{S1_{min}}}^{\mathrm{S1_{max}}} \mathrm{dS1} \cdot \epsilon(\mathrm{S1}) \cdot \int_0^\infty \mathrm{dE_{nr}} \cdot \sum_{\mathrm{n}=1}^{\infty} \left(\frac{\mathrm{dR_{A,Z}}}{\mathrm{dE_{nr}}} \cdot \frac{\nu(\mathrm{E_{nr}})^{\mathrm{n}}}{\mathrm{n!}} \cdot \mathrm{e}^{-\nu(\mathrm{E_{nr}})} \right) \frac{1}{\sqrt{2\pi n} \cdot \sigma_{\mathrm{PMT}}} \cdot e^{\frac{-(\mathrm{n}-\mathrm{S1})^2}{2\mathrm{n}\sigma^2_{\mathrm{PMT}}}}. \tag{2.24}$$

2.7 Scientific results of the XENON100 detector

In the quest of a direct detection of dark matter, the XENON100 results of the two main science runs lasting 100 live days [64] and 225 live days [65] are summarized in [62] and shown again in table 2.2. Two independent methods are used to interpret the data in terms of dark matter interactions. Bounds on the cross section with respect to the dark matter mass are derived by a profile likelihood method [66] which takes not only the

exact distribution of background events into account but enables a profiling of systematic uncertainties. A pre-defined benchmark region allows, additionally, to constrain dark matter interactions by different methods such as the Feldman and Cousin [71] approach. These results can be used to interpret the absence of a signal in terms of different dark

	Run-I	Run-II
Live days [d]	100	225
PL ROI [PE]	$(4-30)$	$(3-30)$
PL ROI [$\mathrm{keV_{nr}}$]	$(8.4-44.6)$	$(6.6-43.3)$
Benchmark ROI [PE]	$(4-30)$	$(3-20)$
Benchmark ROI [$\mathrm{keV_{nr}}$]	$(8.4-44.6)$	$(6.6-30.5)$
S2 threshold [PE]	300	150
Benchmark ER discrimination	99.75 %	99.75 %
Benchmark NR lower contour	$\sim 3\,\sigma$	$\sim$ 97 %
Fiducial mass [kg]	48	34
Expected background events in benchmark ROI	1.8 ± 0.6	1.0 ± 0.2
Measured events in benchmark ROI	3	2

Table 2.2: Summary of the XENON100 analysis parameters from science runs I and II. The PL abbreviates the profile likelihood method. For comparison to the PL analysis, parameters of a pre-defined benchmark region are also stated [62].

matter models which predict nuclear recoils. Bounds on spin independent and isospin conserving WIMP interactions can be seen in figure 1.1, where the XENON100 results showed for over 3 years the worlds best sensitivity on the WIMP - nucleus cross section. However, the data shown in table 2.2 can also be interpreted in terms of spin dependent interactions to protons and neutrons [15] which are shown in figure 2.12. The spin

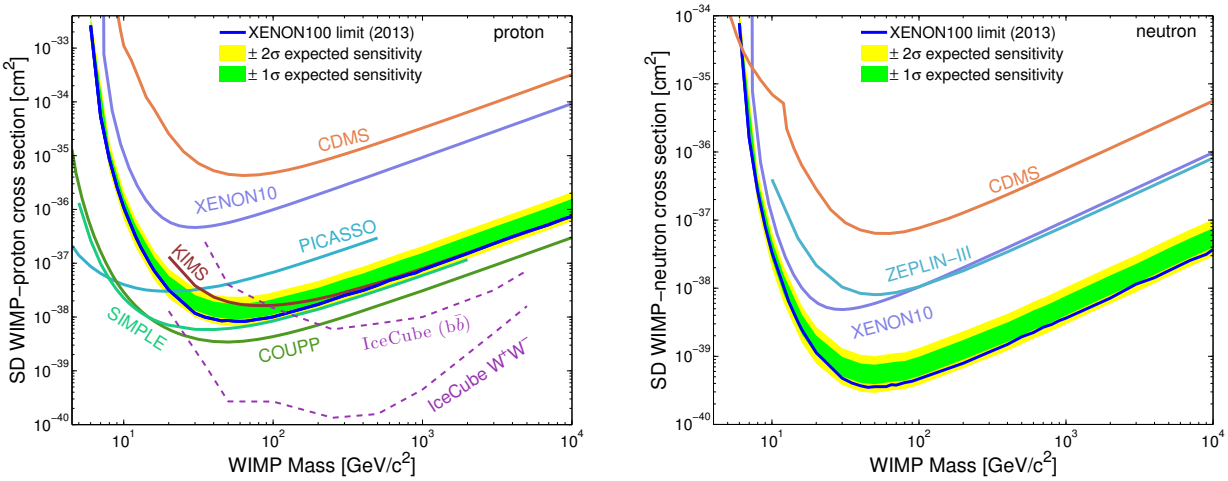

Figure 2.12: Bounds on the WIMP-nucleus cross-section for spin dependent interactions. The calculation is performed individually for protons (left) and neutrons (right) [15].

dependent bounds are computed individually for protons (left) and neutrons (right). It can be seen that XENON100 can not bound spin dependent interactions on protons

competitively, however for neutrons, it shows the best sensitivity. More details can be found in [15]. Also more exotic WIMP candidates such as inelastic dark matter has been probed by XENON100 [67].

As mentioned in the introduction, axions or ALPs are dark matter candidates which produce electronic recoil and can be tested with LXe detectors. The bounds set by XENON100 are shown in figure 1.2 and more details can be found in [19].

A third science run was performed during 2013 and 2014 where the author of this thesis participated in the detector operation (scheduled shifter) and in the off-line data analysis. The goal of the science run III, was to collect additional data with a reduced background, to perform a background stability analysis. This enables to probe another signal channel due to the expected annual modulation of dark matter interactions (see section 1.4).

Chapter 3

Detector characterisation for science run III

This chapter is devoted to the analysis of data, taken during the dark matter search from 22.04.2014 until the 08.01.2014 and in the following it will be named science run III. The relevant energy interval for the dark matter search was blinded in order to avoid a bias in the analysis. Various spatial corrections, definitions of the event selection criteria and calculations of the acceptances have to be performed before the WIMP sensitive region can be unblinded. In particular, this chapter shows the performance of the detector during science run III in terms of the energy resolution, light and charge yields as well as the derivation of the size correction of the charge signal.

3.1 Energy resolution, light and charge yields

For any kind of calorimeter, it is essential to determine the correlation between measured and true deposited energies. For a liquid xenon dual phase detector (e.g. XENON100) this relation can be calculated independently for the primary (S1) and secondary (S2) scintillation signals. In addition, a quantification of energy resolution is important, as it enables statements on the uncertainties of the estimated energy depositions. This section introduces the analysis of these quantities during science run III and are compared to science run II [65]. Note that in this section only interactions due to electronic recoils are considered and energy units written in keV refer to the unit $\mathrm{keV_{ee}}$.

Energy resolution The energy resolution can be generally expressed by $res(E)\ [\%] = 100 \cdot \frac{\sigma}{\mu}$, where σ and μ are the estimators for the mean and width of a Gaussian distribution. After application of various basic event selection criteria to prevent a contamination of noisy or double scattered events (see section 2.4.1), calibration measurements with radioactive sources with monoenergetic de-excitations, such as a AmBe neutron source and ^{137}Cs, can be used to determine the energy resolution (see figure 2.7 and section 2.4.3).

Since the light and charge signal are anti-correlated for electronic recoil in a LXe TPC (see section 2.2.1), the determination of the energy resolution is optimized by considering the relation of S1 and S2 in the event selection. This is achieved by an elliptical parameterization of two superimposed Gaussian distributions, representing the individual fluctuations in S1 and S2. Figure 3.1 shows as an example for such an ellipse in

the S1-S2 plane at 40 keV, however, this selection is applied to all relevant (40, 80, 164, 236, 662) keV calibration lines (see section 2.4.3). In addition, a parameter for the anti-

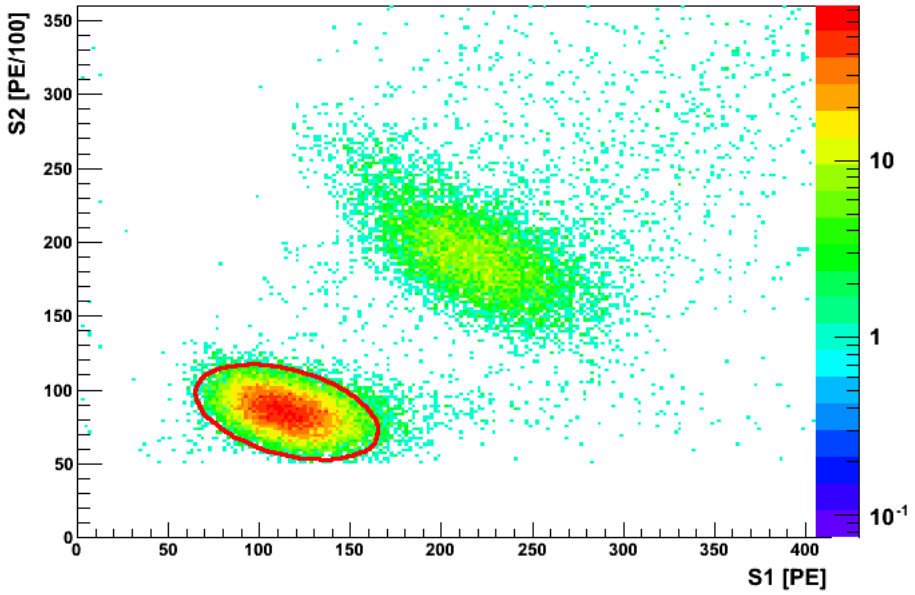

Figure 3.1: Elliptical peak selection of a 40 keV energy deposition in LXe in the parameter space of S1 and S2. The event selection includes $3\,\sigma$ of the two dimensional Gaussian distribution (red line). The color coded scale indicates the number of events in each bin of the two dimensional histogram.

correlation can be determined by the inclination of the ellipse with respect to the x-axis. The resulting combined energy scale (CES) improves the energy measurement, as the fluctuation of electron-ion pair recombinations is reduced for the combined signal compared to fluctuations of the individual signals.

After the event selection, an individual Gaussian fit to the S1 and S2 signals as well as in terms of the combined energy scale is performed to estimate the mean and width of the distributions. The results of the energy resolution during science III for S1, S2 and CES can be seen in figure 3.2 as blue markers at the top left, top right and bottom left, respectively. For comparison the energy resolution during science run I and II [47] are indicated by red and green markers. All values are comparable within the uncertainties and indicate a stable detector performance between science run I and III. Note that the shown uncertainties might be larger due to underestimated systematic errors in the event selection. The meta stable ^{129m}Xe is the sum of two transitions (see section 2.4.3), resulting in a varying energy resolution to a corresponding monoenergetic 236 keV deposition due to the energy dependence of the light and charge yield. Also the energy resolution is biased at 164 keV due to its vicinity to the ^{19}F line at 197 keV. As expected, the highest energy resolution is achieved in the combined energy scale.

Light and charge yields The light and charge yields describe for a given energy deposition the correlation to the detectors' response to the scintillation signal (S1) and charge signal (S2) (see section 2.5). The yield is given by the mean S1 and S2 peak

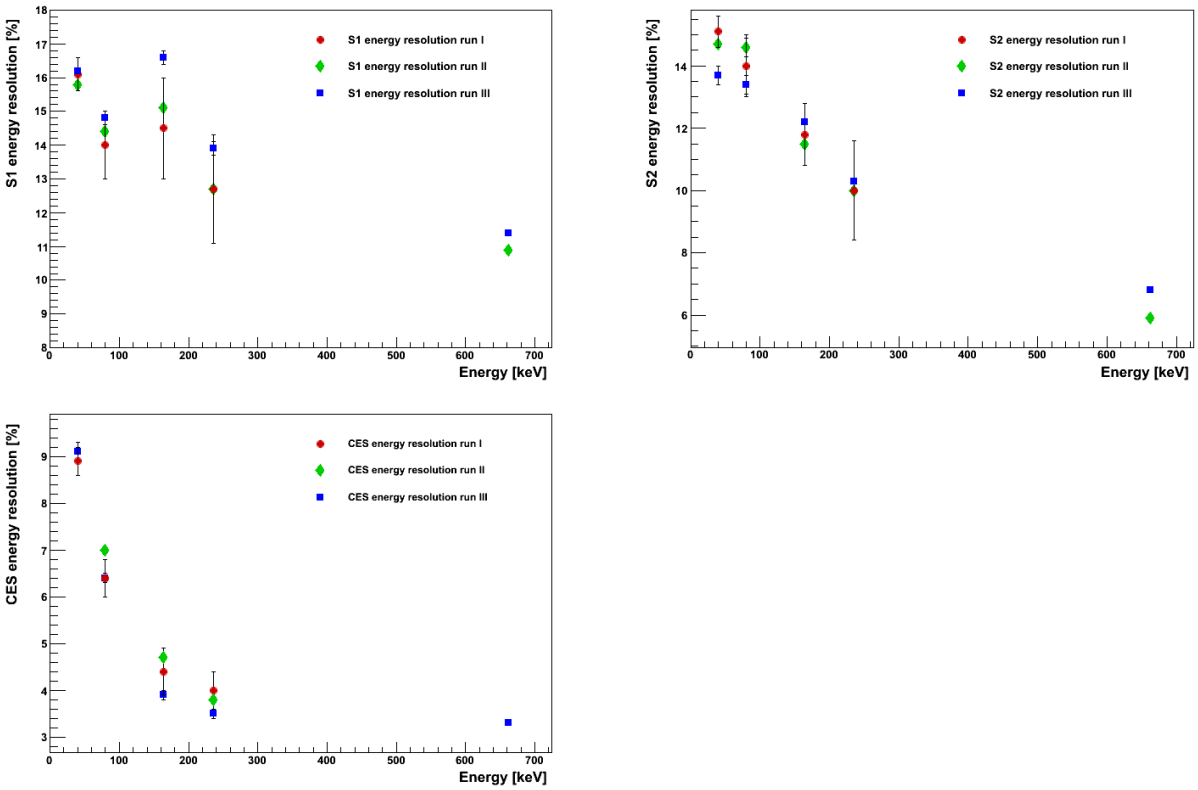

Figure 3.2: Comparison of the energy resolution at (40, 80, 164, 236, 662) keV in terms of S1 (top left), S2 (top right) and CES (bottom left) in science run I, II and III. The data for science run I and II are taken from [47]. It can be seen that energy resolutions in terms of S1, S2 and CES have not changed between science run I and III which indicates a stable detector performance.

size for a monoenergetic calibration line divided by the deposited energy. The analysis is performed at the same energies and event selection as described above for the energy resolution. The light (left) and charge (right) yields of science run II and III are displayed in figure 3.3.

The light yield is generally dependent on the interaction position due to a reduction of the solid angle at the borders of the TPC. The light collection of the PMTs is affected by the finite reflectivity inside the TPC, the Rayleigh scattering length in LXe and the limited transmission of the meshes [47]. A three dimensional correction map for the S1 size accounts for all these effects. Therefore, a change of the light yield over time would not only indicate problems of the TPC but also shows possible improvements due to e.g. different applied drift fields. The change of the average light yield between run II and III is estimated to be $(-0.9 \pm 0.5)\%$ and within $2\,\sigma$ comparable to 0. This can be expected since the detector set up is unchanged and the purity level of the LXe is similar between the two runs. Therefore, the for run II calculated light yield at 122 keV remains at $L_y = (2.28 \pm 0.04)$ PE/keV for science run III (see section 2.6).

In the right plot of figure 3.3 the charge yield for science run II and III is shown. In comparison to the proceeding science run II a significant decrease of the charge yield can be seen and is calculated to a value of $(-5.3 \pm 0.6)\,\%$. This can be understood by equation

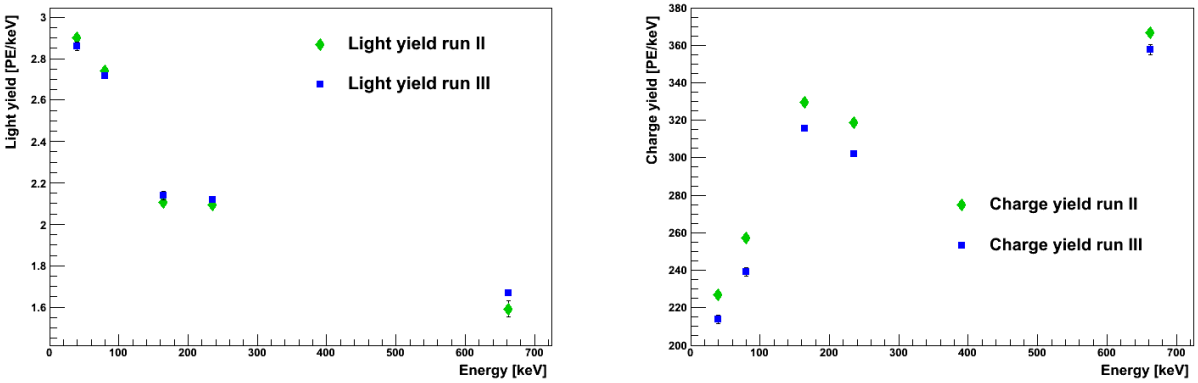

Figure 3.3: Light (left) and charge (right) yields in science run II and III are displayed by green and blue markers, respectively. The average light yield deviates by around $(-0.9 \pm 0.5)\%$ and is within $2\,\sigma$ comparable to 0. The light yield, however, decreased by $(-5.3 \pm 0.6)\,\%$ due to an increased liquid level in science run III.

2.15 as it shows that the S2 size is given by the S2 amplification which is a function of the size of the gas gap. In science run III a higher liquid level has been measured, and, hence, the gas gap is reduced, resulting in a weaker S2 amplification. This decrease has been confirmed by an independent analysis of the single electron gain as performed in [63].

3.2 Charge signal corrections

In section 2.3.2 the mechanisms of the S1 and S2 signal generation in a LXe dual phase TPC is introduced. Corrections on the size of the charge signal are generally dependent on parameters which determine the extraction yield of the electrons, the S2 amplification due to proportional scintillation and the PMT detection probability of a photon created at a position (x,y). In this section it will be shown that the S2 correction maps need to be modified for science run III. Furthermore, a method is introduced which improves the estimations of the spatial S2 size variations, resulting in a increase of the energy resolution of the detector.

3.2.1 Position dependence of the charge signal

For each measured S2 signal, the XENON100 data processor calculates the position relative to the S1 peak, the width and the height of the measured pulse among others [47]. The S2 size is determined by the sum of each measured PMT signal over the threshold of 0.3 PE [47] and is converted to a unit corresponding to photo electrons. This is done independently for the top and bottom PMT arrays and, hence, it is necessary to quantify the size corrections for each PMT array, separately. Since the proportional scintillation light is produced only at the top of the TPC, a different spatial dependency of the size variations in the top and bottom PMTs can be expected as it is shown in figure 3.5. The color coded pattern symbolizes the change of the S2 size with respect to the mean S2 size in the full TPC. As S2 scintillation light is measured by the bottom PMTs

travelled through the whole TPC, small variations in the S2 peak sizes are smeared out and the pattern becomes more homogeneous (left plot). The top map pattern (right plot), however, is dominated by switched off PMTs at around (-50,90) and (100,120), leading to a locally reduced S2 detection efficiency. Also a reduction of the light collection efficiency close to the PTFE walls of the TPC affects the S2 size, as the charge extraction yield is reduced by the decreasing solid angle covered by the PMTs in vicinity of the walls. In addition, inhomogeneities in the extraction field strength can be created due to small variations of the mechanical stress on the anode grid. These small fluctuations in the field strength yield to varying S2 amplifications. Note that the S2 size is in addition to its XY dependency also corrected for the signal reduction due to the finite electron lifetime quantified by the Z coordinate of the interaction vertex (see section 2.3.2). In the following sections the electron lifetime correction is always applied on the measured S2 size, so that the XY correction factors are not correlated with the Z coordinate.

3.2.2 Dataset and event selection

The correct estimation of the spatial S2 size corrections are strongly dependent on the choice of the dataset as well as the event selection. In this section the necessary conditions on the dataset and the important event selection criteria are introduced.

Dataset Generally, spatial S2 size variations can be estimated using any calibration source as long as PMTs do not saturate. The energy deposition needs to be monoenergetic to provide a constant charge yield and the statistics should be sufficient to determine the mean S2 size in a reasonably sized XY grid. During science run III, the only suitable calibration source for quantifying the spatial S2 variations is the AmBe neutron source (see section 2.4.3). The conditions are met either by the 40keV photons emitted by inelastic neutron scattering on ^{129}Xe or the 164 keV photons from the de-excitation of the metastable ^{131m}Xe. The ^{131m}Xe has a life time of 11.8 d (see table 2.1), long enough to be distributed in the TPC, resulting in a homogeneous event pattern in XY. In contrast, events due to the full absorption of the 40 keV photons are correlated to the AmBe source position, indicated by the red dot in figure 2.6. The inelastic neutron scattering is more likely to happen close to the source position due to the finite penetration depth of neutrons in LXe. In addition, the produced excited states have a half life below 1 ns, too short for the ^{129}Xe atom to be distributed homogeneously in the TPC. Therefore, the event pattern will be sensitive to the source position.

However, the 164 keV photons are measured by a lower extraction field as the anode voltage is reduced from 4.4 kV to 2.2 kV. This is necessary, because the top PMTs arrays start to saturate at energies above 100 keV, if measured with an 100 % extraction yield. It is to mention that the AmBe source produces also a 80 keV line created by inelastic neutron scattering off ^{131}Xe but the statistics is less than a factor of 3 and suffers from a background due to the vicinity of the 110 keV energy line of ^{19}F arising from neutron scattering with the Teflon reflector. In section 3.2.4 it will be shown that datasets taken at reduced anode voltage can not be used to correct spatial variations at normal extraction field strengths. Hence, the best option is, considering the mentioned boundary conditions, the 40 keV prompt signal of inelastic neutron scatters and accepting the inhomogeneous event distribution in the TPC as well as the reduced statistics.

Event selection For an unbiased derivation of the correction parameters it is necessary to apply various event quality conditions (see section 2.4.1). Events which are uncorrelated to the inelastic 40 keV energy line could bias the correction parameters, due to varying charge yields. Therefore, various conditions for physical events are applied in order to avoid noise events seen by single PMTs or show an unusual pulse form which passed the peak finding algorithm and is interpreted as a proper event. Also it is necessary to require single scatter events, so that the 40 keV photons deposit the energy in one vertex. In addition to these basic quality conditions, events with a 40 keV energy deposition are selected in the S1, S2 parameter space by selecting an elliptical region containing $2\,\sigma$ of the total events, which is shown in figure 3.1.

After selecting the events, the cylindrical TPC is divided in a rectangular grid in XY of (20×20) mm and displayed in the left of figure 3.4. The size of the grid is dependent on the available statistics and should be chosen as small as possible to achieve a high spatial resolution by considering a sufficient number of events in each grid cell. The right map in figure 3.4 illustrates the distribution of the number of events per cell for the 40 keV energy line. The inhomogeneous distribution can be explained by the AmBe neutron source position indicated by the red dot in figure 2.6.

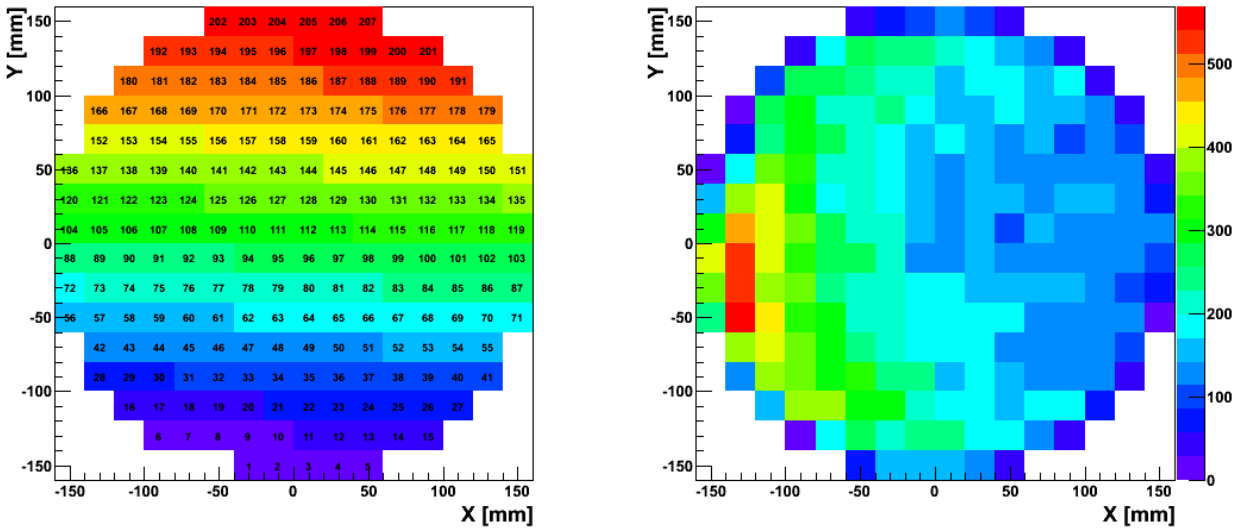

Figure 3.4: Applied grid size of (20×20) mm in the XY plane of the TPC (left). A cell represents an area where the mean S2 size is individually determined. The right plot displays the number of events per grid cell at 40 keV, indicated by the color coded scale. The inhomogeneous event distribution is caused by the AmBe neutron source position.

3.2.3 S2 size variation in science III

In science run II the S2 size correction maps were derived from events of 164 keV photons, emitted by the de-excitation of the meta-stable $^{131\mathrm{m}}$Xe isotope. Since the top PMTs would saturate under normal conditions of the extraction field strength the anode voltage is reduced. After two weeks of continuous measurements the large number of events allows a high spatial resolution of the S2 size variations, enabling a (11×11) mm grid size. This

can be seen in figure 3.5 for the bottom (left) and top (right) PMT arrays in science run III. With these maps the correction factors (color coded scale) are calculated by the

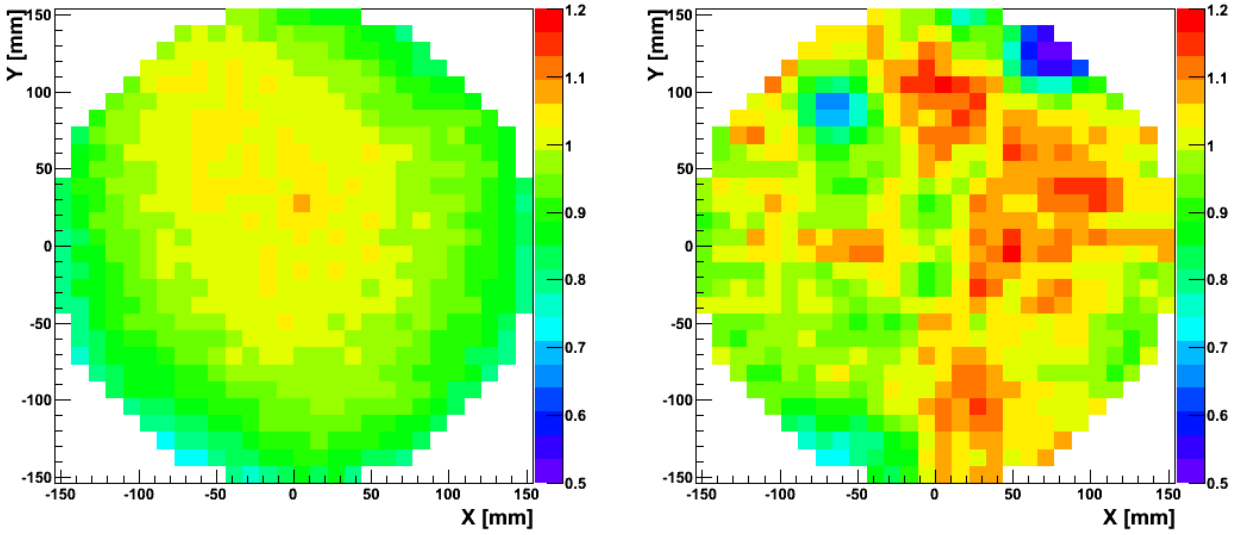

Figure 3.5: S2 correction map for the bottom (left) and top (right) PMT arrays derived at 164 keV, measured with an reduced extraction field. The grid size is (11×11) mm in each cell.

mean S2 size in each grid cell normalized by the average S2 size in the full TPC. Due to the approximation of the cylindrical shape of the TPC by a rectangular grid, cells at the edges and at the opposite of the AmBe source position might suffer from a lack of statistics. Gaussian fits would not converge and it is more robust to use the statistical mean of the histogram as the estimator of the S2 size. Under the assumption that the S2 size fluctuations relative to the mean value do not change, the correction factors can be estimated at this energy. These S2 correction maps look qualitatively similar to values published in [47] and the need of a new estimation of the size variation should be confirmed.

As it is shown in section 3.1, the liquid level raised between science run II and III, resulting in a reduction of the gas gap size and yielding to a smaller amplification of the charge signal. However, it is not obvious that an absolute change of the charge amplification leads to a change in the relative S2 size fluctuations. A first indication can be seen in figure 3.6 which shows the relative changes of the S2 sizes in run III, by using the correction maps for the S2 size as quantified during science run II. These maps are derived from the 164 keV energy line measured at reduced anode voltage during science run III. The color in each grid cell denotes the deviations from the overall mean S2 value. The red pattern in both top and bottom PMT arrays, indicates a more than 10 % increase of the S2 size with respect to the overall mean (black circle). For the following line of argumentation, to this pattern will be referred as population A. In [65] the maximal corrections on the S2 size are stated to be around 15 % and, since the S2 size deviations of the already corrected signals in science run III are in the order of 10 %, new estimations of the S2 size corrections can improve the datasets.

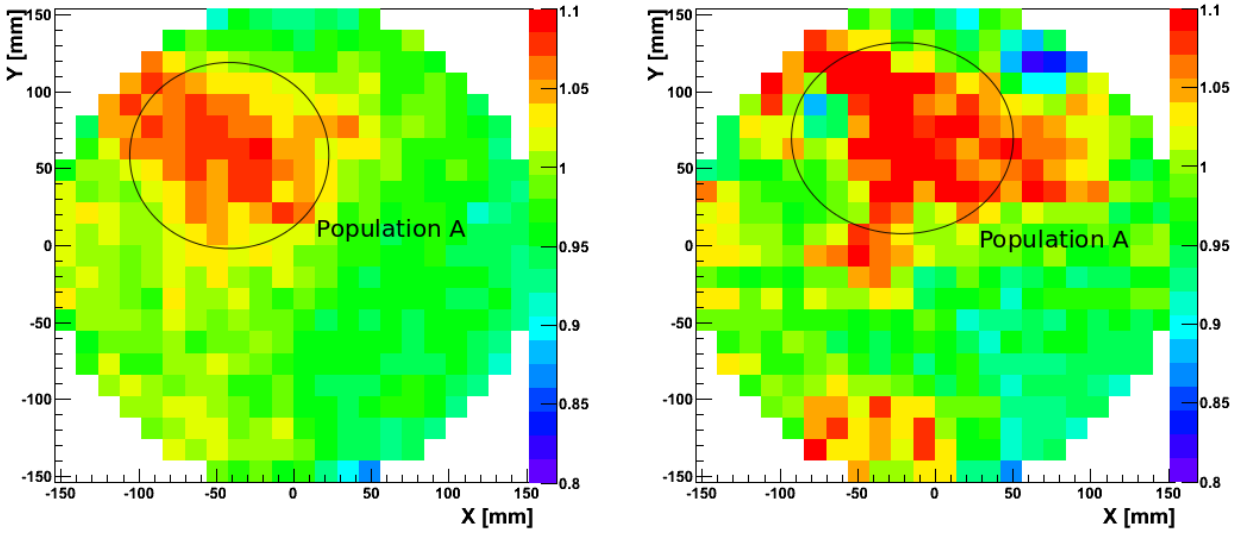

Figure 3.6: S2 variations in the bottom (left) and top (right) PMT arrays derived at 164 keV at an applied anode voltage of 2.2 kV.

3.2.4 Dependence of the S2 correction on the extraction field

The method to estimate the S2 size variations at reduced anode voltage is based on the assumption that the relative size differences are independent on the extraction field strength. In order to test this hypothesis, figure 3.7 shows the corrected S2 sizes for the bottom (left) and top (right) PMT arrays at a factor of two higher extraction field strength for the 40 keV energy line. Note that a comparison of the 164 keV lines at both

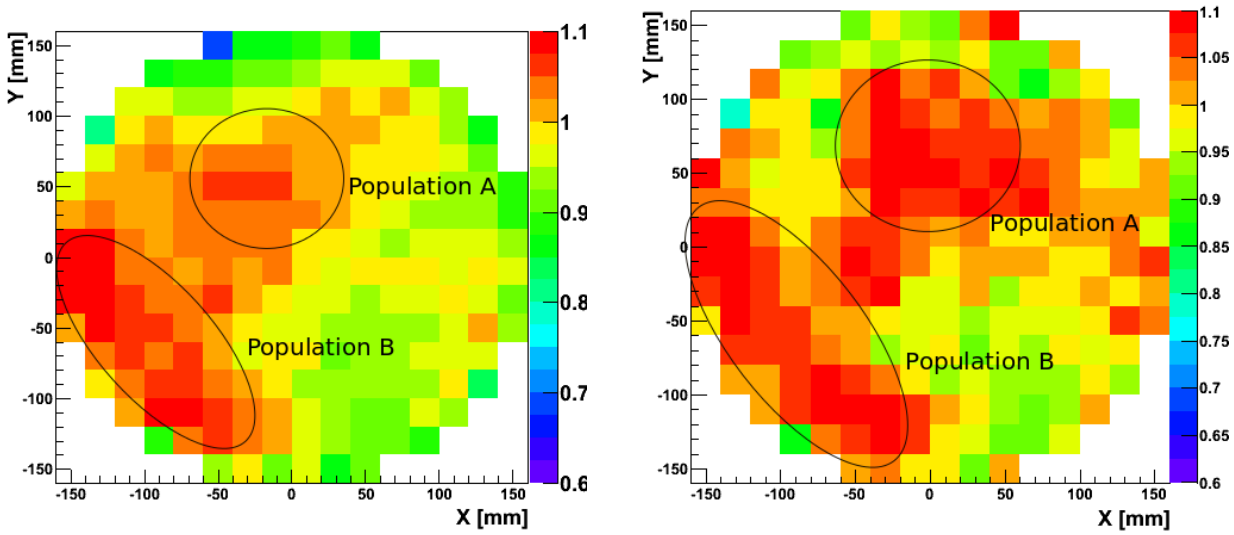

Figure 3.7: Corrected bottom (left) and top (right) S2 sizes at 40 keV, 4.4 kV anode voltage. S2 size fluctuations are estimated during science run II.

anode voltages is difficult, because the PMTs in the top array saturate. A population with larger S2 sizes at a similar spatial region as in figure 3.6 (population A) can be

seen. However, a second region arises at values of X and Y below 0 (population B). The difference of the relative S2 size variations for different anode voltages indicates that the fluctuations are not independent of extraction field strength. It can be shown that population A is correctly estimated by maps derived from datasets measured at reduced anode voltages but population B still remains after the correction. This leads to the conclusion that the S2 size variations have to be estimated by the corresponding extraction field strength.

In order to verify the different fluctuation pattern, figure 3.8 (left) shows the difference in percent for each grid cell at the same energy 164 keV but by a factor of two different extraction field strengths. Again for negative values of X and Y (population B) the

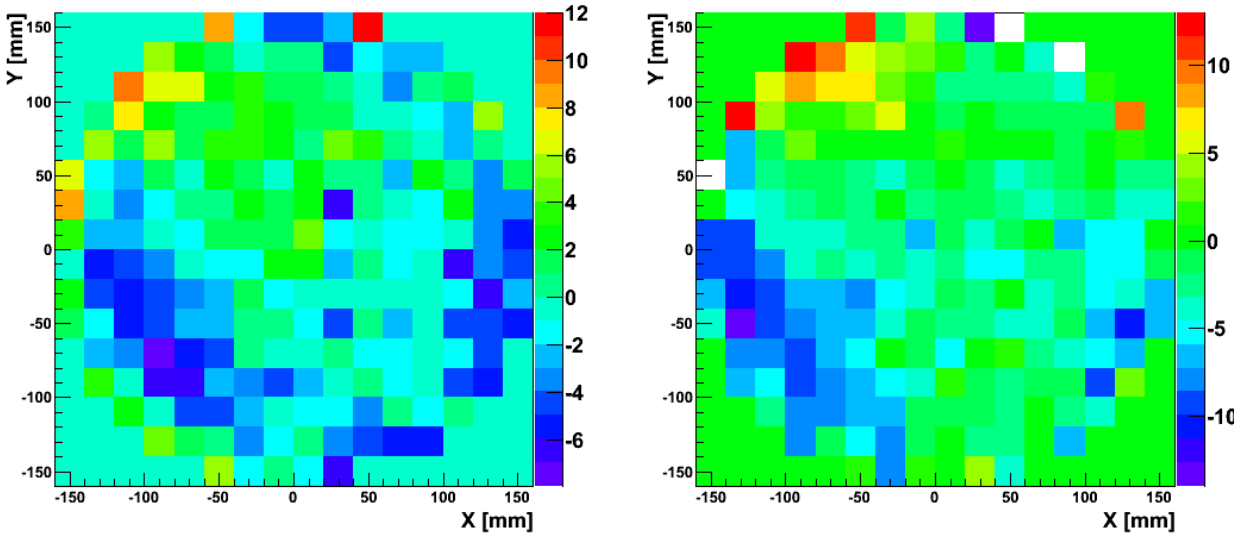

Figure 3.8: Deviations of S2 size fluctuations at 164 keV for different extraction field strengths (2.2 kV and 4.4 kV) measured with the bottom PMT arrays (left).The right plot compares S2 size fluctuations of the 164 keV (2.2 kV anode voltage) to 40 keV (4.4 kV anode voltage) of the top PMT arrays (right). The 40 keV line is chosen to avoid saturation effects of the PMTs.

absolute difference between the fluctuation patterns reach values up to 7%, whereas at the spatial position of population A deviations of only 2 % can be seen. Figure 3.8 (right) displays the difference of the fluctuations of the 164 keV at 2.2 kV to the 40 keV map measured at 4.4 kV, to avoid a bias due to saturating PMTs. As expected, the same pattern can be seen.

A possible explanation A possible explanation for the dependence of the S2 size variations on the extraction field strength is given below. In chapter 2, equation 2.15 is introduced to describe the corrections on the charge signal. It is shown that the S2 size measured by the PMT i at a position r is dependent on the yield κ which describes the probability that electrons pass the liquid gas interface and is mainly influenced by the field strength above the liquid surface. Figure 3.9 shows the extraction yield as a function of the field strength in the gas gap, measured with single electron events [63]. It can be seen that the yield is 100 % for fields above 8.5 kV/cm. The data shows, however,

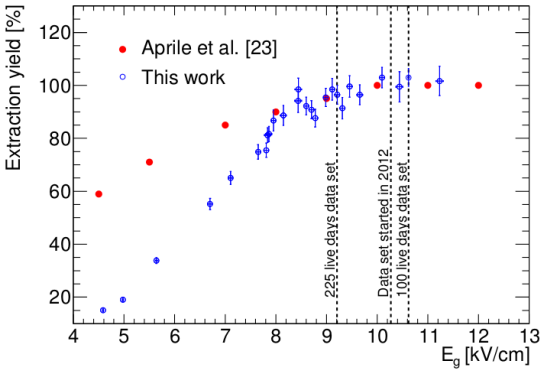

Figure 3.9: The figure shows the liquid-gas extraction yield for electrons as a function of the electric field above the liquid (figure from [63]).

a slope below 8.5 kV/cm and thus local variations of the field strengths result in different extraction yields.

If one considers the gate and anode grid as a simple plate capacitor, then the field within the plates is given by $E = \frac{U}{d}$. With a constant potential U but changing distance d, the field between the plates will vary. For XENON100, the maximal mesh warping is estimated to be around $\Delta d_g = (0.16 \pm 0.03)$ mm [72]. The value is derived from a map of the S2 width defined at 10 % of the maximal peak height as shown in figure 3.10. As the

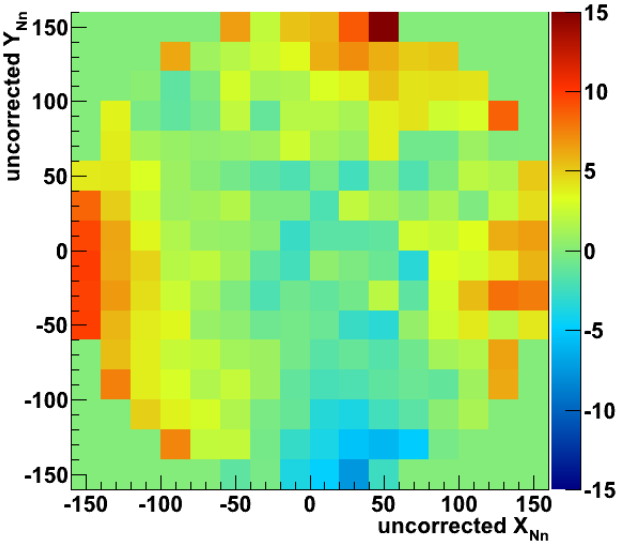

Figure 3.10: Relative differences of the S2 width parameter in the XY plane (figure from [72]).

width is directly linked to the time of flight of the electrons through the gas gap, the S2 width is in general more sensitive to small variations of the gas gap length. Thus, figure 3.10 shows three patterns at the top, left and right with a large width, correlating with the mounting structure of the mesh which is fixed at these positions. The field strength

in the gas gap can be approximated by [72],

$$E_g = \frac{2U}{d + d_g} \tag{3.1}$$

and accordingly a variation of the gas gap ϵ due to mesh warping is given by:

$$\Delta E_g = E_g - E_{g+\epsilon} = \frac{2U}{d + d_g} - \frac{2U}{(d + \epsilon) + (d_g + \epsilon)}. \tag{3.2}$$

Inserting values for science run III at reduced anode voltage U = 2.2 kV, d = 5 mm and d_g = 0.26 mm, an estimation of the field strengths variations lead to 0.23 kV/cm. The local variation translates to a maximal change of the extraction yield up to (5±1) %. This can be derived by using the values of figure 3.9 (blue markers), evaluated at field strengths of around 5.8 kV/cm, which corresponds to an 2.2 kV anode voltage. Note that data indicated by the red markers deviate at small extraction field, probably due to a different geometry of the used detector [63]. The relative change of the extraction yield is (15±3) % and is comparable to the maximal differences in figure 3.8 of about 12 %. Variations in the gas gap length do not affect the S2 signal size at 4.4 kV, since the extraction yield is constant for the corresponding extraction field strengths. In conclusion, correction maps derived at a non constant extraction yield can not be used to correct the S2 size pattern at field strengths above 9 kV due to inhomogeneities in the extraction field.

3.2.5 Deriving a new S2 correction map

In the previous sections it has been shown that due to variations in the extraction field strength, S2 maps indicate a different spatial size pattern. Hence, it is required that spatial S2 size variations are estimated by datasets measured at extraction field strengths above 9 kV/cm and PMTs should not saturate. Then the only available dataset is the 40 keV AmBe energy line. Due to the limited statistics in grid cells at the opposite of the source position, the grid size needs to be enlarged from (11×11) mm to (20×20) mm, in order to maintain negligible statistical errors for the estimation of the mean S2 size. The resulting estimations of the relative corrections are shown in figure 3.11 for the bottom (left) and top (right) PMT arrays. A coarser grid can not improve the estimation of spatial differences in the S2 size, however, the systematic bias created by population B is avoided.

Testing the quality of the correction map The quality of the corrected S2 sizes can be estimated by evaluating the energy resolution of the S2 signal or in terms of the combined energy scale (see section 3.1). To quantify the improvement of the newly derived correction map, figure 3.12 compares the count rates at various energies of remaining radioactive elements in the TPC [73]. The S2 sizes are corrected with maps derived in science run II (purple line) and the map derived in this work (blue lines) for difference fiducial volumes. The strongest evidence for an improvement can be seen at high energies by the measured decays of ^{60}Co at 1332 keV and 1332 keV as well as by ^{40}K at 1460 keV [61]. The new corrections (blue lines) increase the energy resolution to resolve the peaks at 1332 keV and 1460 keV.

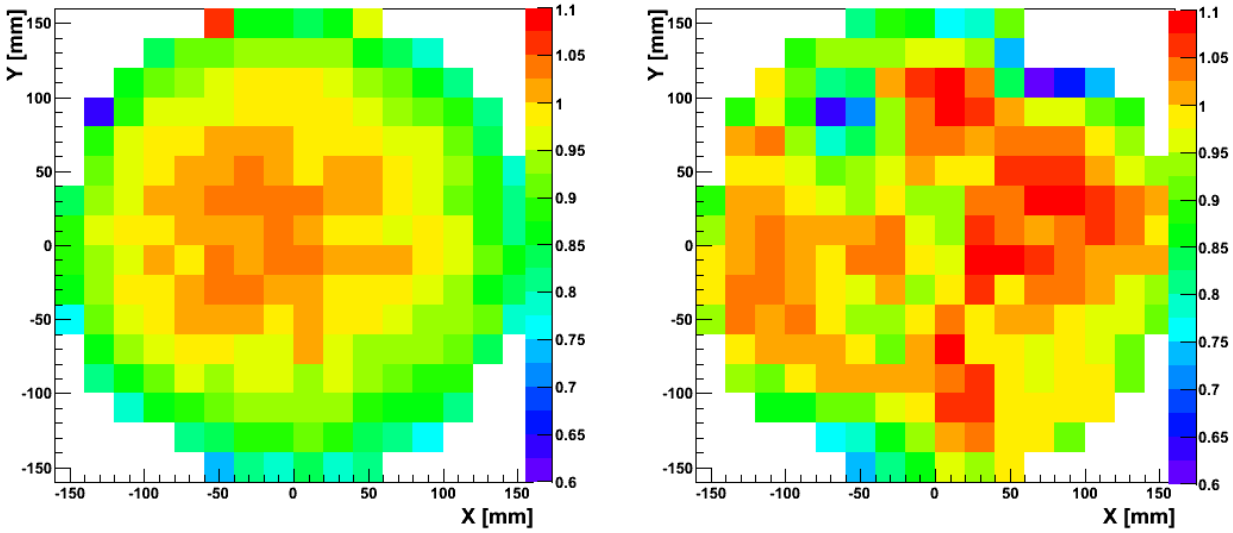

Figure 3.11: S2 correction map for the bottom (left) and top (right) PMT arrays derived at 40 keV during science run III.

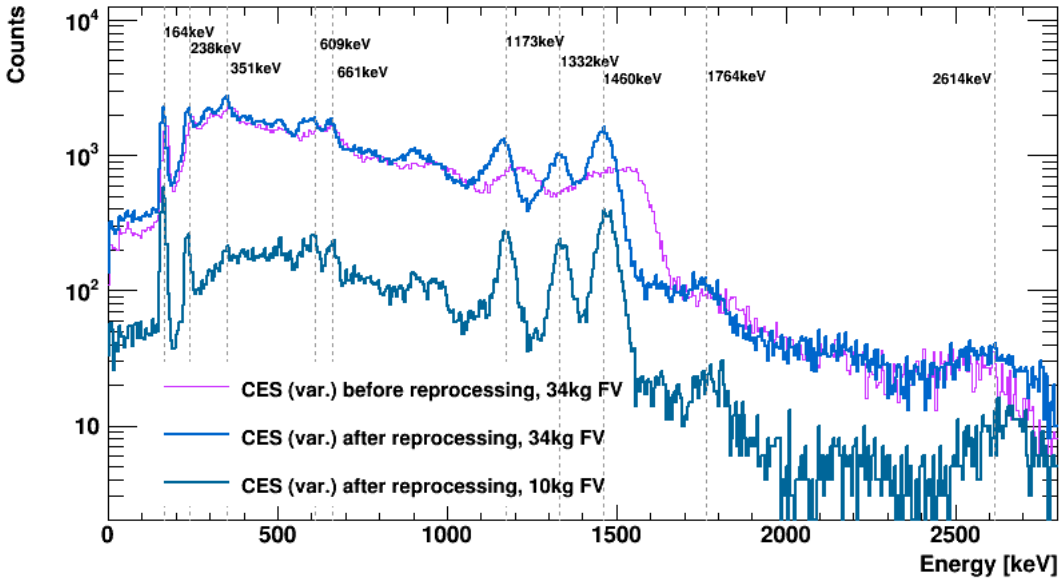

Figure 3.12: Comparison of the count rates in terms of the combined energy scale of the background spectrum. It can be seen that the new correction maps increase the energy resolution, especially at higher energies (figure taken from [74]).

3.3 Discussion

In this chapter the energy resolution, charge and light yield are estimated to characterize the performance of the XENON100 detector during science run III. The results indicate that the performance of the detector is comparable to science run I and II within the uncertainties and thus stable for over three years. Only the S2 amplification is reduced by (5.3± 0.6) % due to an increased liquid level. Hence, this can be avoided by increasing

the gas gap during the filling procedure in future dark matter science runs.

An improved method to correct for spatial differences in the S2 size is introduced. We show that correction maps can not be derived from datasets where the extraction yield is not constant. The reason is given by a mesh warping which induces inhomogeneities in the extraction field in well defined areas inside the TPC. Varying extraction yields induce a bias in the S2 size pattern, resulting in an artificially reduced energy resolution. This can be avoided if only datasets are considered for the estimation of the S2 size differences where the anode voltage is large enough to guarantee a constant extraction yield. It is to mention that the requirements of a monoenergetic energy line, sufficient statistics and a constant extraction yield is only fulfilled for the 40 keV line. Since this energy line is produced due to the inelastic scattering, the event distribution is correlated to the source position, resulting in an inhomogeneous pattern in the correction gird. Also the overall number of events is rather small, forcing a coarse grid and a reduced spatial resolution. Therefore, this method could be further improved with a ^{83m}Kr calibration [75], which not only could lead to large statistics but also to a homogeneous event distribution in the TPC.

Chapter 4

Charge yield of electromagnetic interactions in LXe

For any direct detection experiment it is essential to measure precisely the relation between the signal yield and the corresponding energy deposition in the detector. As mentioned in section 2.5 for WIMP searches the quenching of the charge and light signals for nuclear recoils in XENON100 is expressed by Q_y and $\mathcal{L}_{\text{eff}}$, respectively. However, the XENON100 experiment is not only sensitive to dark matter particles scattering off a nucleus but can also probe new particles beyond the standard model which induce electronic recoils. At the time of writing, the most popular candidate for such interactions are axions or ALPs (see section 1.2). To understand the signatures of such particles in liquid xenon, it is necessary to study the energy dependence of the charge yield for these possible interactions. In this work an analysis, able to measure the charge yield with the XENON100 detector is introduced. This is achieved by selecting double scattered photons of a ^{137}Cs calibration source. For these events it is possible to reconstruct the Compton angle via a kinematic approach due to the high vertex resolution of the detector. In addition to the description of the method, first results are shown and compared to semi empirical predictions. It is to mention that, due to the absence of calibration sources below 40 keV in XENON100 (see section 2.4.3), the region from 0 to 40 keV is of major interest which corresponds to very small scattering angles of less than 20 degrees.

4.1 Introduction to the method

In this work a kinematic approach is introduced to reconstruct the Compton angle of double scattered photons and, hence, the energy deposition of double scattered photons as indicated in figure 4.1. The position of the calibration source is fixed at the outside of the cryostat (see section 2.4.3). An emitted gamma ray propagates a distance $|\vec{d1}|$ through the surrounding material of the TPC and can interact in vertex 1 (V1) via an Compton scatter process, generating a primary (S1) and secondary (S2) scintillation signal in the detector (see section 2.2). Following this, the Compton scattered photon will travel a distance $|\vec{d2}|$ until the photon is e.g. fully absorbed in a second interaction site (V2), producing the corresponding S1 and S2 signals. The angle between the vectors $\vec{d1}$ and $\vec{d2}$ is denoted by θ. The following analysis is based on this interaction scheme. A

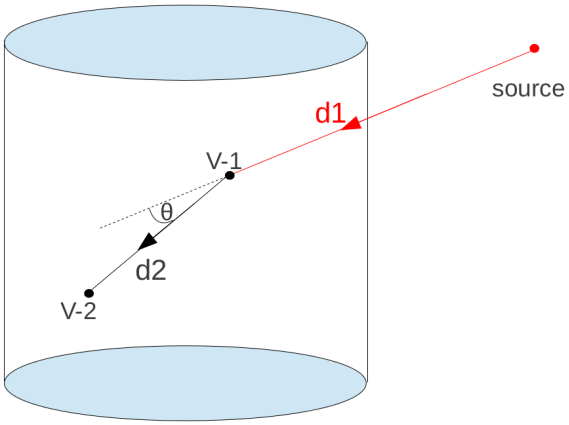

Figure 4.1: The sketch illustrates the kinematic approach to reconstruct the deposited energy of a double scattered photon inside the TPC (cylindrical shape). The two interactions of the photons with the Xe atoms are denoted by V1 and V2 and the Compton angle by θ. In addition it is useful to define the propagation length from the source to the first vertex as d1 and the distance between the vertices as d2.

typical PMT waveform of such an event can be seen figure 4.2. Note that the indicated S1 peak is a superposition of two S1 signals from V1 and V2 which can, due to the short separation time ($\sim$ ns) not be resolved. The S2 peaks, however, show the expected

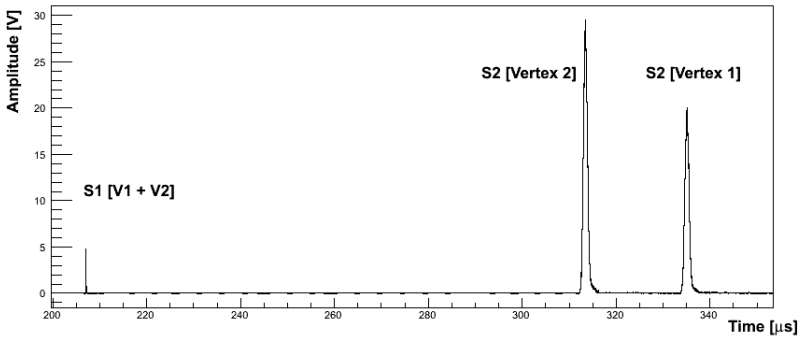

Figure 4.2: The figure shows a typical waveform of a double scatter events with two S2 peaks and an unresolved superposition of two S1 peaks. Due to the size ordering of the S2 peaks during the data processing, vertex 1 and 2 are interchanged.

double peak structure. The ordering of the S2 peaks correspond to the drift time and thus to the Z position (see chapter 2) of the interaction, but the chronological order of the interactions remain unknown. The peak finding algorithm labels the S2 peaks by their size, and, thus, only a kinematic selection of the events allows a reconstruction of the

chronological order. If a Compton scatter process takes place in vertex 1, the deposited energy E_{dep} can be computed with Compton formula

$$E_{dep} = E_\gamma - \frac{E_\gamma}{1 + \frac{E_\gamma}{m_e c^2}(1 - \cos(\theta))}, \tag{4.1}$$

where E_γ denotes the initial energy of the photon, θ the Compton angle and m_e the mass of the electron. Furthermore, the Compton angle is fully described by the measurement of the position of two the vertices V1, V2 and the knowledge of the source position by

$$\theta = 180^\circ - \text{acos}\left(\frac{\vec{d1} \cdot \vec{d2}}{|\vec{d1}||\vec{d2}|}\right). \tag{4.2}$$

The vectors $\vec{d1}$ and $\vec{d2}$ are defined in figure 4.1 and describe each track of the photon.

In conclusion, if we consider a monoenergetic gamma source in a well defined position and select events which interact twice and only twice inside the TPC, then the deposited energy in vertex 1 can be reconstructed without any assumptions on the secondary scintillation yield for electronic recoils.

4.2 Event selection

This section describes the criteria applied to the data in order to select double scattered photons as mentioned in section 4.1. In the past years, the XENON100 collaboration derived a number of selection criteria to avoid events which are not related to WIMP interactions [62]. These conditions are particularly designed for low energetic nuclear recoil events as well as a reduction of events which scattered more than once in the TPC. For this analysis, however, most of these basic quality criteria can not be used since the event selection is based on double scattered photons, the energy depositions are higher in comparison to expected WIMP interactions and scattering processes are based on electronic recoil. New selection criteria have to be studied and only basic quality criteria to avoid noisy events can be used from dark matter searches.

4.2.1 Full energy deposition for double scatter events

In this kinematic approach it is necessary to know the initial energy of the photon as well as the exact source position (see equations 4.1 and 4.2). Therefore only monoenergetic calibrations sources from a fixed point like position can be used. The following analysis considers data taken with the ^{137}Cs calibration source which emits 662 keV gamma rays (see section 2.4.3), since it is the only calibration source available in XENON100 which fulfills both conditions. Applying basic criteria to avoid noisy events and require two and only two S2 peaks above a threshold, it is possible to derive figure 4.3. The figure shows the sum of the S2 sizes in both vertices with respect to the S1 size and the color coded scale indicates the number of events in each bin. As mentioned before, only one S1 peak is expected, since the time difference of the two interactions is too small ($\sim$ns) to be resolved. The lower red line indicates the important requirement that the sum of the S2 size in both vertices sum up to 662 keV. In addition, this cut avoids events which not

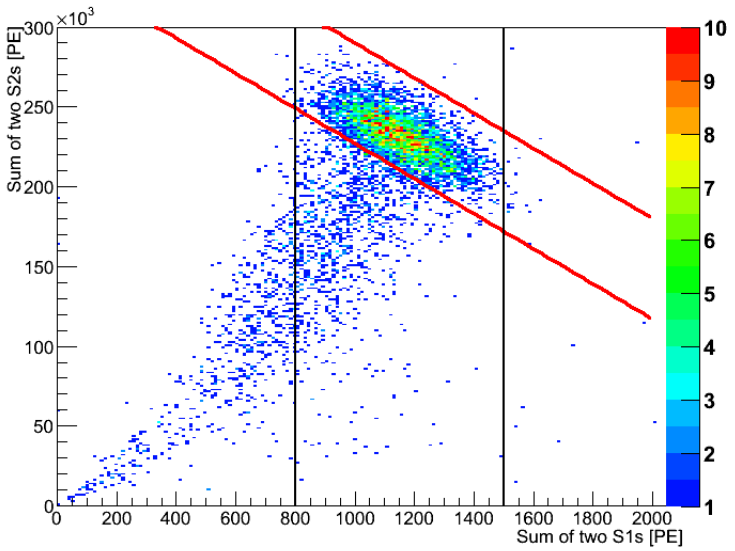

Figure 4.3: The figure shows events with two S2 peaks, where the sum of the two largest S2 peak sizes is plotted with respect to the superposition of two S1 peaks. The color coded pattern indicates the number of events in each bin. The red and blue lines denote the selection criteria for double scatter events in order to ensure a complete energy deposition of 662 keV inside the TPC.

only scatter twice in the TPC but also interacts once in the surrounding material which would bias the Compton angle estimation. The upper red line excludes events which are not directly associated with the ^{137}Cs source since the sum of the two vertices indicate a higher energy deposition than 662 keV. The black lines show the selection criteria on the largest S1 peak size. The definition should not be more restrictive since its a superposition of two S1 signals and the light yield for each energy deposition can differ significantly due to the non linearity of the light yield (see section 2.5).

4.2.2 Forward scattering selection

The determination of the charge yield in the energy region below 40 keV is not only interesting due to the absence of calibration sources at these low energies but restricting the event selection to small Compton angles, enables the possibility to apply a number of selection criteria based on the kinematics of forward scattered photons.

The left sketch of figure 4.4 shows the expected interaction pattern for forward scattering. Note that it is not possible to determine the first and second interaction via their chronological order, since the information about the absolute time stamp of each interaction is not accessible. However, this interaction pattern can be selected by the relative sizes of the S2 signals due to the restriction of forward scattered photons, which is the equivalent to a smaller energy deposition in V1 than in V2 (S2(V1) < S2(V2)). In addition, the information about the spatial positions of the interaction sites can be used to select forward scattered photons, as the length of the vector from the source position to vertex 1 has to be smaller than the length of the vector pointing from the source to vertex 2.

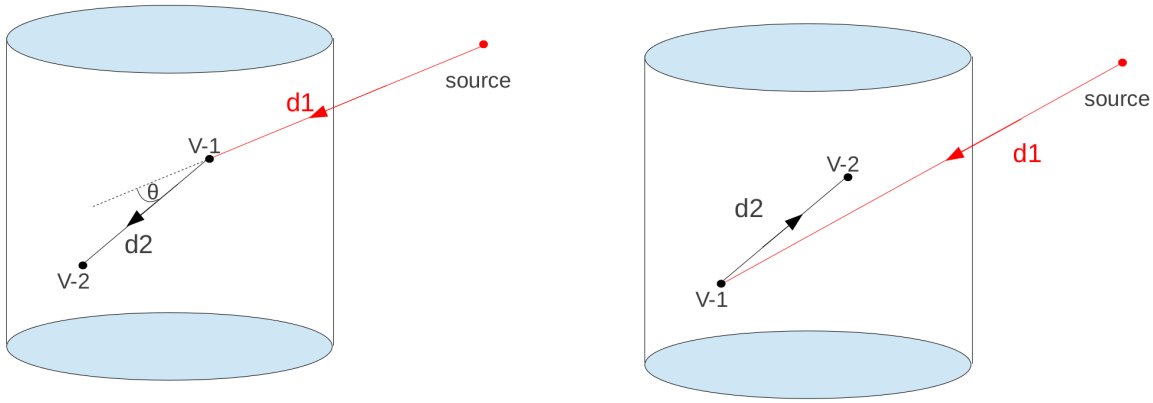

Figure 4.4: The figure is a sketch of the interaction pattern of a forward scattered photon (left). The right figure shows an event with a Compton angle larger than 90°. These two interaction patterns might show a similar waveform and kinematic structure but can be separated by a lower bound on the length of d2. For more details see text.

Note that, these criteria are not sufficiently since a back scatter event could show the same interaction pattern as indicated in figure 4.4 (right), where the Compton angle would be falsely reconstructed. An event which scatters backwards can in principle have the same relative S2 sizes and spatial vertex distribution and would pass the above defined criteria. Hence, a condition on the vertex which is closer to the source position has the smaller S2 size is not a unique definition for a forward scattered double scatter event. To discriminate both interaction patterns the mean free path of photons with different energies can be used. In case of a true forward scattered photon, the photon energy is larger in comparison to the back scattered one and thus the mean free path is enhanced. A lower bound of the propagation length of the Compton scattered photon selects mainly forward scattered photons.

To estimate the mean energy of the photon after the Compton scattering, the average energy of the scattered photon needs to be determined independently for forward and backward scatters. A calculation, using the cross section of Compton scattering results in 528 keV and 256 keV for forward and backward scattered photons, respectively. The mean free path (l) is then calculated by the attenuation coefficients shown in figure 4.5 [76] and the density for liquid xenon at 1 bar over pressure and -173 K ($\sim 2.9\,\frac{\mathrm{g}}{\mathrm{cm}^3}$ [77]). The resulting values for l are 3.5 cm and 1.9 cm for forward and backward scattering, respectively. Finally, the interaction probability of a photon with matter can be computed by the Beer-Lambert law

$$P_{int} = \frac{1}{l}\int_0^d e^{-\frac{x}{l}}\,\mathrm{dx}, \tag{4.3}$$

where l denotes again the mean free path of the photon and d the track length. The integrated probability for a second interaction with respect to the propagation length

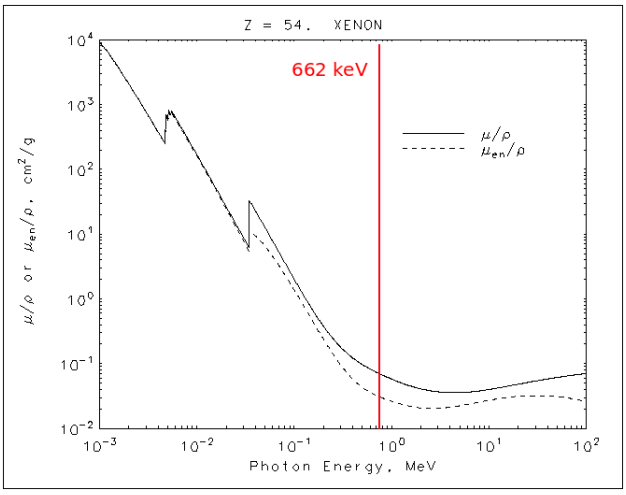

Figure 4.5: The figure shows the mass attenuation coefficients μ/ρ for photon interactions with xenon in the energy rage from a few keV to 100 MeV [76].

d of the photon is shown in figure 4.6. The blue line shows the forward scattered and

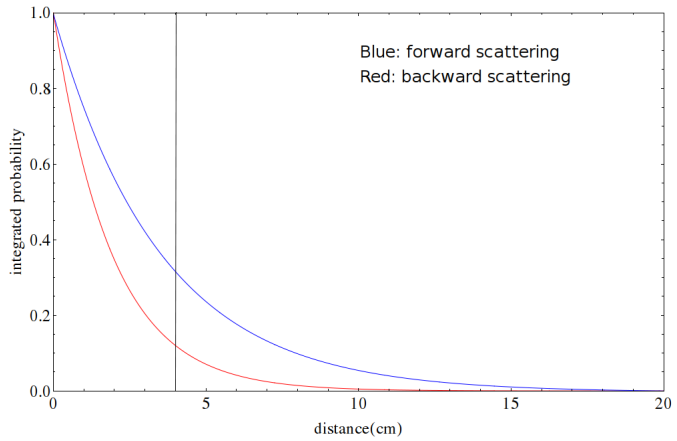

Figure 4.6: Integrated probabilities of a second interaction of photons which scattered in vertex 1 forward (blue line) and backward (red line). The black vertical line denotes the lower limit of the propagation length for Compton scattered photons such that only 10 % backscattered events are accepted.

the red line the backward scattered photons. Due to the smaller mean free path of the backward scattered photons, the probability for a second interaction decreases faster than for photons with a larger mean free path. The vertical black line visualizes the condition on the lower limit of the propagation length $|\vec{d2}|$ at 4 cm. This corresponds to a contamination of approximately 10 % of backscatter events in the forward scatter sample. Note that this is an upper limit, since a further condition will be introduced in section 4.2.4 which also reduces these events.

4.2.3 Restrictions on the charge pulse width

To further increase the quality of events it is necessary to avoid vertices, where two interactions are present, but could not be resolved by the position reconstruction algorithm due to the limited position resolution of 3 mm in the XY plane [47]. To illustrate these events which scattered three times inside the TPC but have been reconstructed as two vertices, figure 4.7 shows a sketch of the interaction pattern. These events could bias the

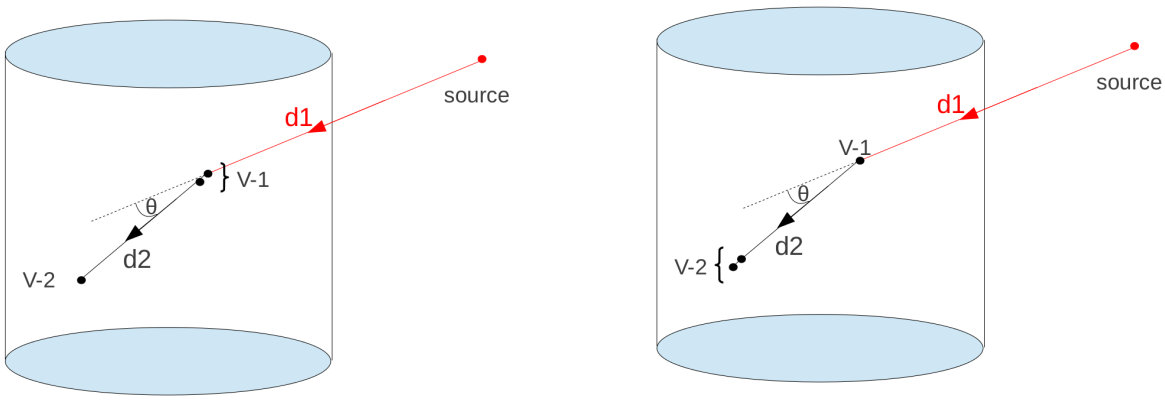

Figure 4.7: Illustration of events which scattered three times in the TPC but only two vertices are reconstructed with the position reconstruction algorithm due to the limited position resolution (3 mm). This could bias the estimation of the deposited energy in a double scatter vertex due to a differing charge yield of the two interactions.

estimation of the deposited energy due to a differing charge yield for each interaction. To reduce a contamination of these double scatter vertices in the analysis, a requirement on the width of the S2 peak can be used. The width of the S2 peak is derived at 10 % of the total amplitude and a typical waveform can be seen in the left waveform of figure 4.8. It shows a symmetric and uniform peak. The right waveform indicates a substructure, constituting of a superposition of two Gaussian distributions. Thus the right waveform of figure 4.8 can be explained by events which interacted twice within a distance smaller than the position resolution of the XENON100 detector. A rough estimation of the interaction probability within the vertex resolution can be done with equation 4.3. After a first Compton interaction the photon has an average energy of 398 keV corresponding to a mean free path of 3.3 cm. Thus about 9 % of the events should interact twice within the vertex resolution of the detector and represent a non negligible population of selected events. The same reasoning holds for vertex 2 but with a smaller average energy of the Compton scattered photon resulting in a smaller mean free path as well as a lower Compton scatter cross section. The energy depositions of two nearby interactions, can result in an increasing width of the waveform and therefore the condition of the peak width is a discrimination parameter to avoid clear double scatter vertices. Note that this condition can not avoid all double scatter vertices and further studies with a Monte Carlo

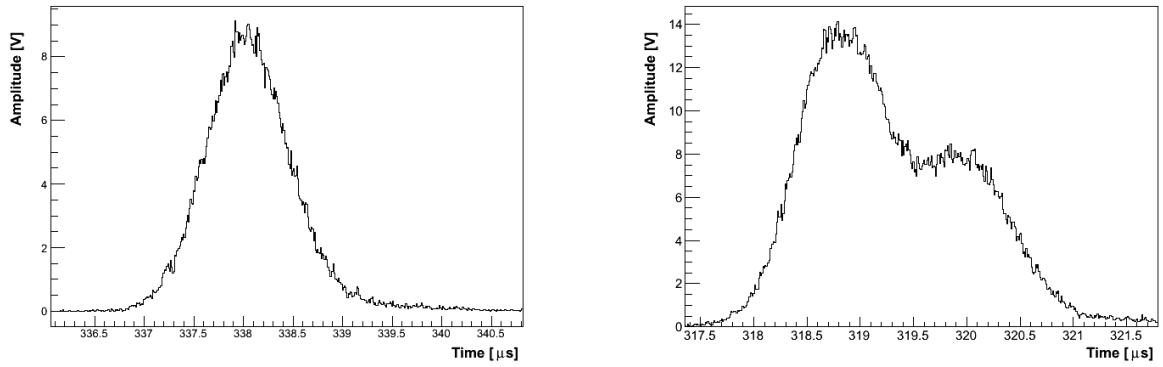

Figure 4.8: This figure compares waveform of single (left) and double scatter vertices (right). It can be seen that the peak width, defined at 10 % of the amplitude, increases for events which which scattered twice in a single reconstructed vertex.

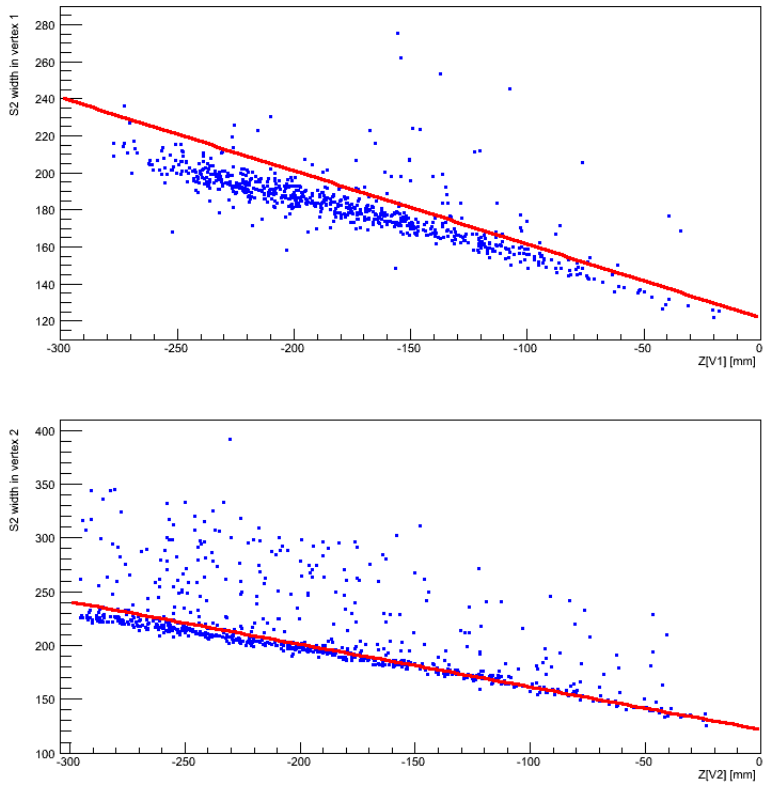

Figure 4.9: The figure shows the width of the S2 peak in units of tens of ns, measured at 10% of the amplitude, for double scatter events in vertex 1 (upper figure) and vertex 2 (lower figure) with respect to the Z position in the TPC. The red line indicates the upper bound on the S2 width derived from single scatter events with a 662 keV energy deposition. The restrictive bound on the S2 width tries to avoid as many double scatter vertices as possible, by considering the loss of statistics.

simulation have to show the efficiency of this discrimination parameter.

In the process of deriving an upper bound on the S2 peak width, measured at 10 % of

the amplitude, it is important to realize that the width is on one hand dependent on the drift length due to a diffusion of the electron cloud and on the other hand increasing with larger S2 sizes. In the following we neglect the energy dependence of the S2 width, since the dependency is small at high energies. The drift time dependence, however, can be estimated by single scatter events at 662 keV. Therefore, a 50 % quantile of the S2 width with respect to the drift time is calculated and a linear fit of the computed quantiles can be seen in figure 4.9 (red line). In addition, figure shows 4.9 the S2 width of double scatter events for vertex 1 (upper plot) and vertex 2 (lower plot) with respect to the Z position. The 50 % quantile is chosen in order increase the quality of events at the cost of reduction of double scatter events. All markers which lay above the red lines are excluded from the analysis due their large pulse width.

4.2.4 Energy balance requirement

By including the information about the S2 size in the second vertex a condition on the energy balance can be set. The knowledge of a full energy deposition of the 662 keV photon inside the TPC at two interaction sites allows to require for each double scatter event the energy condition

$$E_\gamma - E_{V1} - E_{V2} = 0. \tag{4.4}$$

Since we know $E_\gamma = 662\,\text{keV}$ and E_{V1} is fully described by the Compton angle reconstruction the missing parameter is the energy deposition in vertex 2 (E_{V2}). In the case of a Compton scattering in vertex 1, it can be assumed that in vertex 2 more than 160 keV is deposited as the maximal scattering angle of 180 degree would deposit an energy of about 478 keV. The charge yield for this energy region can be experimentally determined by the AmBe 164 keV and ^{137}Cs 662 keV calibration lines (see section 2.4.3). Since these calibrations cover the full energy interval in vertex 2, a linear interpolation of the charge yield can be used to calculate the deposited energy. Combining the information of E_γ, E_{V1} and E_{V2}, we can apply equation 4.4 to the double scatter event selection and derive figure 4.10. The histogram shows the distribution of the energy balance for each reconstructed event. For a perfect energy reconstruction in each vertex, the energy balance would add up to 0. Under the assumption that no systematic misidentification of the S2 size in vertex 2 occurs, and the source position is correctly determined, the distribution of the histogram indicates the precision of the Compton angle reconstruction in vertex 1. The red line denotes a Gaussian fit of the distribution and the estimation of the mean energy reconstruction is comparable to 0 within the uncertainties. This indicates that no bias to lower or higher energies is present in the event selection and the calculated Compton angles are Gaussian distributed around the true value. However, this statement is only valid for the average of the forward scattered photons and further studies need to verify this for each averaged energy interval.

The limited number of double scatter events in combination with maximal variations up to $\pm\,200$ keV result in too large uncertanties to determine the charge yield for energies below 40 keV. However, if we use equation 4.4 to select events which show an expected energy balance around 0, the quality of correct reconstructed Compton angles for double scattered photons will increase significantly. This selection is indicated in the range of $\pm\,20$ keV around 0 by the blue dashed line in figure 4.10. To study the effect of this selection on the results a range of $\pm\,60$ keV is also considered. In general, the energy

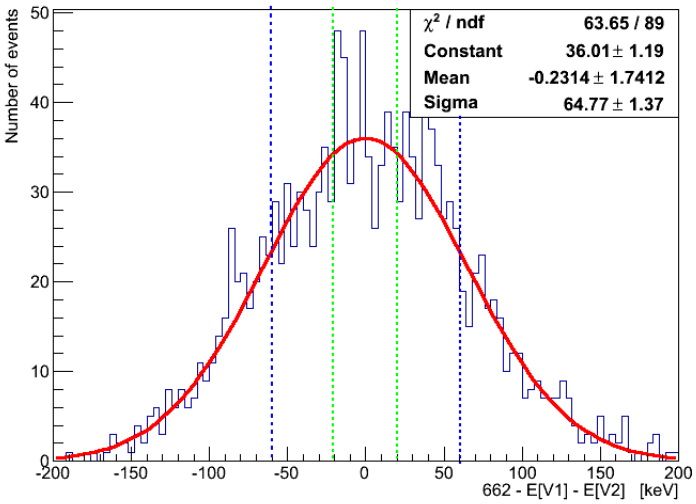

Figure 4.10: Energy balance of the energy estimation of vertex 1 and 2. The red lines represents a Gaussian fit of the distribution and indicates that the mean value is compatible to the expected value of 0. The green and blue dashed lines indicate the event selection for events with a $\pm 20\,\mathrm{keV}$ and $\pm 60\,\mathrm{keV}$ deviation of the energy balance, respectively.

balance requirement should be chosen as narrow as possible to reduce the uncertanties in the reconstructed energy but in the contrary a reasonable statistics has to be maintained.

4.3 Monte Carlo simulation of systematic errors

In section 4.2 it is shown that despite a careful selection of double scatter events, a rather high variation of the Compton angle reconstruction is present. To indentify the impact of known systematical uncertainties a toy Monte Carlo simulation of the kinematics and event selection is performed. The simulation considers all 3×3 spatial degrees of freedom as described in equation 4.2 as well as the limited energy resolution of the detector for the two energy depositions. In this approach, the simulation can account for a spatial variation of the source due to a varying radial position at each mounting of the source (see figure 2.6) as well as a reduced spatial resolution due to saturating PMTs.

The simulation distributes two verticies randomly in a cylidrical shape with the same dimensions as the XENON100 TPC. Following this, the same kinematic restrictions are applied on the simulated data as described in section 4.2, except the energy balance condition since it is used as an indicator of the systematic uncertainties.

In a third step of the simulation, the selected events are smeared according to the expected limitations of the experiment [47]. In vertex 1 and 2 the Z position resolution is estimated to be 0.3 mm. The XY resolution is 3 mm in vertex 1 and due to saturating PMTs only 12 mm in vertex 2, which is estimated from Monte Carlo studies of the position reconstruction algorithm in presence of saturating PMTs. The source position varyies radially since the placement of the source is not fixed at a precise position and is conservatively estimated to be around 5 cm (see section 2.4.3). The resulting variation of the energy balance condition can be seen in figure 4.11. A Gaussian fit of the distribution

reveals that the simulated uncertanties can account for aprroximately 70 % of the fluctuations in the measured data. Due to the uncertanties related to the reconstruction of

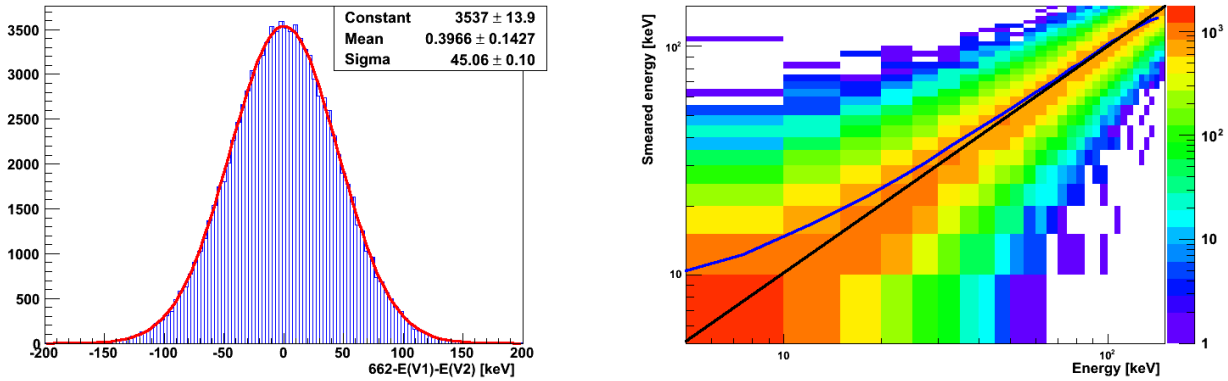

Figure 4.11: (Left) Energy balance requirement of simulated events, by considering limitations due to a varying source position and uncertaitnies of the vertex reconstruction. The red line indicates a Gaussian fit of the distribution and the estimated width accounts for approximatly 70 % of the uncertainties in the measured data. The right figure shows the distribution of simulated events of correctly reconstructed energies with respect to energies where the uncertanties have been applied. At energies above 70 keV the average reconstructed energy reproduces the inital energy deposition. However, at low energy depositions, the smeared values show an average which is larger than the true deposited energy.

the event kinematics, a smearing of the reconstructed energies among the bins is present. To illustrate this effect the right plot of figure 4.11 shows the values of simulated energy depositions where the true reconstructed energies are plotted with respect to the semeard values. At energies larger than 70 keV the average of the smeard values reproduce the true values. At lower values, however, the average value of the smeared values are larger than the true energy depositions. In vicinity of small energy depositions (< 70 keV), the events are not Gaussian distributed and the estimation of the mean energy deposition is biased by about 33 % to higher values as indicated by the difference of the blue and black line. Note that these effects account only for about 70 % of the uncertainties and the induced bias is even larger. It is obvious that this effect can not be neglected and therefore a correction has been derived (see section 4.4).

4.4 Computation of correction factors

To account for the systemtic effect due to events leaking to neigbouring bins, a correction for each energy bin has been computed. The size of the correction is determined by a Monte Carlo simulation of the energy spectrum of Compton scattered photons with an intial energy of 662 keV. Thus the energy spectrum in vertex 1 is given by the Compton scatter cross section. If T is the energy of the Compton recoil electron, the cross section in terms of T reads [78]:

$$\frac{d\sigma}{dT} = \frac{\pi \cdot r^2}{m_e c^2 \gamma^2} \left[2 + \frac{s^2}{\gamma^2 (1-s)^2} + \frac{s}{1-s} (s - \frac{2}{\gamma}) \right] \tag{4.5}$$

with $T_{max} = h\nu \left(\frac{2\gamma}{1+2\gamma}\right)$, $s = \frac{T}{h\nu}$ and $\gamma = \frac{h\nu}{m_e c^2}$. Here h denotes the Planck constant and ν the frequency of the photon.

The energy deposition in vertex 2 can be estimated by a linear interpolation of the charge yield from calibration measurements at 164 keV and 662 keV (see section 4.2.4). Thus, the largest uncertainties can be expected from the limitations of the independent Compton angle reconstruction. The energy balance condition gives a first estimate on the average uncertainty of the reconstructed energy deposition (see section 4.2.4). Thus after applying this condition, the error on the energy in vertex 1 will follow approximately a Gaussian distribution as seen in figure 4.10 within the selected energy interval (green and blue dashed lines). According to the energy balance condition, the smearing of the energy is applied to the simulated energy spectrum in vertex 1 and a correction factor for each bin can be computed.

The charge yield (CY) is defined by the ratio of the measured secondary scintillation signal (S2) and the deposited energy (E) as indicated by the following equation

$$\mathrm{CY} = \frac{\mathrm{S2}}{\mathrm{E}}. \tag{4.6}$$

Note that the simulation does not consider uncertainties in S2 since it does not simulate the S2 signal for a given energy deposition. The reconstructed energy in vertex 1 is averaged for each energy interval and the corresponding correction factor ξ for each energy bin i is then given by

$$\langle \mathrm{CY_c} \rangle_\mathrm{i} = \langle \mathrm{CY} \rangle_\mathrm{i} \cdot \xi_\mathrm{i}. \tag{4.7}$$

Each value for ξ can be computed individually for an energy bin i with

$$\xi_i = \langle \frac{\mathrm{CY_{smear}}}{\mathrm{CY}} \rangle_i = \langle \frac{\mathrm{E}}{\mathrm{E_{smear}}} \rangle_i. \tag{4.8}$$

The results can be seen in figure 4.12 for variation of the energy balance of ± 20 keV (left) and ± 60 keV (right).

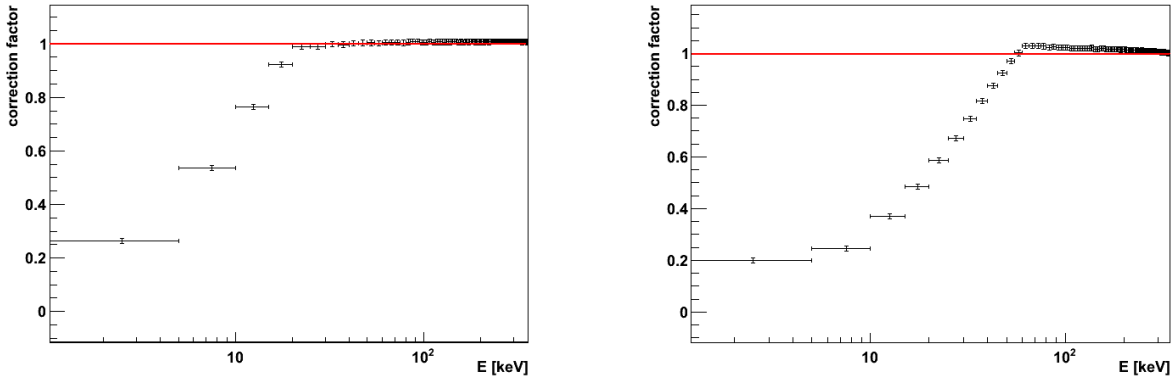

Figure 4.12: Computed correction factors for each energy bin for an uncertainty of ± 20 keV (left) and ± 60 keV (right). It can be seen that only low energy bins need to be corrected due to the vicinity of the physical boundary of small energy depositions.

What is expected that the Gaussian smearing in the absence of a physical boundary averages out for the high N limit and that the leakage effect is only visible at regions close

to the physical boundary of small energy depositions. So figure 4.12 can be interpreted as the solution of a combinatoric problem of leaking events from neighboring bins, by taking into account the expected energy spectrum in vertex 1. These computed correction factors estimated from the energy balance condition can be applied on the measured data by choosing the same energy bin width.

4.5 Charge yield results

After applying the selection criteria introduced in section 4.2 to ^{137}Cs calibration data, the resulting double scatter sample can be used to derive the charge yield for electronic recoil. This is done by dividing the sample in energy intervals of 5 keV, where the reconstructed energy is given by the Compton angle estimation. Then the corresponding S2 sizes in vertex 1 are averaged in each energy bin and the charge yield can be computed by equation 4.6. Finally, the correction factors are applied and the average charge yield is plotted with respect to the energy as indicated in figure 4.13 (left plots) by black markers. Note that the error bars on the charge yield only contain the statistical uncertainties and the small number of events (5 - 20) in each energy interval are one of the main limitations of this analysis. The charge yield of the calibration energies at 40 keV, 80 keV and 164 keV is shown by the red markers. The blue line is a semi empirical prediction of the charge yield [51] and is derived with the assumption of a perfect anti correlation between the light and charge yields (see section 2.5). Note that the NEST prediction is anchored to the 164 keV line for better comparison with the parameter of the XENON100 detector. The right plots show the relative deviation from the derived charge yield to the NEST curve. It can be seen that for energies above 70 keV the measured data is in agreement with the calibration lines at 80 keV and 164 keV as well as with the NEST model within the uncertainties. However, for lower energies a systematic deviation up to 60 % to higher values of the charge yield is visible. This deviation is present in the $\pm$ 20 keV and $\pm$ 60 keV energy balance conditions and the deviations to the NEST model (right figures) do not decrease significantly by narrowing the energy balance condition.

An independent determination of the deposited energy in vertex 1 can be calculated from vertex 2. With the parameterization of the charge yield between 164 keV and 662 keV from calibrations lines (see section 4.2.4) and the measured S2 signal in vertex 2, the energy deposition in vertex 1 is given by

$$\mathrm{E_{V1}} = \mathrm{E}_\gamma - \mathrm{E_{V2}}. \tag{4.9}$$

Given the energy in vertex 1, the charge yield can be computed according to figure 4.13. The results of this independent estimation of the energy deposition is shown in figure 4.14. Similar to figure 4.13, the charge yields are computed with an energy balance condition of $\pm$ 20 keV (left) and $\pm$ 60 keV (right). Again, the calculated charge yields at energies above 70 keV seem to be comparable to the calibration lines as well as the NEST prediction. The agreement of both energy estimators with the NEST prediction confirms the selection criteria of double scattered events. At lower energies figure 4.14 shows a systematic increase of the charge yield in comparison to the 40 keV calibration line as well to the NEST model.

The enhancement of the charge yield at around 30 keV might be explained by a resonance at the xenon K-edge and an emission of a X-ray at about 29.8 keV as well as

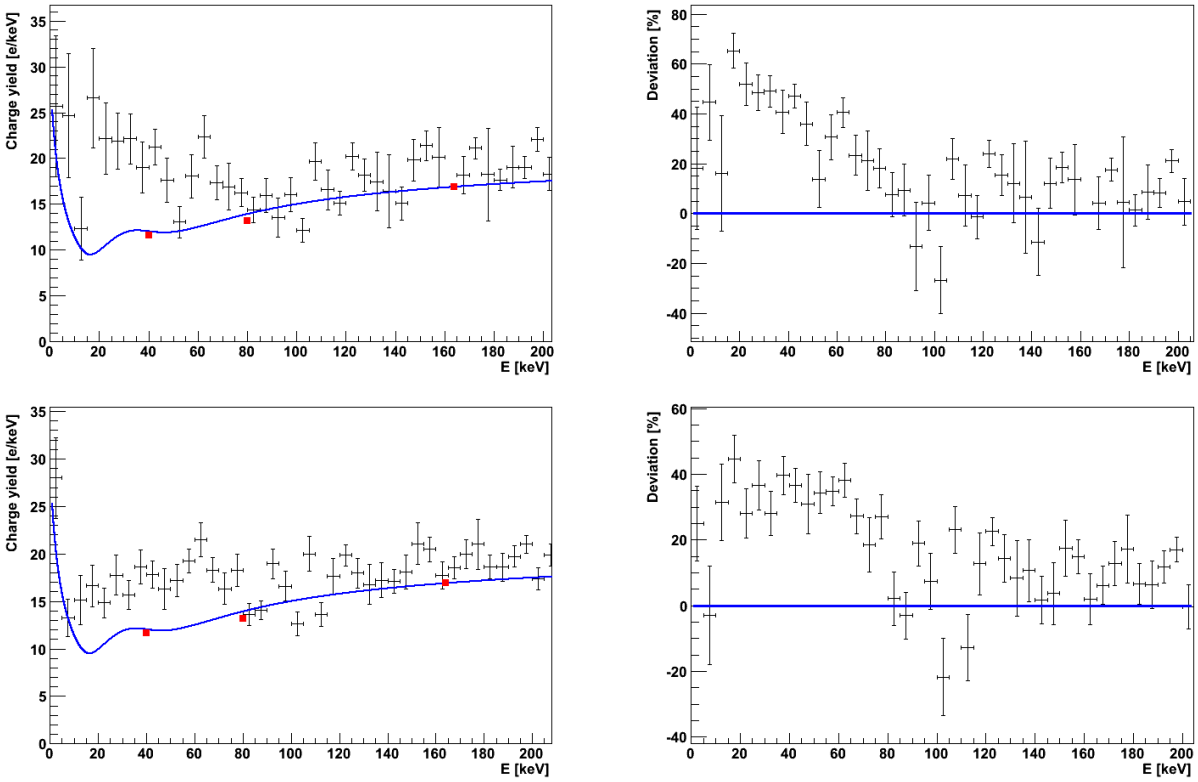

Figure 4.13: The left figures show the results of the computed charge yield from double scattered photons with respect to the energy deposition (black markers), where the energy balance condition is set to $\pm 20\,\mathrm{keV}$ (top) and $\pm 60\,\mathrm{keV}$ (bottom). The blue line denotes a semi empirical prediction published by the NEST collaboration [51] and the red markers show measurements at 40 keV, 80 keV and 164 keV measured with the XENON100 detector. The right figures shows the deviation of the charge yield derived from double scatter events to the predicted curve for an energy balance condition of $\pm 20\,\mathrm{keV}$ (top) and $\pm 60\,\mathrm{keV}$ (bottom). Above 70 keV both results are comparable within the uncertainties but at around 30 keV deviations up to 60 % can be seen. The population of deviating bins do not decrease for a more restrictive energy balance condition (top).

by the production of low energetic Auger electrons (see section 2.5). Both effects increase the number of interaction sites and reducing the total recombination probability.

4.6 Discussion

In this chapter a method in principle able to determine the charge yield of electronic recoils below 40 keV is introduced. A careful data selection of double scattered photons is performed and the Compton angle is reconstructed. A number of selection criteria are introduced to increase the quality of events, but some uncertainties in the data remain. Therefore, a thorough study of possible systematic errors is performed.

In a toy Monte Carlo simulation of the kinematic selection of double scatter events, the varying source position, the vertex resolution and the effect of saturating PMTs on the position reconstruction algorithm are simulated. It can account for approximately 70 %

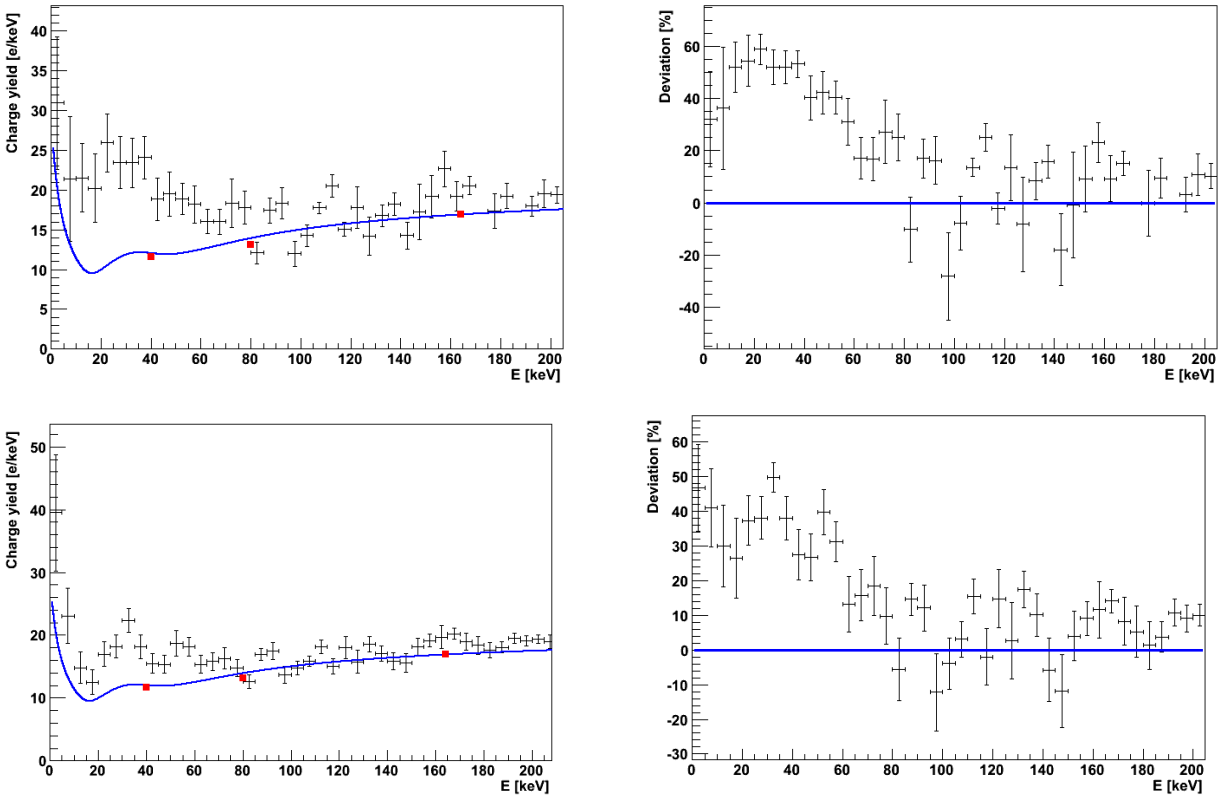

Figure 4.14: The figure shows the charge yields from NEST [51] (blue line) and from calibration lines (red) (see figure 4.13). The black markers show the charge yields derived in this work, however, the energy deposited in the Compton scatter vertex is estimated by the energy deposition in vertex 2. The figures show results, where the energy balance condition is set to $\pm 20\,\mathrm{keV}$ (top) and $\pm 60\,\mathrm{keV}$ (bottom).

of the variations, estimated by an energy balance condition. The remaining 30 % could be explained by too optimistic assumptions or by the remaining double scatter vertices which are not considered in the simulation. Further studies of the systematics including a complete simulation of double scatter events with all involved physical processes need to explain the observed systematic errors before final results can be stated.

The estimation of the uncertainties in the energy reconstruction allows a computation of correction factors determined from a Monte Carlo simulation. They are necessary due to a bias of the charge yield estimation at low energies. In the method of computing the corrections, it is assumed, that the main contribution to the uncertainties are due to the limitations of the Compton angle reconstructions in vertex 1. Thus the computation of correction factors can be improved by considering the energy resolution of about 15 % in vertex 2. So far the S2 fluctuations in vertex 1 and 2 have been neglected as well as a bias to larger values in the S2 size estimation. Similar to the energy smearing, the S2 values are not Gaussian distributed at low energy depositions. However, this is more difficult to consider in a simulation as the S2 size distribution for a given energy is the function of interest.

Despite the remaining uncertainties, the computed charge yields above 70 keV are comparable to a semi empirical prediction [51] and to the charge yield derived from

calibration sources at 80 keV and 164 keV. At energy depositions below 70 keV, deviations up to 60 % can be observed. This result can be verified by an independent method to determine the charge yield, where the energy is reconstructed from the information present in vertex 2.

A limitation of this analysis is the small number of available calibration data. Improving this, the introduced event selection criteria could not only be set more restrictive but averaging over more events in each bin would decrease the statistical error. In addition, saturating PMTs influence strongly the vertex resolution in vertex 2. A different operating voltage of the PMTs would increase the precision of the introduced method. The next generation detector XENON1T will not be affected by these limitations and could improve this analysis considerably. In addition, this analysis can not only be applied to electronic recoil but given a monoenergetic neutron source, the charge yield for nuclear recoil can also be determined with minor changes in the selection of events.

Chapter 5

Representing results in the minimal velocity parameter space

> *Reports that say that something hasn't happened are always interesting to me, because as we know, there are known knowns; there are things we know that we know. There are known unknowns; that is to say, there are things that we now know we don't know. But there are also unknown unknowns there are things we do not know we don't know.*
>
> United States Secretary of Defense, Donald Rumsfeld

Direct detection dark matter experiments generally display their results in terms of the cross section with respect to the particles mass. This chapter is devoted to the *known unknowns*, that are the assumptions on the dark matter velocity distribution in the Milky Way and its involved astrophysical parameters. These uncertainties impede a comparison between the various existing results of direct detection experiments as the *unknowns* affect results in different ways. In this chapter a method is introduced which displays experimental dark matter results in a parameter space that is independent of astrophysical assumptions. This enables a better comparison between of the experimental results. After an introduction of the method, bounds on WIMP interactions with the target atoms are derived from measurements of the XENON100 detector.

5.1 Impact of astrophysical uncertainties on direct detection experiments

Assumptions on the dark matter velocity distribution as well as astrophysical parameters such as the escape velocity, velocity dispersion or the local dark matter density influence the sensitivity of direct detection experiments to WIMP interactions. Since experiments use different target nuclei and show varying energy thresholds the sensitive velocity interval will differ from one experiment to another. To quantify this effect, the differential scattering rate is calculated for a dark matter particle for a target nucleus with respect to the dark matter mass and velocity.

For this, the relation between the recoil energy (E_r) and velocity (v) has to be derived. If a dark matter particle with a mass m_χ and a kinetic energy $E = \frac{1}{2} m_\chi \cdot v^2$ scatters off a

target with the mass m_A at an angle θ the recoil energy E_r can be written in the center of mass system as

$$E_r = E \cdot \frac{m_\chi m_A}{(m_\chi + m_A)^2} \cdot \frac{(1 - \cos(\theta))}{2}. \tag{5.1}$$

And accordingly,

$$E = E_r \cdot \left(\frac{m_\chi m_A}{(m_\chi + m_A)^2} \cdot \frac{(1 - \cos(\theta))}{2} \right)^{-1} = \frac{1}{2} m_\chi \cdot v^2. \tag{5.2}$$

For the further calculation it is useful to drop the dependency of the scattering angle θ. Thus by considering the smallest kinetic energy E_{min} which can produce a recoil energy E_r, the scattering angle can be set to 180°. The corresponding velocity to E_{min} is defined as the minimal velocity v_{min} and given by,

$$v_{min}(E_r) = \sqrt{\frac{m_A \cdot E_r}{2\mu_A^2}} \tag{5.3}$$

where $\mu_A = \frac{m_\chi m_A}{(m_\chi + m_A)}$ describes the reduced mass.

To be able to make a statement on the interaction probability of a dark matter particle with the target nucleus, the Feynman amplitude of a hypothetical interaction needs to be computed. An effective interaction of a dark matter particle scattering off a target nucleus can be seen in figure 5.1. The letters P and K denote the incoming and outgoing

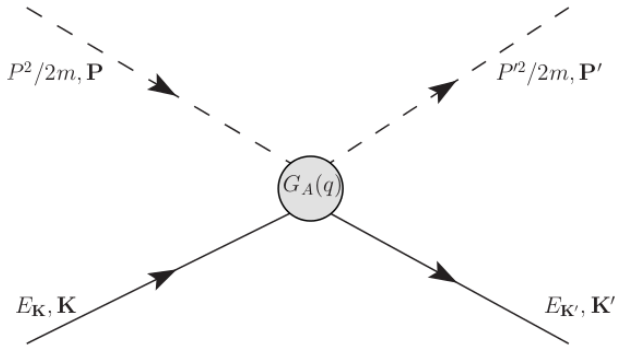

Figure 5.1: Feynman diagram for dark matter particle scattering off a target nucleus where P and K denote the initial and final momenta of the dark matter particle and the target nucleus, respectively. The corresponding energies are shown by a normal font. The vertex of the effective interaction is indicated by the grey circle [79].

momenta of the dark matter particle and target nucleus, respectively. Their energies are denoted by the letters in normal font and the effective interaction is indicated by $G_A(q)$, the grey circle in the center of the figure. Accordingly to the Feynman rules

the differential scattering rate can be computed [79]. If q is the momentum transfer a calculation yields to

$$\left(\frac{d(\sigma v)}{d\mathrm{E_{nr}}}\right) = \frac{m_\mathrm{A}}{\mathrm{v}}|\mathrm{G_A(q)}|^2\frac{1}{2\pi}\Theta(\mathrm{v}-\frac{\mathrm{q}}{2\mu_\mathrm{A}}). \tag{5.4}$$

Note that the step function represents the energy threshold of a detector since it corresponds to a cut off for interactions at too low energy depositions.

For spin-independent and isospin conserving interactions (see chapter 1) the vertex factor is given by [79]

$$|\mathrm{G_A(q)}|^2 = \frac{\pi\sigma_\mathrm{SI}\mathrm{A}^2\mathrm{F}_\mathrm{A}^2(\mathrm{q})}{\mu_\mathrm{p}^2}. \tag{5.5}$$

Where σ_SI is the spin independent cross section, A the mass number of the target atom, $\mathrm{F_A}$ the nuclear form factor and μ_p^2 the reduced mass of the WIMP and proton masses. By using the Helm form factor [26] and writing the nuclear recoil energy in terms of the minimal velocity (eq. 5.3), the differential cross section with respect to the target mass and dark matter velocity can be calculated. Note that the mass number A can be expressed by $\mathrm{A} = \mathrm{m/u}$ with u being the atomic mass unit. Figure 5.2 illustrates the interaction probability (color coded) that a 9 GeV (top) and 50 GeV (bottom) dark matter particle scatters off a nucleus with respect to the minimal velocity and mass of the target element. The left plots represent a detector with an energy threshold of 0.5 keV similar to the CDMS experiment [16] and, in the right plot, a XENON100 like energy threshold of 5 keV. The bright colors indicate a lower interaction probability than the darker colors, the absolute values however are arbitrary. The plots visualize that with an increasing element mass the interaction probability rises with A^2. Moreover, the sensitivity for low WIMP velocities is strongly influenced by a higher energy threshold at low WIMP masses. So comparing experimental results measured with targets consisting of an element mass of 29 GeV (Si) and an energy threshold of 0.5 keV to a target element with 129 GeV (Xe) and an energy threshold of 5 keV is difficult, since they probe different velocity intervals. This effect most pronounced for WIMP masses below 10 GeV. For higher WIMP masses and velocities, the momentum transfer is enhanced and the coherence loss due to the form factor suppresses the interaction probability.

In summary, this study tries to point out that different detectors with individual energy thresholds and target elements are sensitive to different dark matter velocities. Since the dark matter halo and its parameters remains unknown, it is useful to display the direct detection results in a model independent way.

5.2 The minimal velocity parameter space

Usually dark matter searches display experimental results in terms of the cross section and WIMP mass, derived from the model dependent dark matter recoil rate (see section 1.4). The assumptions on the astrophysical parameters (see section 1.5) which are necessary to derive the expected differential rate of dark matter interactions with matter can be seen in equation 5.6,

$$\frac{\mathrm{dR_A}}{\mathrm{dE_{nr}}} = \frac{\sigma_\mathrm{A}^{SI}}{2\mathrm{m}_\chi\mu_\mathrm{A}^2}\rho_\chi \cdot \int_{v\geq v_{min}} \mathrm{d^3v}\cdot\frac{\mathrm{f(\mathbf{v},t)}}{\mathrm{v}}. \tag{5.6}$$

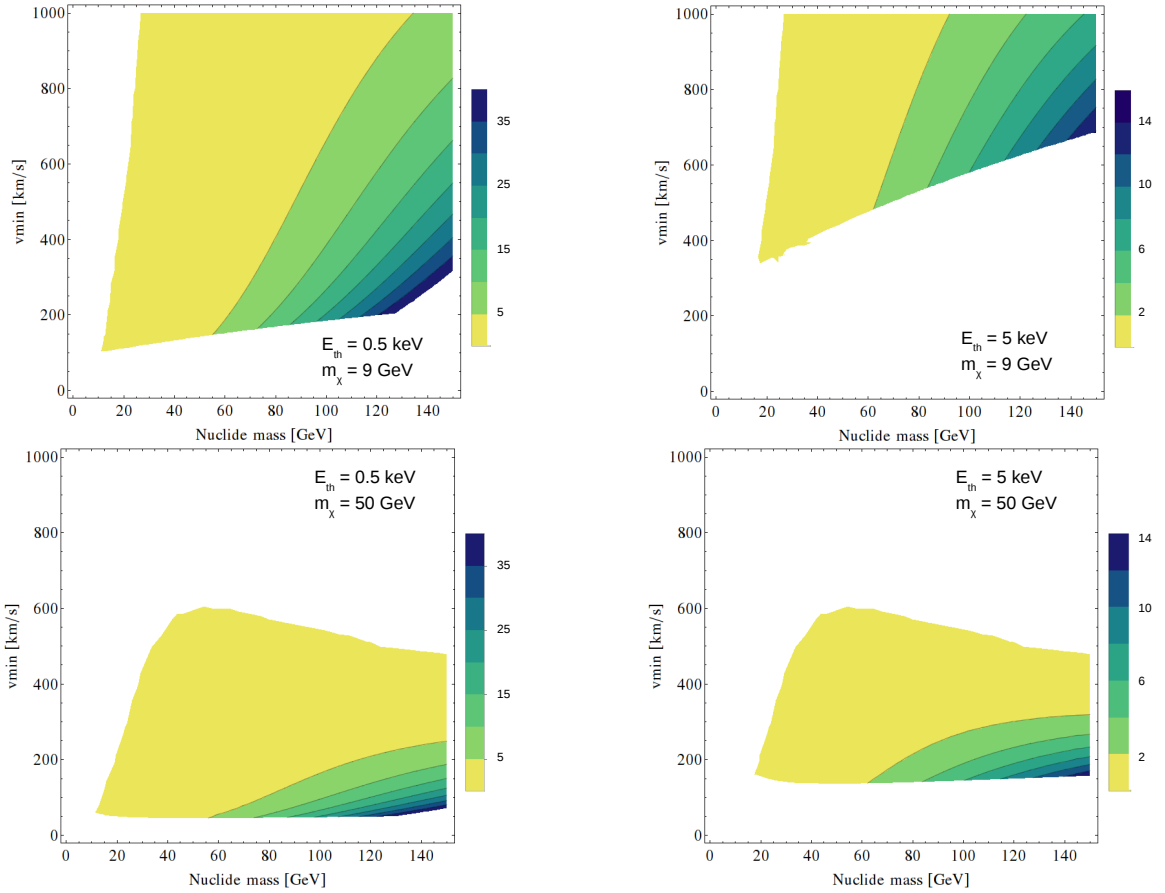

Figure 5.2: The plot shows the minimal velocity of a 9 GeV WIMP (top plots) and 50 GeV (bottom plots) WIMP with respect to the mass of the target element. The color coded scale represents the Feynman amplitude and can be interpreted as an interaction probability of the WIMP with the target nucleus, where darker colors indicate an increasing probability, however, with arbitrary absolute values. The left plots are computed for a low energy threshold of approximately 0.5 keV which can be achieved in a CDMS-like detector. In addition, a higher energy threshold of 5 keV, similar to the XENON100 detector is shown in the right figures. The interaction probability increases with A^2 for heavier elements. Moreover, the sensitivity for low WIMP velocities is strongly influenced by a higher energy threshold for light WIMP masses. For heavy WIMP masses and velocities, the momentum transfer increases and the coherence loss due to the form factor suppresses the interaction probability.

Where ρ_χ denotes the local dark matter density and $f(\mathbf{v}, t)$ the velocity distribution of the dark matter halo in terms of the dark matter velocity v and time t (see section 1.5). To avoid the uncertainties on the astrophysical parameters, it can be useful to display experimental results without these assumptions. This can be done by combining the method of mapping the energy into the minimal velocity as introduced in equation 5.3, with the expected WIMP interaction rate as shown in equation 5.6. Inserting the definition of spin independent cross section as introduced in equation 1.6 results in,

$$\frac{dR_A}{dE_{nr}} = \frac{\sigma_p \cdot A^2 \cdot F_A^2(E)}{2m_\chi \cdot \mu_p^2} \rho_\chi \cdot \int_{v \geq v_{min}} d^3v \cdot \frac{f(\mathbf{v}, t)}{v}. \tag{5.7}$$

Furthermore, it is shown in [80] that the parameter

$$\tilde{\eta}(\mathrm{v_{min}}, \mathrm{t}) = \frac{\sigma_\mathrm{p} \cdot \rho_\chi}{\mathrm{m}_\chi} \int_{\mathrm{v} \geq \mathrm{v_{min}}} \mathrm{d}^3\mathrm{v} \cdot \frac{\mathrm{f}(\mathbf{v}, \mathrm{t})}{\mathrm{v}}, \tag{5.8}$$

is common to all experiments and includes astrophysical assumptions such as the velocity distribution of the dark matter halo, escape velocity, velocity dispersion and the local dark matter density. By displaying results of direct dark matter experiments in $(\tilde{\eta}(\mathrm{v_{min}}, \mathrm{t}), \mathrm{v_{min}})$ parameter space, the comparison of the outcome is independent of astrophysical assumptions. Note that $\tilde{\eta}(\mathrm{v_{min}}, \mathrm{t})$ is generally depend on the time due to the revolution of the Earth around the Sun. The largest recoil energies are expected when the Earth moves in the direction opposite to the Galactic rotation. Thus the parameter $\tilde{\eta}$ is not only sensitive to a constant flux of dark matter particles in the halo but can measure an annular modulation. An approximation by the first terms of a harmonic series yields,

$$\eta(\mathrm{v_{min}}, \mathrm{t}) = \eta_0(\mathrm{v_{min}}) + \eta_1(\mathrm{v_{min}}) \cdot \cos(\omega(\mathrm{t} - \mathrm{t}_0)). \tag{5.9}$$

Here $\eta_0(\mathrm{v_{min}})$ denotes the unmodulated part of $\eta(\mathrm{v_{min}})$ and $\eta_1(\mathrm{v_{min}})$ describes the amplitude of the modulation in terms of the time t and angular frequency ω. The following calculation will focus on the unmodulated part η_0. Thus equation 5.7 can be rewritten as,

$$\frac{\mathrm{dR_A}}{\mathrm{dE_{nr}}} = \mathrm{A}^2 \cdot \frac{\tilde{\eta_0}(\mathrm{v_{min}}, \mathrm{t})}{2\mu_\mathrm{p}^2} \cdot \mathrm{F_A^2(E)}. \tag{5.10}$$

5.2.1 Minimal velocity space for XENON100

Equation 5.10 is derived for a recoil spectrum without any considerations of experimental limitations and physical properties of the target. The analysis procedure for XENON100 is introduced in section 2.4, and here the extension to the parameter η, defined in the previous section, is presented. By considering the relevant physical processes involved in the signal generation in XENON100 the calculation of the total number of expected signal events leads to

$$\mathrm{N} = \mathrm{T} \cdot \int_{\mathrm{S1_{min}}}^{\mathrm{S1_{max}}} \mathrm{dS1} \cdot \epsilon(\mathrm{S1}) \cdot \int_0^\infty \mathrm{dE_{nr}} \cdot \sum_{\mathrm{n}=1}^{\infty} \left(\frac{\mathrm{dR_A}}{\mathrm{dE_{nr}}} \cdot \frac{\nu(\mathrm{E_{nr}})^\mathrm{n}}{\mathrm{n!}} \cdot \mathrm{e}^{-\nu(\mathrm{E_{nr}})} \right) \frac{1}{\sqrt{2\pi n} \cdot \sigma_\mathrm{PMT}} \cdot e^{\frac{-(\mathrm{n}-\mathrm{S1})^2}{2\mathrm{n}\sigma_\mathrm{PMT}^2}}. \tag{5.11}$$

Where the parameter T describes the exposure of a science run, which is defined by the product of the fiducial mass and measured time span. The acceptances in terms of S1 are expressed by the function ϵ(S1) and the fluctuations due to the small number of detected photons is characterized by a Poisson function with the expectation value $\nu(\mathrm{E_{nr}})$. The finite resolution of the PMTs are considered by a Gaussian distribution with a width σ_{PMT} (see section 2.6). In order to compute the expected number of events N with respect to the model independent parameter η the recoil energy $\mathrm{E_{nr}}$ has to be mapped to the minimal velocity $\mathrm{v_{min}}$ as introduced in section 5.1. By using equation 5.3 the derivative of $\mathrm{E_{nr}}$ with respect to $\mathrm{v_{min}}$ yields

$$\mathrm{dE_{nr}} = \frac{4\mu_\mathrm{A}^2}{\mathrm{m_A}} \cdot \mathrm{v_{min}} \mathrm{dv_{min}}. \tag{5.12}$$

By defining a constant $\xi = 2\frac{\mu_A^2}{m_A}$ and using the relation for the recoil energy 5.12, equation 5.11 can be expressed in terms of the minimal velocity,

$$\mathrm{N} = \mathrm{T} \cdot \int_{\mathrm{S1_{min}}}^{\mathrm{S1_{max}}} \mathrm{dS1} \cdot \epsilon(\mathrm{S1}) \cdot \int_0^{\infty} \mathrm{dv_{min}} \cdot 2\xi \cdot \mathrm{v_{min}} \cdot \sum_{\mathrm{n=1}}^{\infty} \frac{\mathrm{dR_A}}{\mathrm{dE_{nr}}} \frac{\nu(\mathrm{v_{min}^2} \cdot \xi \cdot \mathcal{L}_{\mathrm{eff}} \cdot \frac{\mathrm{S_{nr}}}{\mathrm{S_{ee}}} \cdot \mathrm{L_y})^{\mathrm{n}}}{\mathrm{n!}}$$
$$e^{-\nu(\mathrm{v_{min}^2} \cdot \xi \cdot \mathcal{L}_{\mathrm{eff}} \cdot \frac{\mathrm{S_{nr}}}{\mathrm{S_{ee}}} \cdot \mathrm{L_y})} \cdot \frac{1}{\sqrt{2\pi n} \cdot \sigma_{\mathrm{PMT}}} \cdot e^{\frac{-(\mathrm{n}-\mathrm{S1})^2}{2\mathrm{n}\sigma_{\mathrm{PMT}}^2}}. \quad (5.13)$$

The recoil rate $\frac{\mathrm{dR_A}}{\mathrm{dE_{nr}}}$ in terms of $\tilde{\eta}$ is given by equation 5.10. In addition, the spin independent nuclear form factor (Helm form factor) is parameterized by [26]

$$\mathrm{F_{SI}(q)} = 3 \cdot \frac{\sin(\mathrm{qr}) - \mathrm{qr} \cdot \cos(\mathrm{qr})}{(\mathrm{qr})^3} \quad (5.14)$$

with the momentum transfer $\mathrm{q} = \sqrt{2\mathrm{m_A E_r}}$ and the effective atom radius $\mathrm{r} = 1.0 \cdot \mathrm{A}^{1/3}\mathrm{fm}$. Equation 5.14 can be mapped into the minimal velocity parameter space via 5.3

$$\mathrm{F_{SI}(v_{min})} = 3 \cdot \frac{\sin(2\mathrm{v_{min}} \cdot \mu_\mathrm{A} \cdot \mathrm{r}) - 2\mathrm{v_{min}} \cdot \mu_\mathrm{A} \cdot \mathrm{r} \cdot \cos(2\mathrm{v_{min}} \cdot \mu_\mathrm{A} \cdot \mathrm{r})}{(2\mathrm{v_{min}} \cdot \mu_\mathrm{A} \cdot \mathrm{r})^3}. \quad (5.15)$$

Inserting equation 5.10 in 5.13 the expected number of events can be expressed by:

$$\mathrm{N} = \mathrm{T} \cdot \frac{2 \cdot \mu_\mathrm{A}^2 \cdot \mathrm{A}^2}{\mu_\mathrm{p}^2 \cdot \mathrm{m_A}} \cdot \int_{\mathrm{S1_{min}}}^{\mathrm{S1_{max}}} \mathrm{dS1} \cdot \epsilon(\mathrm{S1}) \cdot \int_0^{\infty} \mathrm{dv_{min}} \cdot \mathrm{v_{min}} \cdot$$
$$\left(3\frac{\sin(2\mathrm{v_{min}} \cdot \mu_\mathrm{A} \cdot \mathrm{r}) - 2\mathrm{v_{min}} \cdot \mu_\mathrm{A} \cdot \mathrm{r} \cdot \cos(2\mathrm{v_{min}} \cdot \mu_\mathrm{A} \cdot \mathrm{r})}{(2\mathrm{v_{min}} \cdot \mu_\mathrm{A} \cdot \mathrm{r})^3}\right)^2$$
$$\sum_{n=1}^{\infty} \tilde{\eta_0}(\mathrm{v_{min}}, \mathrm{t}) \cdot \frac{(\mathrm{v_{min}^2} \cdot \xi \cdot \mathcal{L}_{\mathrm{eff}} \cdot \frac{\mathrm{S_{nr}}}{\mathrm{S_{ee}}} \cdot \mathrm{L_y})^{\mathrm{n}}}{\mathrm{n!}} \cdot \mathrm{e}^{-(\mathrm{v_{min}^2} \cdot \xi \cdot \mathcal{L}_{\mathrm{eff}} \cdot \frac{\mathrm{S_{nr}}}{\mathrm{S_{ee}}} \cdot \mathrm{L_y})} \cdot \frac{1}{\sqrt{2\pi \mathrm{n}}\sigma_{\mathrm{PMT}}} \cdot \mathrm{e}^{\frac{-(\mathrm{n}-\mathrm{S1})^2}{2\mathrm{n}\sigma_{\mathrm{PMT}}^2}} \quad (5.16)$$

If the integration order over dS1 and $\mathrm{dv_{min}}$ is changed, it is possible rewrite the lengthy equation in a more general form:

$$\mathrm{N} = \mathrm{T} \cdot \int_0^{\infty} \mathrm{dv_{min}} \mathcal{R} \cdot \tilde{\eta_0}(\mathrm{v_{min}}, \mathrm{t}) \quad (5.17)$$

with $\mathcal{R}$ being the spin-independent response function for XENON100,

$$\mathcal{R} = \frac{2 \cdot \mu_A^2 \cdot \mathrm{A}^2}{\mu_p^2 \cdot \mathrm{m_A}} \cdot \int_{S1_{min}}^{S1_{max}} dS1 \cdot \epsilon(\mathrm{S1}) \cdot \mathrm{v_{min}} \cdot$$
$$\left(3\frac{\sin(2\mathrm{v_{min}} \cdot \mu_\mathrm{A} \cdot \mathrm{r}) - 2\mathrm{v_{min}} \cdot \mu_\mathrm{A} \cdot \mathrm{r} \cdot \cos(2\mathrm{v_{min}} \cdot \mu_\mathrm{A} \cdot \mathrm{r})}{(2v_{min} \cdot \mu_A \cdot r)^3}\right)^2$$
$$\sum_{n=1}^{\infty} \frac{(\mathrm{v_{min}^2} \cdot \xi \cdot \mathcal{L}_{\mathrm{eff}} \cdot \frac{\mathrm{S_{nr}}}{\mathrm{S_{ee}}} \cdot \mathrm{L_y})^{\mathrm{n}}}{n!} \cdot e^{-(v_{min}^2 \cdot \xi \cdot \mathcal{L}_{eff} \cdot \frac{S_{nr}}{S_{ee}} \cdot L_y)} \cdot \frac{1}{\sqrt{2\pi \cdot n}\sigma_{\mathrm{PMT}}} \cdot e^{\frac{-(\mathrm{n}-\mathrm{S1})^2}{2\mathrm{n}\sigma_{\mathrm{PMT}}^2}}. \quad (5.18)$$

5.2.2 Deriving limits in v_{min} space

To constrain the velocity integral η [1] we can make use of the knowledge that the integral of any velocity distribution of the dark matter halo is a non increasing function. In this case, an upper bound on the velocity applies also to all lower velocities and, thus, the most conservative form that that an upper bound on $\tilde{\eta}(v_{min})$ can take is a step function [80]:

$$\tilde{\eta}(v_{min}) \geq \tilde{\eta}(\hat{v}_{min}) \cdot \Theta(\hat{v}_{min} - v_{min}). \tag{5.19}$$

A physical interpretation of this approximation would be to consider a dark matter stream with the velocity $\hat{v}_{min}$. This can be performed for every v_{min} value in the relevant velocity interval. Combining equations 5.19 and 5.17 yields,

$$N = T \cdot \int_0^\infty dv_{min} \mathcal{R} \cdot \tilde{\eta}(\hat{v}_{min}) \cdot \Theta(\hat{v}_{min} - v_{min}). \tag{5.20}$$

Due to the approximation in equation 5.19, the velocity is fixed in $\tilde{\eta} = \tilde{\eta}(\hat{v}_{min})$ and can be pulled out of the overall velocity integral. In addition, the step function changes the upper integration variable to the finite velocity $\hat{v}_{min}$.

$$N^{lim} = T \cdot \tilde{\eta}(\hat{v}_{min}) \int_0^{\hat{v}_{min}} dv_{min} \cdot \mathcal{R}(v_{min}). \tag{5.21}$$

The upper bound on the total number of signal events N^{lim} can be determined by a non significant dark matter result of the XENON100 detector. Since results are a combination of signal and background events, it is necessary to calculate the maximal number of expected events which can be solely explained by the background in the absence of a signal. In this work, the method proposed by Feldman and Cousins is used to derive the upper bounds on N^{lim} for a 90 % confidence level [71]. Finally equation 5.17 can be solved for $\tilde{\eta}$

$$\tilde{\eta}(\hat{v}_{min}) = \frac{N^{lim}}{T \cdot \int_0^{\hat{v}_{min}} \mathcal{R}(v_{min})}. \tag{5.22}$$

This assumption can be used in an analysis for the unmodulated signal to determine the upper bounds on $\tilde{\eta}$. Thus for any velocity integral with $\eta(\hat{v}_{min}) = \eta_0$ the one defined by $\eta(v_{min}) = \eta_0 \cdot \Theta(\hat{v}_{min} - v_{min})$ predicts the smallest number of events for a given experimental null result. To visualize this mathematical formulation figure 5.3 shows the method of setting bounds on η in the minimal velocity space. For a given velocity $\hat{v}_{min}$ it is possible to compute the corresponding value for $\tilde{\eta}$ with equation 5.22 which defines the amplitude of the step function as introduced in equation 5.19 (dashed red lines). This can be done for each $\hat{v}_{min}$ in the sensitive velocity interval. The bound on $\tilde{\eta}$ is then derived by the curve which intersects the step function at the corresponding velocity (black line).

5.3 Results of the XENON100 science run I and II

By using equation 5.22, the detector response function for XENON100 derived in equation 5.18 and the experimental results of the two longest science runs I and II of 100 live days

[1] In the following only bounds on the unmodulated part of η are derived and the notation is changed to $\eta \equiv \eta_0$.

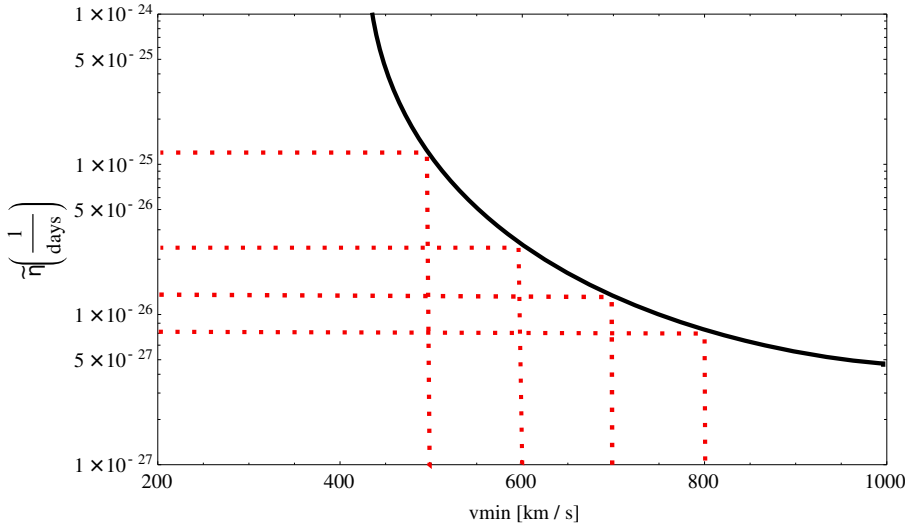

Figure 5.3: Visualization of the method to set limits in the minimal velocity parameter space. The dashed line indicates the bound on $\tilde{\eta}(\hat{\mathrm{v}}_{\mathrm{min}})$ which is determined by an experimental null results. The black line illustrates the resulting limit by intersecting each individual bound. Method from [80].

[64] and 225 live days [65], it is possible to derive the bounds on $\tilde{\eta}$ with the method derived in section 5.2.2. The limits for $\mathrm{N}^{\mathrm{lim}}$ can be computed by considering the values in table 5.1 and applying the method of Feldman and Cousins [71]. Note that the response function

Science run	Expected background	Measured events	Signal limit at 90 % CL
I	1.8	3	5.67
II	1.0	2	4.91

Table 5.1: Published results of science run I [64] and II [65]. The limits on the number the signal events are derived using the method of Feldman and Cousins [71].

depends on the event selection acceptances published in [64] and [65] and are displayed and explained in section 2.4.4. Applying all acceptances according to the XENON100 method (see section 2.6), the derived bounds on η are shown for a 7 GeV (left) and 9 GeV (right) WIMP in figure 5.4. It can be seen that the bounds are weaker for the 7 GeV WIMP mass than for a 9 GeV WIMP interaction. The bounds at low velocities are determined by the 6.6 $\mathrm{keV}_{\mathrm{nr}}$ energy threshold of the XENON100 detector. As a comparison, an independent determination of the derived limits in figure 5.4 can be seen in figure 5.5 (purple line) as it was published in [81]. In addition, various other experimental bounds are given in the minimal velocity parameter space.

In [81], instead of applying the S2 threshold as a further acceptance curve, a cut off at 6.6 $\mathrm{keV}_{\mathrm{nr}}$ in the light yield function $\mathcal{L}_{eff}$ (see section 2.5) is performed. This neglects the exact shape of the S2 acceptance as seen in figure 2.8. The difference of both procedures

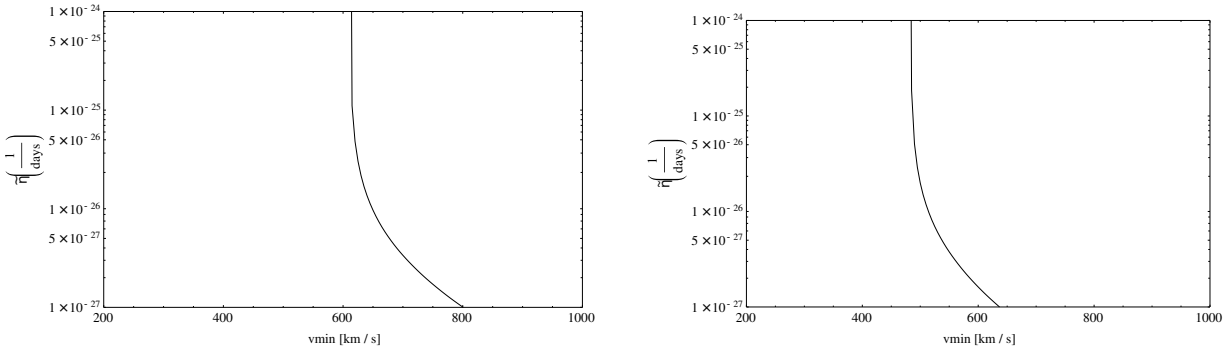

Figure 5.4: Bounds on WIMP interactions in the minimal velocity parameter space derived from science run II [65] for a 7 GeV (left) and 9 GeV (right). The bounds on $\tilde{\eta}$ improve for larger WIMP masses. The limit at small velocities is solely determined by the 6.6 $\mathrm{keV_{nr}}$ energy threshold of the XENON100 detector.

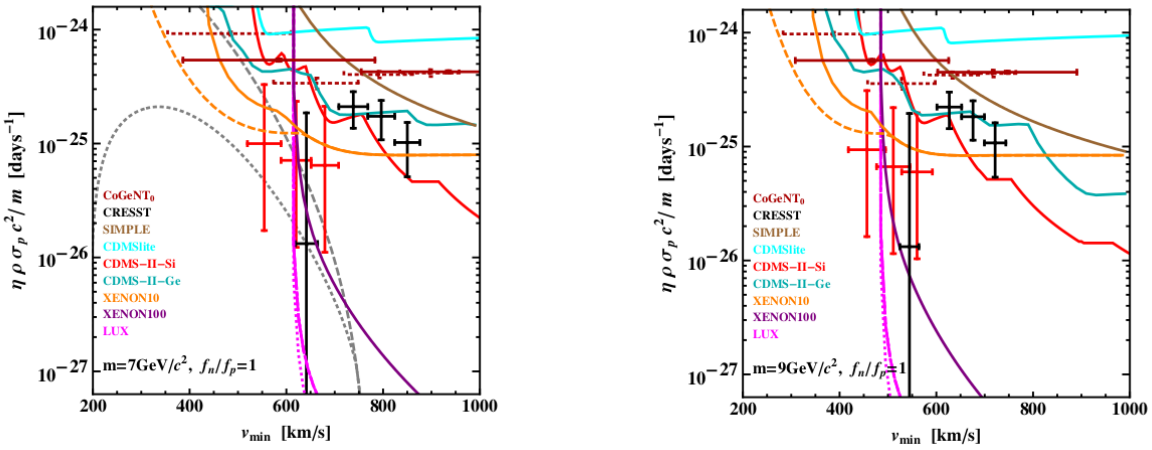

Figure 5.5: Published bounds on $\tilde{\eta}$ by a fixed dark matter mass of 7 GeV (left) and 9 GeV (right) for various direct detection experiments. Figure from [81].

can be seen in figure 5.6. The black line shows the effect of the direct cut off. However, the limit is slightly overestimated by neglecting the exact shape (red line).

The bounds on $\tilde{\eta}$ is expected to be lower for science run I, due to the lower exposure and higher background expectation of this run. A limit derived from science run I can be seen in figure 5.7 and is indicated by the blue line.

5.3.1 Combining results from different runs

A simple method to combine the experimental results is given in [26] if the target is composed of different elements. The authors state that if the cross-section limit is determined separately for each element of a detector, an improved combined limit can be obtained

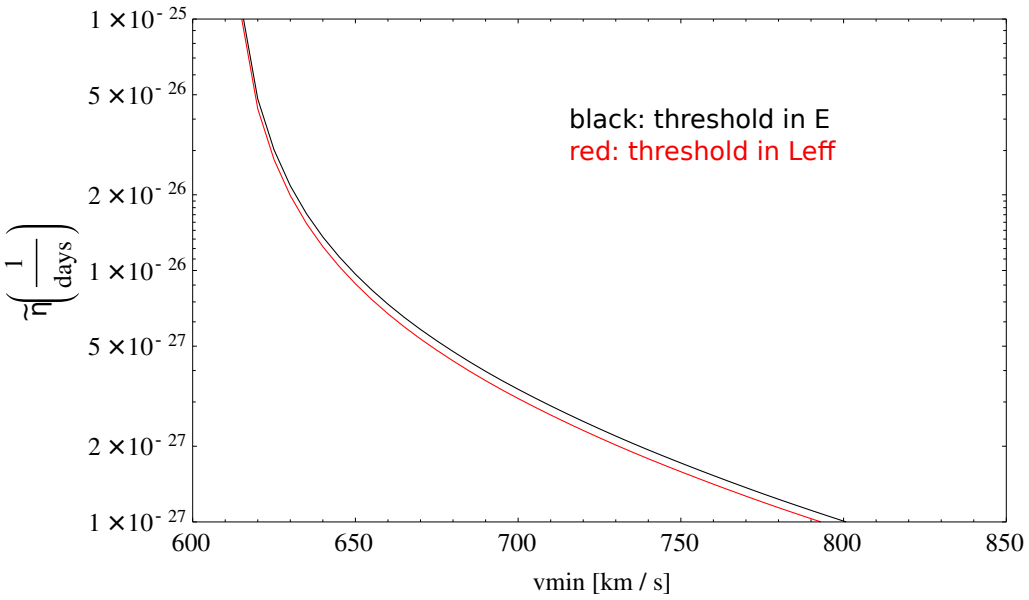

Figure 5.6: Differences of the bounds on $\tilde{\eta}$ for a 7 GeV WIMP when accounting for the exact shape of the S2 threshold cut acceptance. Various publications (e.g. [81]) neglect this acceptance and apply a cut off condition directly on the light yield function $\mathcal{L}_{eff}$ as shown by the black line. However, the limit is slightly overestimated by neglecting the exact shape (red line).

by using

$$\frac{1}{\sigma} = \sum_{A} \frac{1}{\sigma(A)}. \tag{5.23}$$

This method allows to determine the cross-section limit for each element individually, by considering the relevant acceptances and background acceptances. Since XENON100 consists of only one element the mass fraction C is set to 1. The calculation of the combined limit can be achieved by extending the rate equation 5.10 so that it accounts for each individual target element.

$$\frac{\mathrm{dR_A}}{\mathrm{dE_{nr}}} = \sum_{\mathrm{A}} \mathrm{C_A} \cdot \mathrm{A}^2 \cdot \frac{\tilde{\eta}(\mathrm{v_{min}}, \mathrm{t})}{2\mu_{\mathrm{p}}^2} \cdot \mathrm{F_A^2(E)}. \tag{5.24}$$

In this work a similar procedure is followed to combine data from different runs. By defining the total exposure as $\mathrm{T} = \sum_{\mathrm{i}} \mathrm{T_i}$ with i labeling a dataset and $\mathrm{T_i}$ the exposure of a single dataset, then the fraction of a individual $\mathrm{C_i}$ can be computed with $\mathrm{C_i} = \frac{\mathrm{T_i}}{\mathrm{T}}$. And this translates to $\tilde{\eta}$ with

$$\tilde{\eta}(\hat{\mathrm{v}}_{\mathrm{min}})_{\mathrm{i}} = \sum_{\mathrm{i}} \frac{\mathrm{N^{lim}(i)}}{T \cdot \mathrm{C_i} \cdot \int_0^{\hat{\mathrm{v}}_{\mathrm{min}}} \mathcal{R}_{\mathrm{i}}(\mathrm{v_{min}})}, \tag{5.25}$$

with T being the summed exposure of all considered science runs and $N^{lim}(i)$ denotes the upper bound of the signal events for each run i. Applying equation 5.23 to the velocity integral the combined bound can be calculated with

$$\frac{1}{\tilde{\eta}} = \sum_{i} \frac{1}{\tilde{\eta}(\hat{v}_{min})_i}. \tag{5.26}$$

A resulting limit can be seen in figure 5.7 which shows the individual XENON100 bounds for a 9 GeV WIMP on $\tilde{\eta}$ for science run I (blue) and science run II (black) publications. The combined limit is shown by the red line. As expected for higher

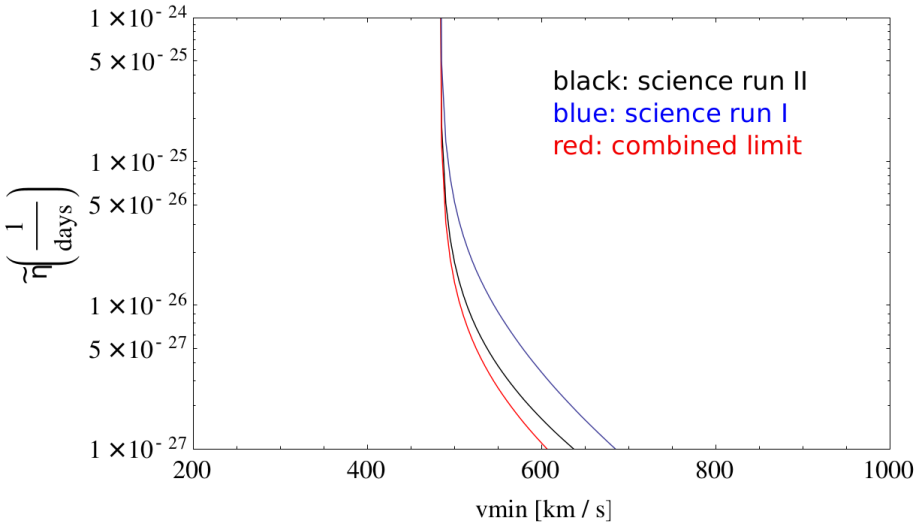

Figure 5.7: The bounds on $\tilde{\eta}$ for a 9 GeV WIMP derived from science run I (blue) and science run II (black) data is shown. The red line indicates the improved limit by combining the two science runs.

velocities the limit improves due to the increased exposure, but at velocities close to the energy threshold the limit does not get stronger. Only a better performance such as an increased light yield of the detector could lower the energy threshold strengthening the limit. This is a rather simple method of combining bounds on $\tilde{\eta}$ and further studies have to show that the coverage remains at 90 % confidence level.

5.3.2 Quantifying the influence of astrophysical parameters

The analysis in the minimal velocity space enables a quantification of the impact of astrophysical parameters on the bounds on $\tilde{\eta}$ due to the separation of detector dependent parameters and astrophysical assumptions. As introduced in section 1.5 the values for the local dark matter density, the velocity dispersion or the escape velocity are difficult to determine and systematic uncertainties remain non negligible. In addition the velocity distribution itself is modeled and simulated in different ways and, again, the systematic uncertainties are not negligible [42, 46].

The influence of these systematic errors can be tested in the minimal velocity parameter space. Figure 5.8 shows in black a bound on $\tilde{\eta}$ as it is calculated in section 5.3. The blue line represents a region of the halo model with fixed set of the astrophysical

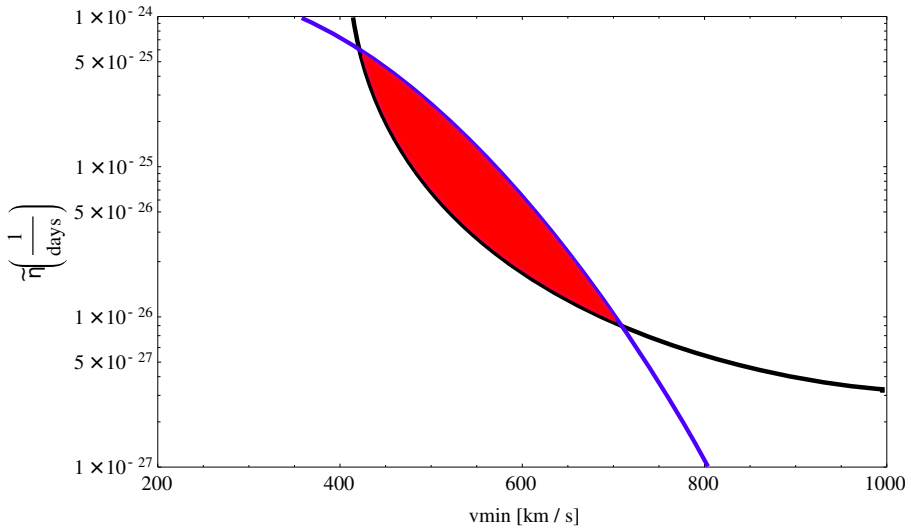

Figure 5.8: In this sketch, the blue line represents a standard halo model [30] with fixed set of the astrophysical parameters and the black line shows the bound on $\tilde{\eta}$ for a given WIMP mass. The red area illustrates the actual physical model which is tested by the experiment.

parameters [29, 30]. The red area shows the actual physical model which is tested by the experiment. Only if such an intersection between the bounds and the calculated values for $\tilde{\eta}$ exist, physical values of the dark matter interaction can be probed.

The influence of individual astrophysical parameters for a fixed halo model has been tested. The results for various combinations of parameters are shown in figure 5.9. In each plot the black line denotes a bound on a 9 GeV WIMP derived from science run II. The blue line shows the integral of the velocity distribution parameterized by a truncated Maxwell-Boltzmann distribution with the standard values of $\rho = 0.3\,\mathrm{GeV}$, $v_{esc} = 540\,\mathrm{km/s}$ and $v_0 = 220\,\mathrm{km/s}$. The red and green lines denote the minimal and maximal values stated in publications [28, 29], respectively (see section 1.5). In the top left figure the escape velocity is varied from 498 km/s to 608 km/s [40] and has a minor influence only at large velocities. The top right plot indicates a variation of the local dark matter density from $\rho = 0.11\,\mathrm{GeV}$ to $\rho = 1.25\,\mathrm{GeV}$ [34, 35]. Since this parameter is not influenced by the dark matter velocity distribution, it scales the limit homogeneously up and down. However it changes the value of $\tilde{\eta}$ significantly. The lower left plot displays the influence of the velocity dispersion for 200 km/s and 279 km/s [35, 39]. The influence on velocity integral is also significant. To point out the problematic with an extreme case, all values are varied to their maximal and minimal values in the lower right figure. In this case, the red line does not intersect the experimentally determined limit and XENON100 would not be sensitive to a 9 GeV WIMP. Note, however, that this is an extreme example

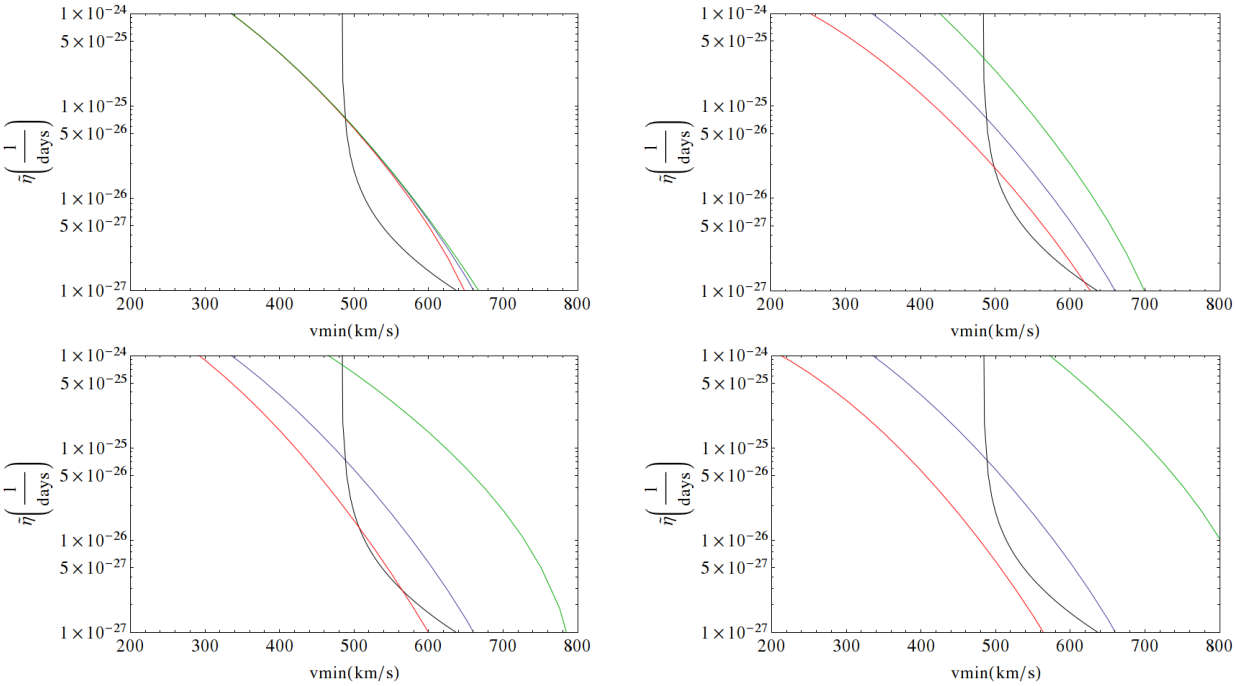

Figure 5.9: These plots show the influence of the astrophysical uncertainties relative to the bounds for $\tilde{\eta}$ (black line) in the minimal velocity parameter space, derived from science run II for a 9 GeV WIMP. The blue line shows the integral of the velocity distribution parameterized by a truncated Maxwell-Boltzmann distribution with the standard values of $\rho = 0.3\,\text{GeV}$, $v_{esc} = 540\,\text{km/s}$ and $v_0 = 220\,\text{km/s}$. The red and green lines denote the minimal and maximal values stated in [28]. In the top left figure the escape velocity is varied from 498 km/s to 608 km/s and has a minor influence only at large velocities. The top right plot indicates a variation of the local dark matter density from $\rho = 0.11\,\text{GeV}$ to $\rho = 1.25\,\text{GeV}$. The lower left plot displays the influence of the velocity dispersion for 200 km/s and 279 km/s (details see text).

not supported by a certain halo simulation.

The effect of different halo models (see section 1.5) can be seen in figure 5.10, where the parameter g on the y-axis is directly proportional to $\tilde{\eta}$ [82]. The solid blue line shows the standard halo model and the colored dashed lines represent different assumptions on the velocity distribution of the dark matter particles. By fixing the astrophysical parameters and changing the halo model, significant deviations can be observed.

5.4 Discussion

A number of experiments try to measure WIMP interactions by using different detector technologies and target elements. Hence, energy thresholds and sensitivities to light or heavy WIMP masses differ. Due to the uncertainties of the velocity distribution as well as in measurements of the astrophysical parameters, a comparison of experiments in the parameter space of the cross section and WIMP mass is dependent on an astrophysical model. In this work, a method is introduced to display experimental results of dark matter searches independently of such astrophysical uncertainties. For this it is necessary

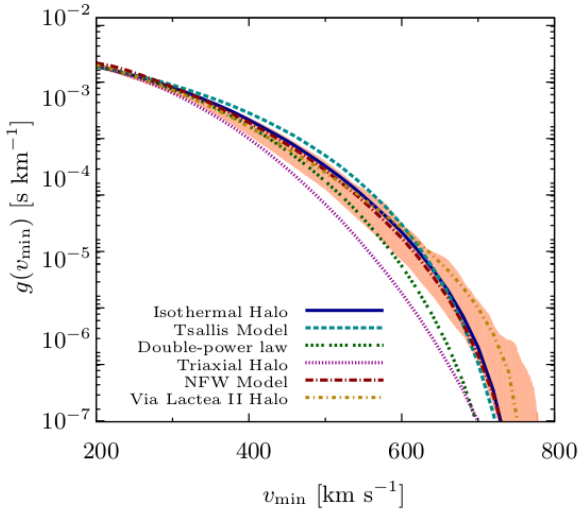

Figure 5.10: Halo models for a different scaling of $\tilde{\eta}$ with respect to the minimal velocity. The blue line displays the standard halo model and the dashed lines represent different parameterizations of the velocity distribution of dark matter particles in the halo. It can be seen that changes of the halo model result in significant deviations. Figure from [82].

to derive the detector response function for the XENON100 experiment which accounts not only for the relevant acceptances but also considers statistical effects in the process of a signal generation. So far this is done by selection of a benchmark region which results in an acceptance loss. For simplicity, the method proposed by Feldman and Cousins [71] has been used to set limits. However, future studies will use the profile likelihood method which is used in the standard XENON100 analysis [66]. In addition a two dimensional analysis, taking both signals S1 and S2 into account could further improve the sensitivity of the XENON100 detector.

A simple method to combine the results of different science runs is introduced, which can improve the bounds on velocity integral due to an increased exposure. It is to mention that further studies have to prove that the coverage of the method is at 90 % C.L.

Finally the influence of astrophysical parameters as well as different velocity distributions on the velocity integral are studied. This is possible due to the separation of the detector dependent quantities and astrophysical assumptions in the minimal velocity parameter space. In this way, it is possible to determine the sensitive velocity interval of an detector and can reveal that experiments are not sensitive to certain astrophysical models due to the large uncertainties in astrophysical measurements. In the $(\tilde{\eta}, \mathrm{v}_{\min})$ parameter space, the outcome of different experiments can be better compared as the velocity intervals are shown explicitly.

Chapter 6

Conclusions

In this work three different analysis related to dark matter searches with XENON100 are presented. The first chapter motivates the quest for a direct detection of dark matter and tries to summarize the current knowledge of these particles beyond the standard model derived from indirect searches. The second chapter describes in detail the XENON100 detector, beginning with the concept of a dual phase TPC and the experimental setup, to conclude with a selection of published results from the XENON100 experiment.

The third chapter is dedicated to the performance of the detector during science run III between 2013 and 2014. The light and charge yield is derived from various different energies. It is shown that the charge yield is reduced by around 5 % in comparison to run II due to an increased liquid level. In addition, an improved method to derive the S2 size corrections is introduced which enables a significantly higher energy resolution of the detector. This is possible by estimating the S2 size variations from calibration data which is measured by a 100 % extraction efficiency of the electrons. To improve these corrections more statistics is necessary to achieve a higher spatial resolution of the S2 size corrections.

In chapter four a method is developed to estimate the charge yield for electronic recoils with the XENON100 detector, which is at the same time the first direct measurement of the charge yield for non zero drift fields. A precise knowledge of the yield is necessary to search for dark matter candidates (e.g. axions, ALPs) producing electronic recoils. This can be achieved by a kinematic reconstruction of double scattered photons, enabled by dedicated selection criteria to tag Compton scattered photons. For energies larger than 70 keV a semi empirical prediction [51] can be verified. However, around energy depositions of 30 keV a larger charge yield than expected is observed. This requires further studies but might be explained by Compton scatters on the K-shell electrons close to this energy. A simulation of systematic errors can already explain 70 % of the observed uncertainties, but further studies have to explain the remaining 30 % which are still present in the analysis as well as a full Monte Carlo simulation with GEANT4 should be performed.

Finally, a method is used to set limits independently of astrophysical uncertainties. Limits derived for science run I and II in the new parameter space verify the calculations which have been published by independent groups in the last years. In addition, a method is used to combine science run I and II to increase the total exposure, resulting in stronger bounds on WIMP interactions. Furthermore, it can be shown that this parameter space

can be used to study the impact systematic uncertainties in astrophysical parameters. So far this analysis is based on the predefined WIMP search region and an analysis using the profile likelihood method will improve the sensitivity, by considering the exact distribution of background events.

The XENON100 detector showed an excellent performance but is mostly limited through its small fiducial volume. The next generation detector XENON1T [83] will improve the performance twofold: Not only by increasing the target volume by more than one order of magnitude but by further reducing the internal and external backgrounds by a factor of 100. This enables to increase the sensitivity for spin-independent WIMP-nucleon cross-section parameter down to $10^{-47}\,\mathrm{cm}^2$.

Bibliography

[1] F. Zwicky, "Die Rotverschiebung von extragalaktischen Nebeln," *Helvetica Physica Acta* **6** (1933) 110.

[2] **Planck** Collaboration, P. Ade *et al.*, "Planck 2013 results. I. Overview of products and scientific results," arXiv:1303.5062.

[3] **WMAP** Collaboration, G. Hinshaw *et al.*, "Nine-Year Wilkinson Microwave Anisotropy Probe (WMAP) Observations: Cosmological Parameter Results," *Astrophys. J. Suppl.* **208** (2013) 19, arXiv:1212.5226.

[4] D. Tytler, J. M. O'Meara, N. Suzuki, and D. Lubin, "Review of Big Bang Nucleosynthesis and Primordial Abundances," *Physica Scripta Volume T* **85** (2000) 12, astro-ph/0001318.

[5] V. Springel, C. S. Frenk, and S. D. White, "The large-scale structure of the Universe," *Nature* **440** (2006) 1137, arXiv:astro-ph/0604561.

[6] M. Bartelmann and P. Schneider, "Weak gravitational lensing," *Phys. Rept.* **340** (2001) 291, arXiv:astro-ph/9912508.

[7] M. Bradac, S. W. Allen, T. Treu, H. Ebeling, R. Massey, *et al.*, "Revealing the properties of dark matter in the merging cluster MACSJ0025.4-1222," *Astrophys. J.* **687** (2008) 959, arXiv:0806.2320.

[8] D. Clowe, M. Bradac, A. H. Gonzalez, M. Markevitch, S. W. Randall, *et al.*, "A direct empirical proof of the existence of dark matter," *Astrophys. J.* **648** (2006) L109, arXiv:astro-ph/0608407.

[9] V. C. Rubin, N. Thonnard, and W. K. Ford, "Extended rotation curves of high-luminosity spiral galaxies.," *Astrophys. J* **225** (1978) L107.

[10] S. Tremaine and J. E. Gunn, "Dynamical role of light neutral leptons in cosmology," *Phys. Rev. Lett.* **42** (1979) 407.

[11] G. Bertone, ed., *Particle Dark Matter*. Cambridge, 2010.

[12] G. Bertone, ed., *Particle Dark Matter*, ch. 7. Cambridge, 2010.

[13] **DAMA/LIBRA** Collaboration, R. Bernabei *et al.*, "New results from DAMA/LIBRA," *Eur. Phys. J.* **C67** (2010) 39, arXiv:1002.1028.

[14] **LUX** Collaboration, D. Akerib *et al.*, "First results from the LUX dark matter experiment at the Sanford Underground Research Facility," arXiv:1310.8214.

[15] **XENON100** Collaboration, E. Aprile *et al.*, "Limits on spin-dependent WIMP-nucleon cross sections from 225 live days of XENON100 data," *Phys. Rev. Lett.* **111** (2013) 021301, arXiv:1301.6620.

[16] **SuperCDMS** Collaboration, R. Agnese *et al.*, "Search for Low-Mass WIMPs with SuperCDMS," arXiv:1402.7137.

[17] C. Baker, D. Doyle, P. Geltenbort, K. Green, M. van der Grinten, *et al.*, "An Improved experimental limit on the electric dipole moment of the neutron," *Phys. Rev. Lett.* **97** (2006) 131801, arXiv:hep-ex/0602020.

[18] G. Bertone, ed., *Particle Dark Matter*, ch. 11. Cambridge, 2010.

[19] **XENON100** Collaboration, E. Aprile *et al.*, "First Axion Results from the XENON100 Experiment," (2014) , arXiv:1404.1455.

[20] S. Arrenberg, L. Baudis, K. Kong, K. T. Matchev, and J. Yoo, "Kaluza-Klein Dark Matter: Direct Detection vis-a-vis LHC (2013 update)," arXiv:1307.6581.

[21] **Fermi-LAT** Collaboration, M. Ackermann *et al.*, "Dark Matter Constraints from Observations of 25 Milky Way Satellite Galaxies with the Fermi Large Area Telescope," *Phys. Rev.* **D89** (2014) 042001, arXiv:1310.0828.

[22] E. Bulbul, M. Markevitch, A. Foster, R. K. Smith, M. Loewenstein, and S. W. Randall, "Detection of An Unidentified Emission Line in the Stacked X-ray spectrum of Galaxy Clusters," (2014) , arXiv:1402.2301.

[23] A. Boyarsky, O. Ruchayskiy, D. Iakubovskyi, and J. Franse, "An unidentified line in X-ray spectra of the Andromeda galaxy and Perseus galaxy cluster," (2014) , arXiv:1402.4119.

[24] A. Drukier, K. Freese, and D. Spergel, "Detecting Cold Dark Matter Candidates," *Phys. Rev.* **D33** (1986) 3495.

[25] P. Gondolo, "Either neutralino dark matter or cuspy dark halos," *Phys. Lett. B* **494** (2000) 181–186, hep-ph/0002226.

[26] J. Lewin and P. Smith, "Review of mathematics, numerical factors, and corrections for dark matter experiments based on elastic nuclear recoil," *Astropart. Phys.* **6** (1996) 87.

[27] G. Bertone, ed., *Particle Dark Matter*, ch. 17. Cambridge, 2010.

[28] A. M. Green, "Astrophysical uncertainties on direct detection experiments," *Mod. Phys. Lett.* **A27** (2012) 1230004, arXiv:1112.0524.

[29] A. M. Green, "Dependence of direct detection signals on the WIMP velocity distribution," *JCAP* **10** (2010) 34, arXiv:1009.0916.

[30] A. M. Green, "Effect of halo modeling on weakly interacting massive particle exclusion limits," *Phys. Rev. D* **66** no. 8, (2002) 083003, astro-ph/0207366.

[31] M. J. Reid, "The distance to the center of the galaxy," *Annual Review of Astronomy and Astrophysics* **31** (1993) 345.

[32] C. Francis and E. Anderson, "Two estimates of the distance to the Galactic centre," (2013) , arXiv:1309.2629.

[33] Y. Sofue, M. Honma, and T. Omodaka, "Unified Rotation Curve of the Galaxy – Decomposition into de Vaucouleurs Bulge, Disk, Dark Halo, and the 9-kpc Rotation Dip," *PASJ* **61** (2009) 227, arXiv:0811.0859.

[34] M. Weber and W. de Boer, "Determination of the local dark matter density in our Galaxy," *Astron. Astrophys.* **509** (2010) A25, arXiv:0910.4272.

[35] S. Garbari, J. I. Read, and G. Lake, "Limits on the local dark matter density," *MNRAS* **416** (2011) 2318–2340, arXiv:1105.6339.

[36] J. Oort, "The force exerted by the stellar system in the direction perpendicular to the galactic plane and some related problems," *Bull. of the Astron. Inst. of the Netherlands* **6** (1932) 249.

[37] J. I. Read, "The Local Dark Matter Density," (2014) , arXiv:1404.1938.

[38] F. J. Kerr and D. Lynden-Bell, "Review of galactic constants," *MNRAS* **221** (1986) 1023–1038.

[39] P. J. McMillan and J. J. Binney, "The uncertainty in galactic parameters," *MNRAS* **402** (2010) 934–940, arXiv:0907.4685.

[40] M. C. Smith *et al.*, "The rave survey: constraining the local galactic escape speed," *MNRAS* **379** (2007) 755–772, astro-ph/0611671.

[41] I. R. King, "The structure of star clusters. III. Some simple dynamical models," *AJ* **71** (1966) 64.

[42] N. W. Evans, C. M. Carollo, and P. T. de Zeeuw, "Triaxial haloes and particle dark matter detection," *MNRAS* **318** (2000) 1131–1143, astro-ph/0008156.

[43] J. Diemand, M. Kuhlen, and P. Madau, "Dark Matter Substructure and Gamma-Ray Annihilation in the Milky Way Halo," *ApJ* **657** (2007) 262–270, astro-ph/0611370.

[44] J. Stadel, D. Potter, B. Moore, J. Diemand, P. Madau, *et al.*, "Quantifying the heart of darkness with GHALO - a multi-billion particle simulation of our galactic halo," *Mon. Not. Roy. Astron. Soc.* **398** (2009) L21, arXiv:0808.2981.

[45] V. Springel, J. Wang, M. Vogelsberger, A. Ludlow, A. Jenkins, *et al.*, "The Aquarius Project: the subhalos of galactic halos," *Mon. Not. Roy. Astron. Soc.* **391** (2008) 1685, arXiv:0809.0898.

[46] M. Kuhlen, N. Weiner, J. Diemand, P. Madau, B. Moore, D. Potter, J. Stadel, and M. Zemp, "Dark matter direct detection with non-Maxwellian velocity structure," *JCAP* **2** (2010) 30, arXiv:0912.2358.

[47] **XENON100** Collaboration, E. Aprile *et al.*, "The XENON100 Dark Matter Experiment," *Astropart. Phys.* **35** (2012) 573, arXiv:1107.2155.

[48] A. Lansiart, A. Seigneur, J.-L. Moretti, and J.-P. Morucci, "Development research on a highly luminous condensed xenon scintillator," *Nucl. Instrum. Meth.* **135** (1976) 47.

[49] **MACRO** Collaboration, M. Ambrosio *et al.*, "Vertical muon intensity measured with MACRO at the Gran Sasso laboratory ," *Phys. Rev. D* **52** (1995) 7.

[50] E. Aprile and T. Doke, "Liquid xenon detectors for particle physics and astrophysics," *Rev. Mod. Phys.* **82** (2010) 2053, arXiv:0910.4956.

[51] M. Szydagis, N. Barry, K. Kazkaz, J. Mock, D. Stolp, M. Sweany, M. Tripathi, S. Uvarov, N. Walsh, and M. Woods, "Nest: A comprehensive model for scintillation yield in liquid xenon," (2011) , arXiv:1106.1613.

[52] C. Dahl, *The physics of background discrimination in liquid xenon, and first results from XENON10 in the hunt for WIMP dark matter*. PhD thesis, Princeton University, 2009.

[53] T. Doke, A. Hitachi, S. Kubota, A. Nakamoto, and T. Takahashi, "Estimation of fano factors in liquid argon, krypton, xenon and xenon-doped liquid argon," *Nuc. Instrum. Methods Phys.* **134** no. 2, (1976) 353 – 357.

[54] **XENON10** Collaboration, J. Angle *et al.*, "A search for light dark matter in XENON10 data," *Phys. Rev. Lett.* **107** (2011) 051301, arXiv:1104.3088.

[55] E. Aprile, K. L. Giboni, P. Majewski, K. Ni, and M. Yamashita, "Observation of anticorrelation between scintillation and ionization for mev gamma rays in liquid xenon," *Phys. Rev. B* **76** no. 1, (2007) 014115, arXiv:0704.1118.

[56] T. Doke, H. Crawford, A. Hitachi, J. Kikuchi, P. Lindstrom, *et al.*, "Let Dependence of Scintillation Yields in Liquid Argon," *Nucl.Instrum.Meth.* **A269** (1988) 291–296.

[57] J. Birks, "The theory and practice of scintillation counting," *International Series of Monographs on Electronics and Instrumentation* **27** (1964) .

[58] J. Thomas and D. Imel, "Recombination of electron-ion pairs in liquid argon and liquid xenon," *Phys. Rev.* **A36** (1987) 614.

[59] P. Sorensen and C. E. Dahl, "Nuclear recoil energy scale in liquid xenon with application to the direct detection of dark matter," *Phys. Rev. D* **83** no. 6, (2011) 063501, arXiv:1101.6080.

[60] M. Szydagis, A. Fyhrie, D. Thorngren, and M. Tripathi, "Enhancement of nest capabilities for simulating low-energy recoils in liquid xenon," *J. Instr.* **8** (2013) C3, http://arxiv.org/abs:1307.6601.

[61] Firestone R.B. and Ekstroem L.P., "*Periodic chart of the nuclides.*" http://nucleardata.nuclear.lu.se/NuclearData/toi/, February, 1999.

[62] **XENON100** Collaboration, E. Aprile *et al.*, "Analysis of the XENON100 Dark Matter Search Data," *Astropart. Phys.* **54** (2014) 11, arXiv:1207.3458.

[63] E. Aprile *et al.*, "Observation and applications of single-electron charge signals in the xenon100 experiment," arXiv:1311.1088.

[64] **XENON100** Collaboration, E. Aprile *et al.*, "Dark Matter Results from 100 Live Days of XENON100 Data," *Phys. Rev. Lett.* **107** (2011) 131302, arXiv:1104.2549.

[65] **XENON100** Collaboration, E. Aprile *et al.*, "Dark Matter Results from 225 Live Days of XENON100 Data," *Phys. Rev. Lett.* **109** (2012) 181301, arXiv:1207.5988.

[66] **XENON100** Collaboration, E. Aprile *et al.*, "Likelihood Approach to the First Dark Matter Results from XENON100," *Phys. Rev.* **D84** (2011) 052003, arXiv:1103.0303.

[67] **XENON100** Collaboration, E. Aprile *et al.*, "Implications on Inelastic Dark Matter from 100 Live Days of XENON100 Data," *Phys. Rev.* **D84** (2011) 061101, arXiv:1104.3121.

[68] **XENON100** Collaboration, E. Aprile *et al.*, "Response of the XENON100 Dark Matter Detector to Nuclear Recoils," *Phys. Rev.* **D88** (2013) 012006, arXiv:1304.1427.

[69] L. Baudis, H. Dujmovic, C. Geis, A. James, A. Kish, *et al.*, "Response of liquid xenon to Compton electrons down to 1.5 keV," *Phys. Rev.* **D87** (2013) 115015, arXiv:1303.6891.

[70] E. Aprile, C. Dahl, L. DeViveiros, R. Gaitskell, K. Giboni, *et al.*, "Simultaneous measurement of ionization and scintillation from nuclear recoils in liquid xenon as target for a dark matter experiment," *Phys. Rev. Lett.* **97** (2006) 081302, arXiv:astro-ph/0601552.

[71] G. Feldman and R. Cousins, "Unified approach to the classical statistical analysis of small signals," *Phys. Rev. D* **57** no. 7, (1998) 3873–3889, physics/9711021.

[72] S. Lindemann, *Intrinsic 85Kr and 222Rn Backgrounds in the XENON Dark Matter Search.* PhD thesis, Ruperto-Carola-University of Heidelberg, 2013.

[73] **XENON100** Collaboration, E. Aprile *et al.*, "Study of the electromagnetic background in the XENON100 experiment," *Phys. Rev.* **D83** (2011) 082001, arXiv:1101.3866.

[74] M. Weber. Personal communication.

[75] A. Manalaysay, T. Marrodán Undagoitia, A. Askin, L. Baudis, A. Behrens, *et al.*, "Spatially uniform calibration of a liquid xenon detector at low energies using ^{83m}Kr," *Rev. Sci. Instrum.* **81** (2010) 073303, arXiv:0908.0616.

[76] H. J. H. and S. S. M., "*Tables of X-Ray Mass Attenuation Coefficients and Mass Energy-Absorption Coefficients from 1 keV to 20 MeV for Elements Z = 1 to 92 and 48 Additional Substances of Dosimetric Interest*." http://www.nist.gov/pml/data/xraycoef/index.cfm, May, 1996.

[77] V. A. Rabinovich and L. Veksler, "Collection GSSD," *Standards Press* **2** (1970) .

[78] W. R. Leo, ed., *Techniques for Nuclear and Particle Physics Experiments: A How-to Approach*, ch. 2. Springer, Berlin, 1994.

[79] R. Laha and E. Braaten, "Direct detection of dark matter in universal bound states," (2013) , arXiv:1311.6386.

[80] P. J. Fox, J. Liu, and N. Weiner, "Integrating out astrophysical uncertainties," *Phys. Rev. D* **83** no. 10, (2011) 103514, arXiv:1011.1915.

[81] E. Del Nobile, G. B. Gelmini, P. Gondolo, and J.-H. Huh, "Update on light WIMP limits: LUX, lite and light," *JCAP* **3** (2014) 14, arXiv:1311.4247.

[82] M. T. Frandsen, F. Kahlhoefer, C. McCabe, S. Sarkar, and K. Schmidt-Hoberg, "Resolving astrophysical uncertainties in dark matter direct detection," *JCAP* **1** (2012) 24, arXiv:1111.0292.

[83] **XENON1T** Collaboration, E. Aprile *et al.*, "The XENON1T Dark Matter Search Experiment," arXiv:1206.6288.

Acknowledgments

I would like to thank Prof. Dr. Manfred Lindner enabling me not only to write my master thesis in his group but making it possible to attend various conferences, winter and summer schools. Also I would like to thank Prof. Dr. Andre Schöning who agreed to correct my thesis.

Most of all I would like to thank Dr. Teresa Marrodan who supervised me during the last year by answering my endless questions with an incredible patience and arousing my scientific curiosity.

I would like to express my gratitude to Dr. Hardy Simgen, Dr. Marc Weber, Dr. Sebastian Lindemann and all members of the XENON group at the Max-Planck-Institute who kindly supported me whenever possible. Also I would like to thank all people in the XENON100/1T collaboration, especially the analysis team, for all the helpful discussions.

My daily work was accompanied by Meike Danish, Tim Wolf, Dominik Stolzenburg, Juliana Stachurska, Sebastian Ohmer and many others where I could discuss any physical question without hesitation and found encouragement every day. Finally, I can confirm our motto, *all's well that ends well*!

I can not name all my friends who helped me during the last year, but I would like to thank especially Steffen Hagstotz and Jonas Zeuner for their encouraging humor. I appreciated the generosity of my flatmates who saved me from starving at the weekends. Last but not least I thank my family for their endless support no matter what audacious plan I have in mind.

Erklärung:

Ich versichere, dass ich diese Arbeit selbstständig verfasst habe und keine anderen als die angegebenen Quellen und Hilfsmittel benutzt habe.

Heidelberg, den 13.05.2014 .....